Observation manual for stellar occultation by asteroids

Version 1.0
March 2025

Contents

Introduction **1**

1 Recent trends in occultation observation **6**

2 Stellar occultation by asteroids and principles of its measurement **8**

2.1 Overview 8
2.2 Occultation by Asteroids 9
2.3 Observation of Occultation by Asteroids 9
2.3.1 Capturing occultation phenomena with a video camera 11
2.3.2 Determine the most probable time of the phenomenon from the photometric results 11
2.3.3 Estimation of time error 15
2.3.4 Time resolution 15
2.3.5 "Non-instantaneous" increase/decrease light 17
2.4 Video camera for occultation observation 18
2.4.1 Image capturing performance 18
2.4.2 Time stability 20
2.4.3 Global shutter and rolling shutter 21
2.5 Getting Accurate Time — Time and Clocks 23
2.5.1 PC System Clock 23
2.5.2 NTP Server 24
2.5.3 Satellite positioning system 25
2.5.4 GPS receivers 25
2.5.5 GPS receiver and leap seconds 26
2.5.6 Precautions for using "older-generation" GPS receivers 27
2.5.7 Other Clocks 30
2.5.8 Improving reception conditions 30
2.6 Record UTC time values in video images 30
2.7 Record PC time values in the video image 31
2.8 Obtain precise time from LED light imaging synchronized to 1PPS 34
2.8.1 Capture 1 PPS LED light with non-integer frame rate 34
2.8.2 Frame rate and the recording time of the LED light emission 34
2.8.3 Measure "multiple sets" of LED light increase (decrease) 37
2.8.4 Area of LED light emission on the image and temporal stability of LED light 37

2.8.5 If only one LED light brightness increase (or decrease) could be recorded . . . 38
2.8.6 If LED light is not available . . . 39

3 Observation Instruments **40**
3.1 Using a high-sensitivity astronomical CMOS camera for occultation observations . . . 40
3.2 Camera control software "SharpCap" . . . 40
3.2.1 Operating Environment . . . 41
3.2.2 Install . . . 42
3.3 Equipments . . . 43
3.3.1 CMOS Camera . . . 43
3.3.2 Telescope tube . . . 43
3.3.3 Telescope mount . . . 45
3.4 Tools for setting the clock . . . 45
3.5 LED light-emitting device with GPS PPS signal . . . 49

4 Observation Methods **49**
4.1 Preparation for observation . . . 49
4.1.1 Prediction of Occultation Phenomena . . . 52
4.1.2 Selection of observation sites . . . 52
4.1.3 Confirmation of target stars . . . 53
4.1.4 Secure power supply . . . 53
4.2 At the observation site . . . 53
4.3 Setting parameters for SharpCap . . . 55
4.4 Observation . . . 57
4.4.1 Test observation . . . 57
4.4.2 Main observation . . . 58

5 Data Analysis **60**
5.1 Fundamentals of Photometry . . . 60
5.1.1 Measurement region and photometry procedure . . . 60
5.1.2 Tracking of the star images . . . 62
5.1.3 "Anchor mode" and "Drift mode' . . . 62
5.1.4 PSF tracking and Aperture tracking . . . 63
5.2 From the measurement of the time of the event by Limovie to the reporting of the observation . . . 64
5.2.1 Preparation . . . 65
5.2.2 Main flow . . . 65
5.2.3 Detailed Operation Procedures . . . 65

5.2.4 Output Example 86

6 Observation Reports **87**
6.1 Observation site 88
6.1.1 Measure the longitude and latitude of the observation site 88
6.1.2 Observer's elevation 88
6.2 Report 89

7 Appendix a **91**
7.1 Observations of stellar occultation by asteroid (3200) Phaethon; DESTINY$^+$ flyby targets 91
7.1.1 The importance of Phaethon observations 91
7.1.2 Observations of stellar occultation by Phaethon 94

Introduction

The phenomenon of the moon obscuring the sun is called an "solar eclipse". The Sun, which shines brightly during the day, is suddenly obscured and the area around it becomes dark, so it was once a cause of fear for people. Now that we understand how solar eclipses occur, solar eclipses have become a popular form of viewing.

While solar eclipses occur during the day, lunar and stellar eclipses or occultations occur at night. A lunar eclipse occurs when the Earth blocks the moon from the sun's light. Like solar eclipses, lunar eclipses are visible to the naked eye and have been recognized by humans since ancient times. What about stellar eclipses or occultations? Stellar eclipses or occultations are a phenomenon in which a star is eclipsed by another celestial body. There are many celestial bodies in the solar system (planets, satellites, asteroids, comets, outer solar system bodies, etc.), and these celestial bodies are much closer to Earth than fixed stars, and when viewed from Earth, they move at different speeds and in different directions than the diurnal motion of fixed stars. In short, solar system bodies pass in front of fixed stars. When the star and the object passing in front of it are exactly aligned, the star suddenly disappears because the object in front of it blocks the star's light. The term "stellar eclipse" is conventionally used when the moon obscures a star, and the term "stellar occultation or occultation" is conventionally used when an object other than the moon, such as an asteroid, obscures a star. From now on, we will use the term "occultation" to refer to both stellar eclipses and occultations.

Since the fixed stars are far away, they appear only as a point of light. The celestial bodies passing in front of them are closer, so they appear to move much faster than the fixed stars. Therefore, the time that the celestial body obscures the fixed star depends on the size of the obscuring body (see figure 1), but it is usually very short. When a star is obscured by a large celestial body such as a planet or moon, it may be obscured for tens of minutes, but when a small asteroid obscures a star, the time it takes to obscure the star is often less than a second. The phenomenon is very short, and the obscured star is so faint that people probably will not notice when it disappears. Therefore, occultations are almost never noticed in everyday life. But even though it is a phenomenon we don't notice, we should not ignore it, and we should think about the movement of the earth as it rotates and orbits the Sun in space, and the movement of distant stars and celestial bodies in our solar system. When a celestial body in our solar system passes in front of a distant star, the light of the star is blocked by the celestial body

in our solar system, and the shadow of the celestial body falls on the ground. This shadow moves along with the rotation of the Earth and the movement of the celestial body in our solar system. Many small solar system bodies are usually too faint to be seen with the naked eye, but their shadows allow us to notice their existence. Smaller, fainter objects that cannot be seen even with a telescope can be revealed by observing their "**shadows**". That's pretty amazing, isn't it?

Because the stars are far away, the light from the stars reaches the ground as parallel light. The shadows cast by the objects are almost the same size and shape as the objects themselves (*note that if the object to be hidden is small, the effect of light diffraction must be considered [1]). In other words, by measuring the size and shape of the shadow, we can determine the size and shape of the objects that are invisible to the eye. You can see how we can measure the shadow size by looking at Figure2. We say that the object obscuring the star here is an asteroid. You can see how the size of the asteroid's shadow is measured in Figure 2. The brightness of the star that is obscured by the asteroid is measured. As the star is obscured by the asteroid, the brightness of the star suddenly decreases. When the asteroid moves out of the way of the star and the star becomes visible again, the brightness of the star returns to its original brightness. This process is captured in a movie, and the time it takes for the star's brightness to diminish and recover is measured.

Furthermore, as shown in Figure 3, if we observe the star obscured by the asteroid from many observation sites simultaneously, "the shape of the shadow" = "shape of the asteroid" (cross section of the asteroid as seen from Earth when the occultation occurs) can also be determined. Since asteroids are usually irregularly shaped, the more observation points you have, the shape will be determined more accurately.

This manual is intended to be useful to all amateur and professional observers interested in observing occultations. We hope that the methods described in this manual will be useful for your own observations.

In Chapter1, you can read about recent rapid progress in occultation observation. Occultation observation has recently attracted the attention of many amateur and professional observers and plays an important role in supporting planetary exploration missions. If you are new to occultation observation, you can start by reading Chapter3 and Chapter4 to see an occultation event for yourself: how objects obscure stars. If you are interested in how to improve the accuracy of your observations by comparing your results with the analysis of observers at other locations, you may want to read Chapter2 and Chapter5 for a deeper understanding of the occultation events

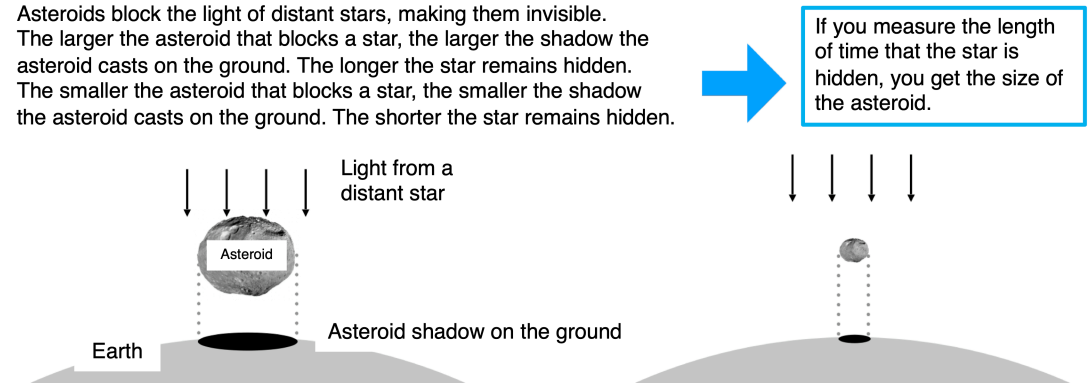

Figure 1: When an asteroid obscures a star, the shadow of the asteroid is cast on the ground. If the asteroid is large, the shadow is also large and the time the star is obscured is long. If the asteroid is small, its shadow is small and so the time the star is obscured is naturally shorter. In other words, by measuring the time duration the star is obscured, the size of the asteroid can be determined.

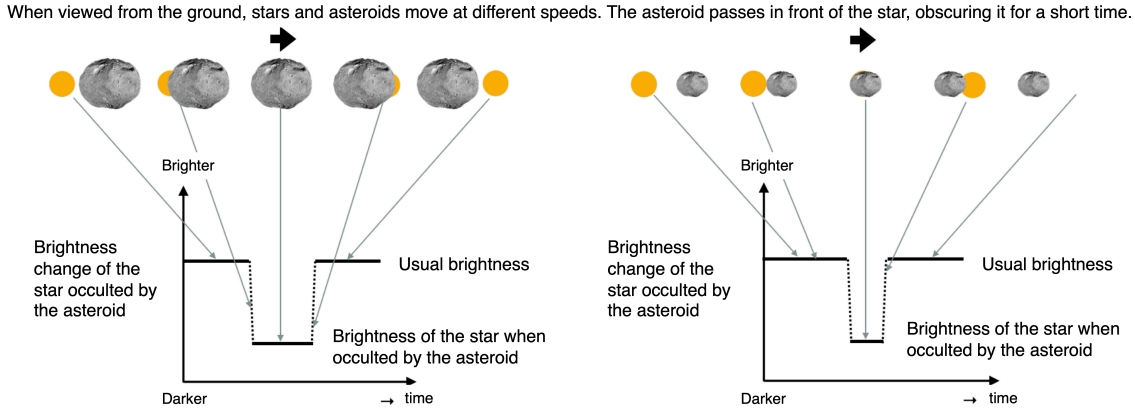

Figure 2: When an asteroid occults a star (= yellow circle), the brightness of the star suddenly changes. As shown on the left, if the occulting object is large, the star is dim for a long time (=the shadow is large). On the other hand, when the occulting object is small, as shown on the right, the star is dimmed only for a moment (=the shadow is small). We take a movie of the occulted star and measure the change in brightness. We measure the timing when the star becomes dim, which is the moment the star is obscured by the asteroid, and the timing when it becomes brighter again, which is the moment the star reappears from the asteroid, and convert the duration time the star is dimmed into the size of the shadow.

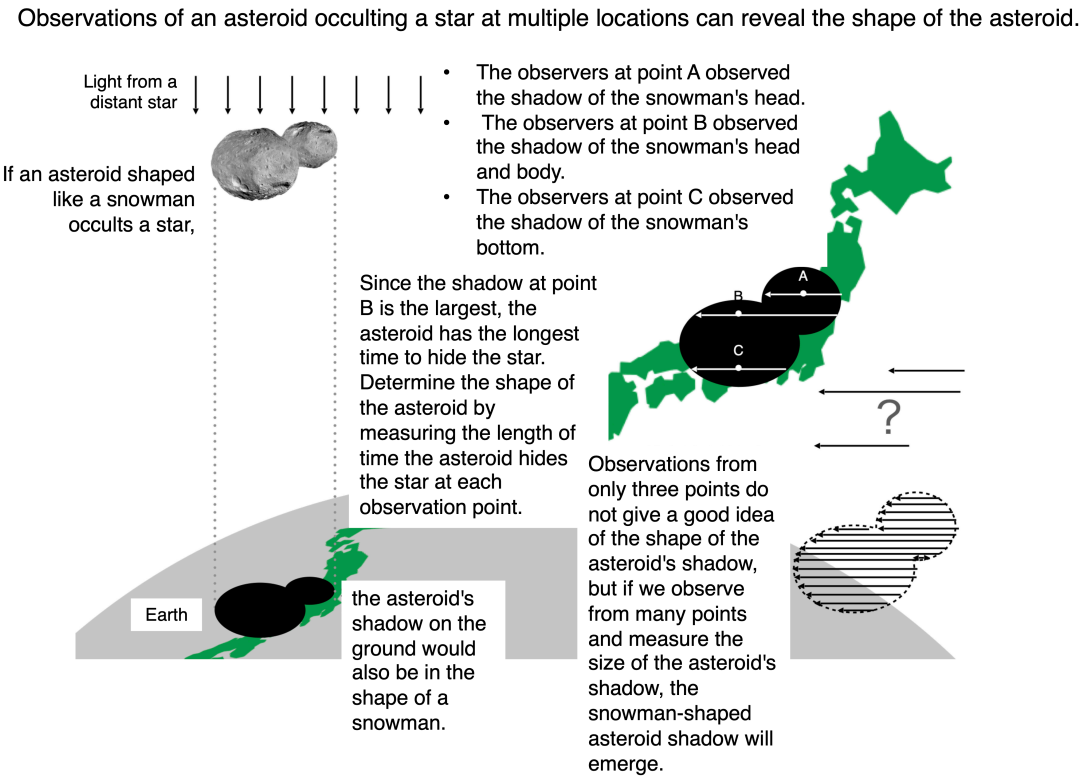

Figure 3: To determine the shape of the shadow that an asteroid casts on the ground when it blocks the light of a star, it is necessary to make multiple chord observations from many different observation sites.

and the data you have taken. The actual results of successful multi-chord observations are given in Appendix7.

Since more observation sites are more advantageous for occultation observations, in order to increase the number of observers, we have prepared Japanese and English versions of this manual. Please make this manual useful for joint observations across country/regional borders. We hope that occultation observations will continue to grow in the future.

2025.03.31

Authors (in alphabetical order)
Tsutomu Hayamizu
Kazuhisa Miyashita
Hiroyuki Watanabe
Hidehito Yamamura
Fumi Yoshida

1 Recent trends in occultation observation

As mentioned in Chapter , the phenomenon of a star being obscured by other celestial body is called "occultation". The phenomenon of an asteroid obscuring a star is a form of occultation, but the observational history of "asteroid occultation" is relatively new and it has become an important field of occultation observation in recent years. The main goal in occultation observation is to obtain the exact time of the moment when the occultation occurs. Therefore, if you have a camera capable of taking movies and a device to record the time on the movies, all of you have a chance to observe the occultation phenomenon. Occultation occurs frequently, but only for a short time in a very limited area, as mentioned in Chapter . The scientific result of a single occultation event is better when a large number of observations are collected together than when a single observation is made. Because of these characteristics, occultation observation has grown as a field of observation mainly for amateur astronomers.

Occultation observations by asteroids have been used as a means of measuring the size of asteroids. However, after the infrared satellite IRAS was launched in 1983 (https://lambda.gsfc.nasa.gov/product/iras/), and the establishment of a method for estimating the diameter of asteroids was established using both visible and infrared observations, occultation observations have almost retreated from being a common method for estimating the size of asteroids. Recently, however, the number of occultation observations has been increasing. According to the statistics on the number of observed occultations by asteroids, which can be found using the function of the occultation prediction software "OCCULT" (http://www.lunar-occultations.com/iota/occult4.htm) (Occult v4.12.x.x) > Asteroid Observations > statistics and find occultations of a star"), we find that a total of 8020 occultation events for 2333 asteroids have been observed in the world, and the total number of positive detections is 26605 by December 6, 2022. As a result of these observations, 115 double stars and 47 satellites of asteroids have been discovered. During the 20th century, the number of observations per year was less than a few dozen in the world, then it began to exceed 500 per year around 2018. In Japan, the number of observations was less than 10 in the 20th century, and now more than 100 since 2021.

This rapid increase is due to

1. amateurs became able to compute occultation predictions with accuracy comparable to that of professionals do, and

2. amateurs got the cameras to take high-sensitivity movies because inex-

pensive and high-sensitivity CMOS cameras are widely spread around the world.

1. is related to the fact that "OCCULT", a software program for generating predictions and analyzing observations for astronomical occultation phenomena provided by Dave Herald (Australia), incorporated the Gaia catalog (accurate positions of stars) and NASA JPL's Horizons system (accurate positions of asteroids), and then the accuracy of the prediction became drastically higher.

2. is related to the observation camera commonly used in Japan. Most of the occultation observers in Japan use QHY174M-GPS (from QHY) or ASI290MM (from ZWO). QHY174M-GPS, which was developed for occultation observations, became popular as a standard camera for occultation observations around 2017 after the observation of stellar occultation by the Kuiper Belt object (486958) Arrokoth, which is the flyby target of NASA's New Horizons spacecraft. On the other hand, since the QHY174M-GPS is quite expensive, it was not widely used by Japanese amateurs. Instead, the ASI290MM, which was developed as a popular planetary imaging camera, became popular among Japanese amateurs. However, the ASI290MM camera does not have a built-in GPS function. This camera does not have a built-in GPS function, so it requires a unique observation method (see Chapter 4).

The aforementioned occultation observations of (486958) Arrokoth were supported by the New Horizons mission and were a great success. The occultation observations predicted that (486958) Arrokoth is a contact binary before the spacecraft flyby. In Japan, occultation observations of the Apollo-type asteroid (3200) Phaethon, the flyby target of the DESTINY$^+$ mission, were systematically performed in 2019, 2021, and 2022. The 2021 observations were performed from 35 different sites, and then the positive detections were reported from 18 sites. These observations helped to determine the exact size and shape of Phaethon. The observation of the occultation by Phaethon was also a great success in 2022 (see chapter 7 for details). The size and shape of asteroids obtained from occultation observations leave little room for error. As these examples show, occultation observations have recently attracted the attention of professional researchers as a tool for solar system exploration missions.

(a) QHY174M-GPS **(b)** ASI290MM

Figure 4: (a) QHY174M-GPS (made by QHY) is a mainstream camera among overseas occultation observers. (b) ASI290MM (made by ZWO) is popular among Japanese occultation observers because of its low price. But this ASI290MM has no GPS function. To compensate for the lack of GPS function, it is necessary to use a GPS module at the same time (see text for details).

2 Stellar occultation by asteroids and principles of its measurement

2.1 Overview

More than a million asteroids have been discovered in the Solar System. Asteroids range in size from several hundred kilometers to several meters in diameter. The large asteroids are nearly spherical, but as their size decreases, they tend to become elongated or irregular. The shape and approximate size of an asteroid is estimated by radar observations, light curve observations, thermal models based on the amount of thermal radiation from the asteroid, and/or a combination of these observations. Occultation observation is a method of measuring the shadow cast by the asteroid on the ground, and since it does not involve an artificially generated model, it can accurately measure the shape and size of a cross-section of the asteroid at a given time when the occultation occurs. The accuracy of the measurement depends on how accurately the time of the occultation is measured. To learn about the various techniques for obtaining accurate time and its measurement, please read the sections 2.3 and 2.5. Occultation observations are made

with several instruments. To obtain accurate observations, it is necessary to understand the following instruments and things.

1. High-sensitivity video camera capable of continuously capturing images at a stable frame rate
2. High-precision clock tied to Universal Time Coordinated (UTC)
3. Method for determining the accurate start/end time of exposure for each frame
4. Setting an appropriate frame exposure time (time resolution), taking into account the duration of the occultation event
5. Method for determining the time of disappearance/reappearance, taking into account the effect of light diffraction.
6. How to know accurate latitude, longitude, and elevation of the observation site.

2.2 Occultation by Asteroids

At night, the surface of the Earth is illuminated by the light of distant stars. Their light is so faint that it is unrecognizable to our eyes. However, if you go outside on a moonless night when there are no city lights, you will see that it is not all black. That is the light of the stars. When a celestial body such as an asteroid passes in front of a star, the light of that star is blocked by the asteroid, creating a shadow of the asteroid on the Earth's surface. As the positions of the celestial body and the Earth change, the shadow moves across the Earth's surface. Observed from our telescopes, the star disappears at the moment it is obscured by the asteroid (this is called "disappearance"). At that moment, observers on the ground are in the shadow of the asteroid, but after a while, when the asteroid passes in front of the star, the stars suddenly appear again (this is called "reappearance"). This phenomenon is called "occultation".

2.3 Observation of Occultation by Asteroids

"Occultations by asteroids" have been observed to reveal the position, shape, size, etc. of the asteroid. Suppose that a certain occultation phenomenon is observed at several points on the ground as shown in Figure 5. Some points pass near the center of the shadow (at point "C" in Figure 5), and some

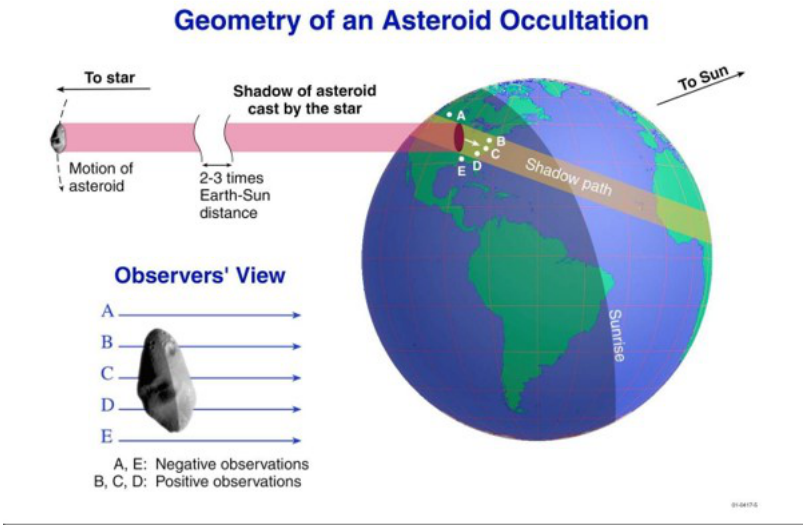

Figure 5: When an asteroid passes in front of a star, the asteroid's shadow is cast on the Earth. Since the star is very far away, the light reaching the Earth from the star is considered to be parallel light. Therefore, the size of the asteroid's shadow is equal to the size of the asteroid (for very small asteroids, the effect of diffracted light must be considered).This figure is cited from https://occultations.org/occultations/what-is-an-occultation/

points pass near the edge of the shadow (points "B" and "G" in Figure 5). There are also points where the star is out of the shadow and not hidden at all (points "A" and "E" in Figure 5).

The time that the star is obscured is longer near the center of the shadow and shorter near the edge of the shadow, reflecting the length of the shadow. The length of the shadow measured at each observation point is represented by a straight line on the observation reduction diagram, and the length of the line is called the "chord length." The exact time at which the occultation occurs at your observation site must be known before the observation because the time of the shadow's passage varies depending on whether the observation site is located forward or backward along the shadow's path. To do this, you need to know the exact longitude and latitude of your observation site (using GPS (see sections 2.5.4, 6.1.1) and the elevation (using published topographic maps (see section 6.1.2). The respective observation data collected at different observation sites with different shadow passage times are

corrected for differences between observation sites using the shadow speed. This is called "observation reduction". By performing "observation reduction", we can obtain the exact shape of the asteroid.

2.3.1 Capturing occultation phenomena with a video camera

Because fainter stars are more numerous throughout the sky, the probability of occultation by asteroids is higher for fainter stars. Recently, most of the reported occultation observations are for stars in the 10th to 12th magnitude range. Observations of such faint stars are made with a telescope equipped with a high-sensitivity detector.

One such detector is a high-sensitivity video camera. A video camera continuously outputs images (frames) that are exposed for short periods of time to create a moving image. Figure 6 shows a series of cropped video frames of the occultation event by asteroid (245) Vera taken with a frame exposure time of 0.202 s. The star looks slightly fainter in the fourth frame from the top and then disappears completely in the fifth frame. The timestamp indicates the time of each frame (corresponding to the end time of the frame exposure), so we can guess that the star disappeared at about 17h43m16.402s. However, we do not know how long before (or after) the timestamp the phenomenon (disappearance) occurred. Therefore, observers usually report the time of disappearance as 17h43m16.402s $\pm$ 0.202s, the error value being equal to the exposure time of the frame. In this case, the time resolution of the observation can be 0.404 s, which is twice of the frame exposure time. For a precise understanding of time resolution, see the section 2.3.4).

Let us look at the reappearance side of the phenomenon. A faint star is seen in the frame time stamped as 17h43m22.866s (the fourth frame from the bottom). This indicates that the star appeared a little before the time stamped. How long ago did the star appear? We will discuss how to determine the exact time of the disappearance/reappearance from the photometric results in the next section 2.3.2.

2.3.2 Determine the most probable time of the phenomenon from the photometric results

In frame-by-frame video (visual inspection of frame images), the time resolution is the interval between frame outputs. If we can measure the star's brightness on the video in the same way that we measure the star's brightness on a still camera image, we can get a light curve of the star on the video

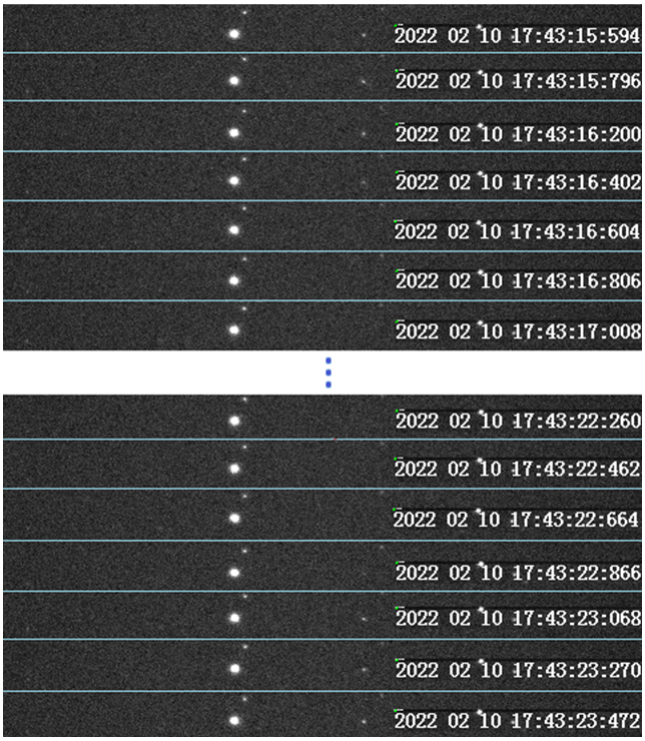

Figure 6: The asteroid (245) Vera (13.4 mag) occulted the star TYC 285-00908-1 (10.9 mag). The image was captured with a video camera (observed by Akira Asai on February 10, 2022). The top seven frames show the disappearance of the star. The lower seven frames show the reappearance of the star.

and improve the time accuracy. This can be done using video light-curve measurement software such as Limovie or PyMovie.

Figure 7 shows the case where the disappearance occurs at the time of one-third during the exposure of the nth frame. Assuming that the image of the star disappeared immediately due to the occultation, the brightness of the star in the nth frame can be one-third of the brightness before the occultation. Conversely, if the star's brightness is one-third of what it was before the occultation, the phenomenon could occur one-third of the time between the start of exposure of the nth frame and the frame output. Based on this principle, Limovie creates a model of the phenomenon, including light diffraction, and compares it with the photometric results of the observation, then obtains the most accurate time of the phenomenon. The light curves obtained from the observation and the time of the phenomenon calculated from the model fit are shown in Figure 8.

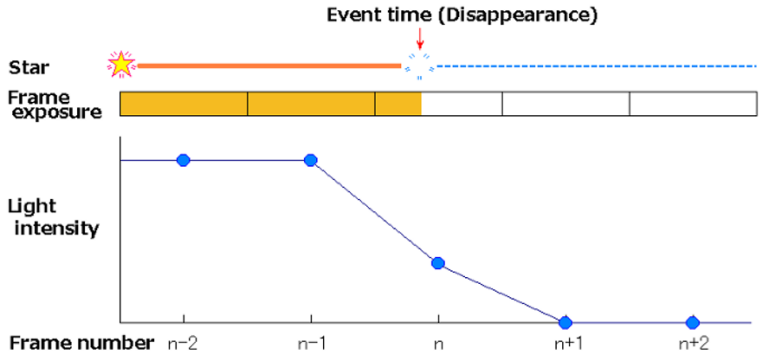

Figure 7: When occultation (dimming) occurs in the middle of the exposure of the frame.

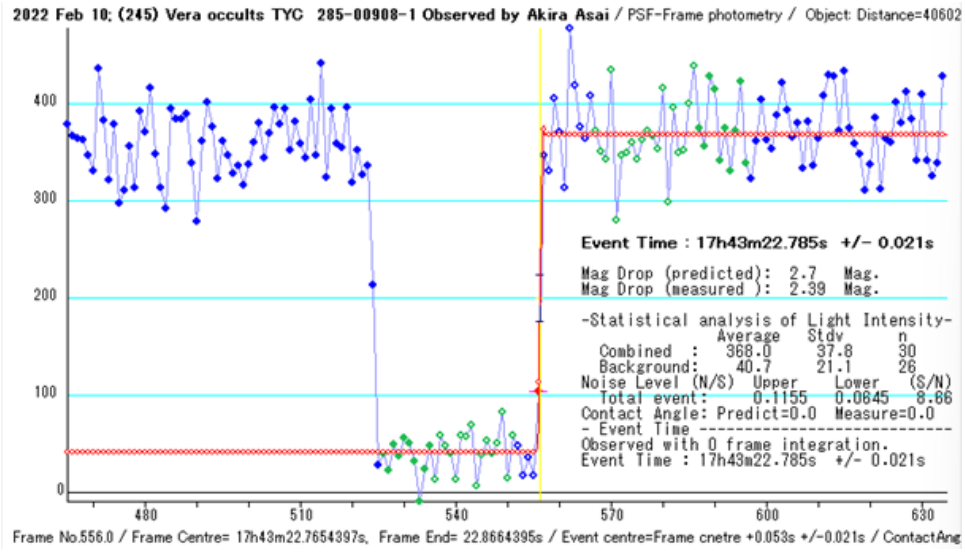

Figure 8: We analyzed the video shown in Figure 6, and then fit the diffraction simulation model to the light curve of the star occulted by the asteroid to obtain the most likely value of the event time. As a result, we found that 17h43m 22.785 $\pm$ 0.021s was the most likely value of the event time. This means that the event occurred 0.081s before the timestamp of 17h43m 22.866s, which is the timestamp of the frame in which the faint star image was seen.

2.3.3 Estimation of time error

First, the error factor in determining the time as described in the previous section is the noise on the light curve. This noise is caused by the readout noise on the image sensor and the blinking of the star due to atmospheric turbulence. How can we estimate the time error in such cases? Although it is possible to obtain the amount of error by statistically processing the results of observations of a single phenomenon with a large number of telescopes at a single observing site, this is not realistic. Therefore, we estimate the time error based on the following idea.

We have created software with the ability to create noisy phenomena and find the most likely values from them. The phenomenon generation function generates random noise, such as that seen in light curves, and adds it to the appearance or attenuation model. It also allows the creation of different types of noise. The light curves created in this way are analyzed by the function that finds the most accurate values. There will be an error between the moment of the phenomenon before the noise is added and the most accurate value obtained by the analysis. The above procedure is repeated many times (more than 1000 times) and the degree of variation (in frames) is calculated as the standard deviation (1σ), which is treated as an estimation error.

The time error ER ($1\ \sigma$) (seconds) can be expressed as follows, where LD: light intensity change due to occultation, SD: standard deviation of the light intensity value before the light intensity decreased, and FT: frame output interval (seconds).

$$ER = FT \times \frac{SD}{LD} \tag{1}$$

When SD/LD reaches 0.4, the error reaches one frame, so the time resolution is equal to the frame output interval. This can happen if a star is too faint to be captured, or if the asteroid is too bright relative to the star, or if the attenuation is too small.

2.3.4 Time resolution

In the case of occultation observations to study the shape of small asteroids, how accurately the topography on the asteroid can be determined (length resolution) depends on the "time resolution" of the observation. Time resolution is a concept that is needed when planning an occultation observation and is replaced after the observation by the resulting estimated time error. Therefore, the "time resolution" that should be considered at the time of

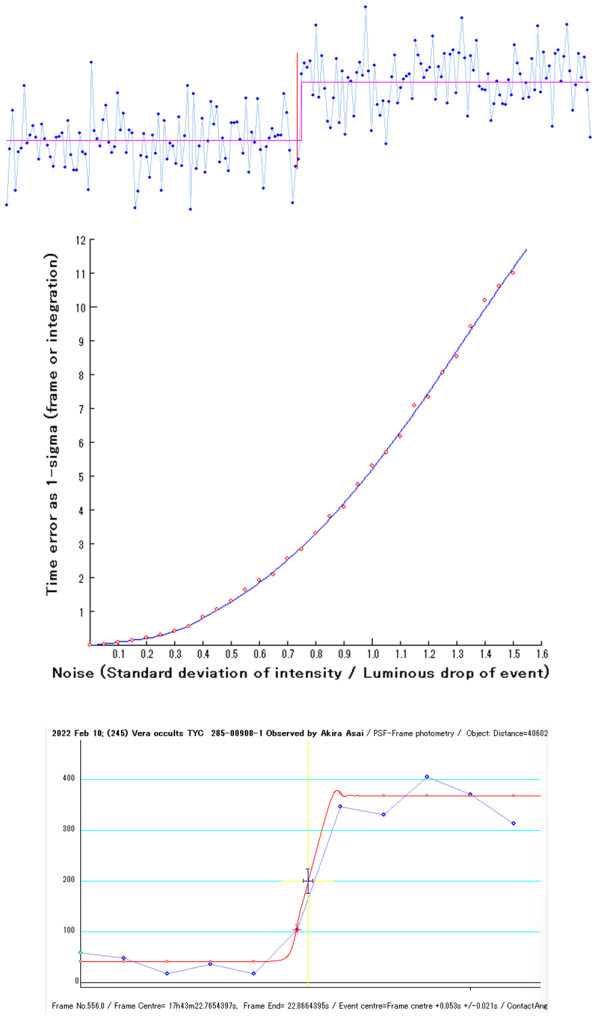

Figure 9: Effect of Lightcurves noise on Time Errors (Top) Correct time of appearance (vertical red line) and the most accurate value obtained from the light curve with noise (magenta). Here is an example of noise with S/N=2.0. In this case, the time error is nearly one frame between the correct appearance time (vertical red line) and the most accurate value obtained from the noise light curve (magenta). (M) Relationship between the noise (inverse of S/N) and the estimated time error (1 σ expressed in frame exposure time). The standard deviation was obtained by repeating the process shown in the upper panel many times with different values of S/N. (Bottom) Phenomenon time and estimated time error obtained. Vertical error bar of blue cross indicates the variation of light intensity, and horizontal error bars indicates the estimated time error.

planning is expressed by equation (1), which requires the value of the signal-to-noise ratio on the assumed light curve in addition to the frame exposure time. The middle panel in Figure 9 shows that 1 σ is approximately 1.0 when S/N is 2.5 (N/S=0.4), which can be used as a guide. However, even if the S/N of the light curve is measured by preliminary observation the day before, if the attenuation during the occultation is close to zero, the S/N as it is can be used, but it should be noted that the S/N will be reduced to half the value when the attenuation is 50%.

The time resolution should be determined by considering not only the frame exposure time but also the amount of attenuation and the atmospheric conditions of the day (which depend on the altitude of the target star, monsoon conditions, etc.) when planning the observation.

2.3.5 "Non-instantaneous" increase/decrease light

Since a star is a point light source, the shadow of an asteroid on the ground is often thought to have a sharp edge, but in reality, the light diffraction at the edge of the asteroid causes a gradual change in brightness. Therefore, when an asteroid passes in front of a star, the increase or decrease of light is not instantaneous, but the light intensity changes with a curve like the one shown in Figure 11.

If the size of the object occulting the star is sufficiently large and the edge can be regarded as a straight line, the change in brightness near the shadow edge can be expressed by the following equation.

$$I(t) = 0.5I_0[(0.5 + C(\omega))^2 + (0.5 + S(\omega)^2], \tag{2}$$

where $C(\omega)$ and $S(\omega)$ are Fresnel integrals and are expressed by the following equations.

$$C(\omega) = \int_0^x \cos\left(\frac{\pi t^2}{2}\right), S(\omega) = \int_0^x \sin\left(\frac{\pi t^2}{2}\right) \tag{3}$$

Also, ω is the Fresnel number and is expressed as follows.

$$\omega = \left(\frac{2}{\lambda D}\right)^{\frac{1}{2}} \nu(t - t_0), \tag{4}$$

where λ is the wavelength of light, D is the distance to the asteroid, and ν is the speed at which the moon's shadow moves in the plane perpendicular to the line of sight. If the limb of the asteroid is tilted from perpendicular

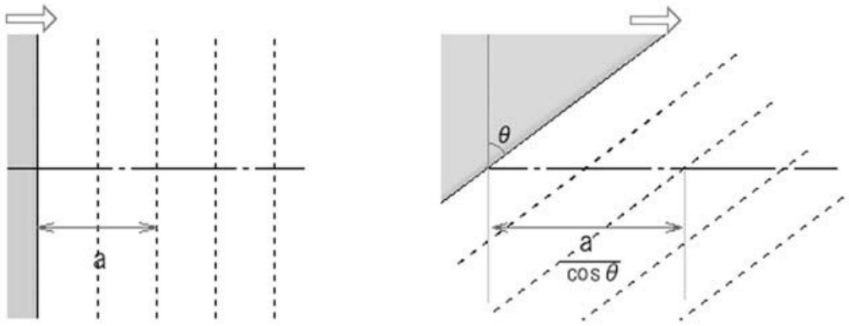

Figure 10: Angle of the edge of the celestial body to the direction of motion and diffraction pattern change.

to the direction of the moon's motion, the brightness changes slowly due to the movement of the shadow on the ground (Figure. 10).

Figure 11 shows the case where the moon obscures the star, and a similar curve is observed for asteroids. This gradual change in light intensity is more pronounced when a celestial body grazes a star. In such a case, the gradual change in intensity produced by the simulation is fitted to the observed light curve to obtain an accurate time.

In addition, if the star has an apparent diameter, it will cause a slow increase or decrease in light, similar to the way the sun gradually emerges from the ground at sunrise. Combined with the aforementioned diffraction effects, the larger the apparent diameter, the slower change happens, as seen in Figure12.

2.4 Video camera for occultation observation

A video camera is "a device that continuously outputs still images taken at a fixed exposure time". Video cameras used for occultation observations must be highly sensitive to capture faint stellar phenomena, produce images that accurately record the brightness of stars, and also function as an accurate clock.

2.4.1 Image capturing performance

To accurately record the brightness of the star, it is important that image processing such as gamma correction, for example, is not applied. Video frames taken with conventional SLR cameras and Handycams are strongly

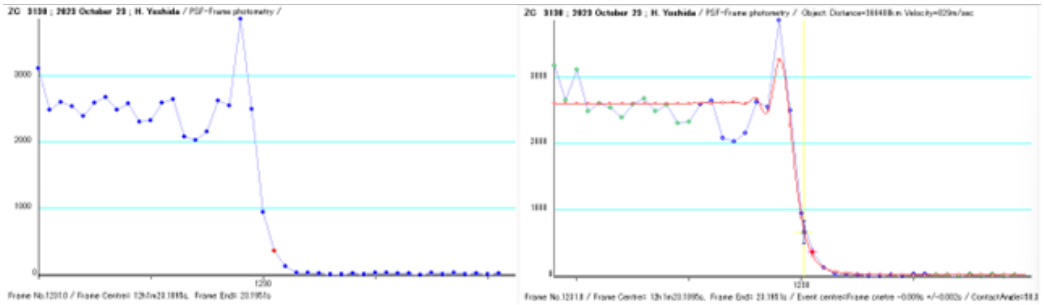

Figure 11: Light intensity changes when the moon occults a star (which has no visual diameter and can be treated as a point source). The time required for the change depends on the distance to the "hidden" object, the contact angle, and the speed at which the object's shadow moves. If the star can be treated as a point source, the light intensity during the event (when the center of the star, the edge of the object (in this case the moon), and the observation point are aligned) is 25% of the intensity before the occultation, as shown with the red dot in the left panel. The right panel shows a comparison with a diffraction simulation (red curve). In the case where the contact angle is set to 50.8 degrees, the simulation and the observed light curve are in good agreement.

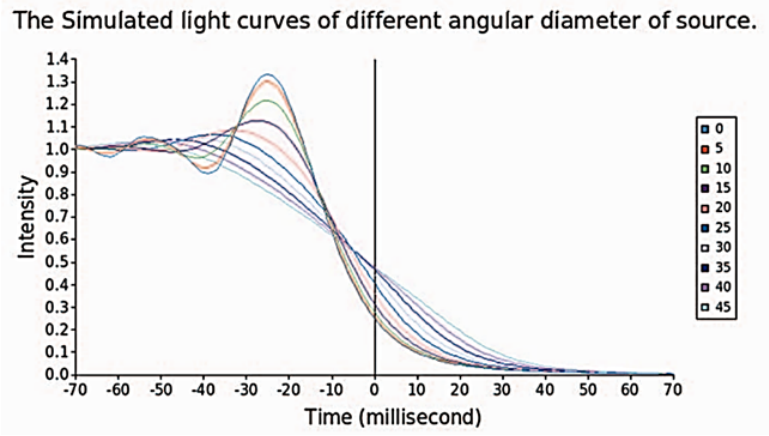

Figure 12: Light intensity variation during occultation when the visual diameter of the star must be taken into account. The light intensity during the event varies from 25% to 50% depending on the visual diameter of the star. This curve is valid when the object is sufficiently large and its edge can be treated as a straight line. The curve is different when the object is far from the Earth and has a small diameter, so it is necessary to specify the shape of the object and the location of the edge that hides the star in the simulation.

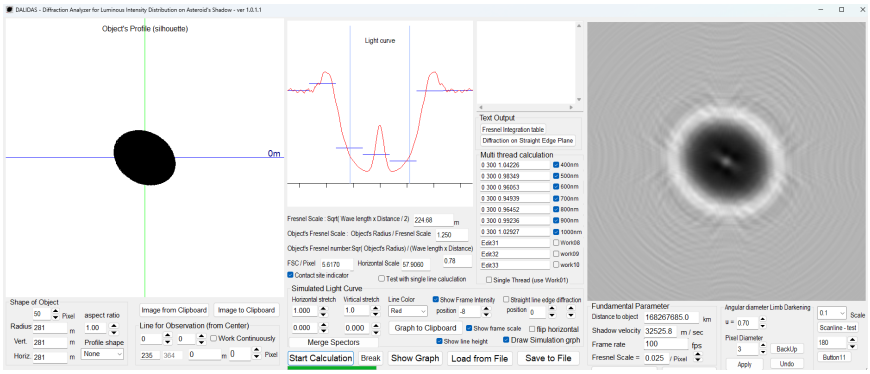

Figure 13: Shadow cast on the Earth's surface by a distant small diameter asteroid. When the Fresnel number is less than 1.0, it is impossible to determine the shape of the asteroid from occultation observations. The figure shows a simulation for a Fresnel number of 1.5. Even in this case, the edges of the shadow are not clear.

image-processed, and the output image does not reflect the amount of light incident on the image sensor in a linear fashion. Therefore, when stars are supernovae, the brightness of each star cannot be measured correctly when captured with such cameras. On the other hand, a high-sensitivity analog video camera (CCD) has a characteristic of linearity of output value with respect to the amount of light received and has been used for occultation observations. CMOS video cameras, which are currently the main type of video camera, are not converted to an analog video signal during the process, so the output value is not affected by the distortion of the amplifier that produces the analog signal and more reliably reflects the amount of light received by the device. Furthermore, CMOS video cameras are 10 times more sensitive and have lower noise than analog video cameras.

2.4.2 Time stability

If the frame output interval is constant, counting the number of frames from "infiltration" to "appearance" and multiplying by the frame output interval (the inverse of the frame rate) gives the duration of the phenomenon, and from this duration, the chord length can be obtained. The time stability during video recording with a CMOS video camera was investigated using a high-performance stroboscope. The results showed that the frame output timing was stable with an error of one order of magnitude less than one

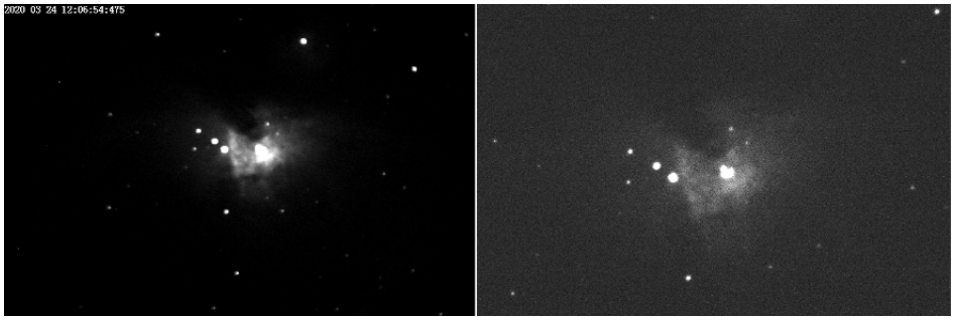

Figure 14: Comparison of sensitivity between analog CCD camera (left) and CMOS camera (right). M42 images were taken with an analog CCD camera (left: WAT120N exp=0.0334 × 16-frame stack) and a CMOS camera (right: ASI290MM exp=0.0333sec (2× binning)) mounted on the same optical system. Comparing the two images, the CMOS camera produces an image that is almost equivalent to the 16-frame accumulation of the CCD camera. Therefore, the CMOS camera is considered to be about 10 times more sensitive than a conventional CCD camera.

millisecond. This confirms that the CMOS video camera functions as a high-precision ticking device (clock).

2.4.3 Global shutter and rolling shutter

The major difference between CCD and CMOS is the way the data is read out. To read out the data of the entire sensor element, it was necessary to stop the exposure of all pixels and complete the "bucket relay – Transfer of charge" (the time required for this bucket relay is called the readout time). This procedure allows the exposure start and end times to be the same for all pixels. This type of exposure is called a global shutter, and in occultation observations, if a precise time is projected somewhere on the image (or recorded as the file name), that time can be used as the time of the event. However, since this way requires a certain readout time, it is not suitable for use in shortening the frame output interval and releasing the shutter at high speed. In a CMOS camera, on the other hand, each pixel has an amplifier that converts the stored electrons after exposure into a voltage signal that is output by a dedicated circuit in the order in which the pixels are arranged. This means that the data transfer time within the device is short. In addition, when data is read out line-by-line instead of for the entire image, the amount of data is much smaller, resulting in a

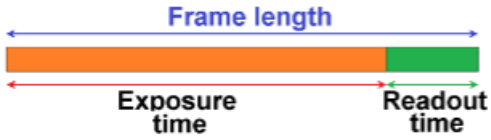

Figure 15: Relationship between exposure time and readout time in one frame of CCD

much shorter readout time. As a result, the ratio of exposure time to frame length can be increased, allowing image capture at a higher frame rate. This is called a rolling shutter.

Figure 16 shows the sequence of rolling shutter operation based on the published data sheet of the SONY IMX290 device and the results obtained from 1PPS (pulses/second) LED light imaging. You can see the datasheet from here http://static6.arrow.com/aropdfconversion/c0c7efde6571c768020a72f59b226308b9669e45/sony_imx290lqr-c_datasheet.pdf. The time required to read one line of data (readout time) is 0.0077 ms, and the remaining time is used for exposure. For example, for a video with a frame length of 20 ms, the exposure time is 19.9923 ms, which means that 99.96% of the frame length can be used for exposure. Thus, video with a recordable frame rate can be treated as "frame length = exposure time".

However, the rolling shutter has the characteristic that the exposure start and end times are different at the top and bottom of the image. The time at the bottom of the image is slightly earlier than the time at the top of the image (for example, a difference of 540 lines results in a time difference of 4.16 ms). Therefore, to get the correct time for occultation observations, the time signal on the image must be on the same line as the star of interest. For example, the LED emitting signal should not illuminate a single point on the image but should illuminate the image vertically in a long and narrow direction or the entire image. This also means that a rolling shutter camera cannot use a method such as a video time inserter, which is often used in analog video cameras with a global shutter system, to display the time value on the image.

Each of the above two shutter methods has its advantages and disadvantages, and the choice is made according to which is more important for the application. However, for a relatively small aperture telescope used by amateurs, a rolling shutter camera is more useful because the first priority is "high sensitivity and the ability to see the object being observed". Therefore, some efforts have been made to compensate for the disadvantages of

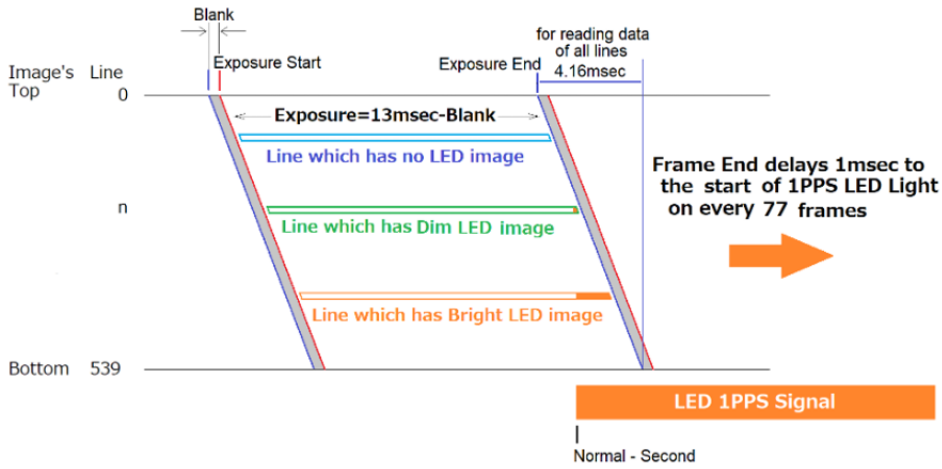

Figure 16: Operation sequence of rolling shutter type image sensor (SONY IMX290).

rolling shutter cameras by developing methods to improve the time accuracy. A large part of this manual is devoted to describing these innovations. Some CMOS image sensors also use a global shutter (e.g. QHY174). The sensitivity is inferior because the ratio of exposure time to frame output interval is not large, but there is no time difference in the image.

2.5 Getting Accurate Time — Time and Clocks

Here we present several clocks used for occultation observation.

2.5.1 PC System Clock

When observing with a CMOS camera, the captured images are saved as a movie file on the PC's hard disk drive. The PC system clock is one of the clocks that play an important role in the observation, because the time of the PC system clock is recorded in the movie. The PC has a crystal oscillator to drive the CPU, and the operating system works as a clock by counting the signals from the oscillator. The time displayed in the Windows system tray is the time value of the system clock, which stops working when the PC is turned off, but a separate crystal clock is built into the PC, and when the PC starts up, it reads the time from this crystal clock, and then the system clock is driven by the CPU's crystal oscillator.

As mentioned above, PC clocks work in the same way as electronic clocks

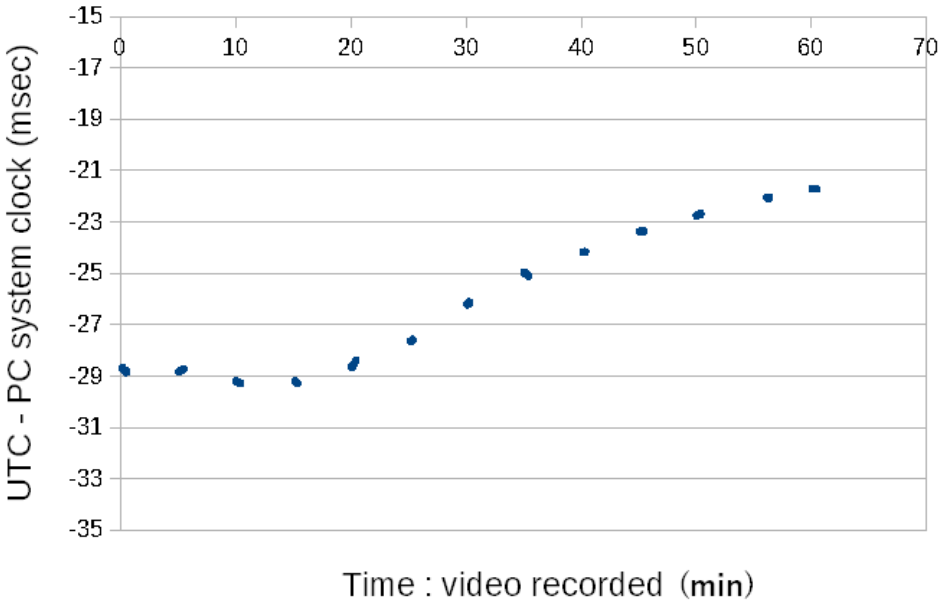

Figure 17: PC System clock indicates time change over time.

(quartz clocks) that we use in our daily lives. They have an advance and a delay. If the PC clock has a large error (advance/delay), it cannot be used for occultation observations. It must to be precisely adjusted (Figure 17). The simplest way to adjust the clock is to synchronize it with an NTP server if connected to the Internet (see 2.5.2. For more accurate time synchronization, it is necessary to synchronize with a GPS receiver (see 2.5.3). In addition, occultation observation requires "correction by 1PPS LED light output from the GPS receiver".

2.5.2 NTP Server

NTP is a protocol used to synchronize the time of computers connected to a network. The data transmitted includes the time information received by the server and the client, and compensates for delays in data transmission over the network and processing on the PC. According to the NICT: Japan Standard Time Group, the synchronization accuracy "may vary widely from a few milliseconds to several hundred milliseconds, depending on the Internet environment". This is not accurate enough for occultation observation, but it is suitable for the purpose of roughly adjusting the time on a PC. Our

recommendation is to synchronize the PC time with the NTP server before applying the method to get the exact time with the 1PPS LED light, which is described below.

For Windows 10 and Windows 11, synchronization is completed by simply clicking the "Synchronize Now" button under "Settings" – "Language and Time" – "Date and Time" in the "Synchronize Time" section while connected to the Internet. However, if the PC time has a delay of 1 second or less relative to UTC at the time of the operation, synchronization will not be performed. If the delay is more than 0.5 seconds, Limovie's time correction function will calculate a value that is 1.0 second different. Therefore, if time synchronization is to be performed using this method, it is necessary to manually set a value that differs from the PC time by several seconds to several minutes in advance, and then perform the synchronization. If the PC is not directly connected to the Internet, such as during an observation expedition, it is possible to use the tethering function of a cell phone or pocket WiFi to connect to the Internet and synchronize as described above. Note that even after synchronization, the PC clock value may change if automatic synchronization is performed during observation recording. For a detailed explanation of NTP, please refer to the URL of the Japan Network Information Center (https://www.nic.ad.jp/ja/basics/terms/ntp.html for a detailed explanation of NTP.

2.5.3 Satellite positioning system

First, the following terminology is used here. The term "GPS", first developed and operated by the United States, has been widely used to describe satellite-based positioning systems. However, since Russia's GLONASS and Europe's GALILEO are now in operation, they are collectively referred to as GNSS. However, since we often use the term "GPS" in our daily lives, we will describe them in the following unified manner.

1. Receivers are referred to as GPS receivers.
2. GNSS is used as a generic term for satellite positioning systems.
3. Except in the case of 1., GPS is used only for systems operated by the United States.

2.5.4 GPS receivers

GPS receivers can be divided into two groups, one according to the development period and the connection method with PCs (Figure 18).

The development period is divided as follows.

- Old generation models: Receivers that use only GPS (USA) and its MICHIBIKI auxiliary satellites for positioning at the start of reception after power-on in the initial configuration (a configuration that the manufacturer expects to be used as a standard).

- New generation models: Receivers that use GLONASS (Russia) satellites in addition to GPS (USA) for positioning at the time of power-on with the initial settings.

The old-generation receivers are less expensive than the new-generation receivers, but the new-generation receivers are more convenient for occultation observations, as described below.

Next, there are two types of connection methods to PCs.

- USB connection: The time is transmitted from TXD (receiver side) to RXD (PC side), and the NMEA sentences are received by RXD (PC side) for PC time correction. The NMEA sentences are transmitted with a delay of 50 to 100 msec relative to the positive second of UTC, and the output time can vary up to 10 msec, so the PC system time can only be corrected to that accuracy. Even with this model, the time can be accurately corrected by Limovie by recording the light from a 1PPS LED. However, a separate 1PPS receiver is required for models that do not have a 1PPS LED.

- RS232C cable or terminal connection: In many cases, it is necessary to make it work by yourself. In such cases, wiring to transmit 1PPS to the PC via the RS232C DSR communication line allows precise PC time correction (+/-0.2msec) using HACSTIP-GPS. However, even if the PC time is accurate, the time stamp will be delayed by the image processing time of capture software such as SharpCap, so time correction by 1PPS LED is necessary as with the USB type. In this method, the amount of light emitted by the LEDs can be adjusted by a variable resistor, making it possible to use a single unit for time-related purposes, which is very convenient for observation.

2.5.5 GPS receiver and leap seconds

The new-generation GPS receivers described in the previous section will output the correct UTC time when the LED starts flashing after power-on because the GLONASS satellites are acquired at the start of reception

	Vendor	Engine	Satellites	RS232C type	USB type
Old generation	ublox	NEO-6M NEO-7M	GPS(USA) etc.	Ren He GY-NEO-6MV2	VK172 DOCTORADIO GR7
	Garmin			15XL/H(GHS-OSD) 18xLVC	
New generation	ublox	NEO-M8M NEO-M9N	GPS(USA) GLONASS(Russia) etc.	GT902PMGG	
	MediaTek	MT3333 MT3337 MT3339		GT502MGG-N AE-GNSS- EXTANT+ANT_SET	GT502MGG-USB GlobalSat BU-353N5 USB

Figure 18: Types of GPS Receivers.

and leap-second information is obtained from them. Therefore, there is no need to wait for the leap-second information, which is necessary for the old-generation receiver as described in the next section. Therefore, if you are using a new-generation model, you can skip the next section.

2.5.6 Precautions for using "older-generation" GPS receivers

It is important to note that with old-generation GPS receivers that only use GPS(USA), the time values that are output immediately after power-up are "wrong". Immediately after power-up, the GPS receiver begins to receive data such as satellite orbits and leap seconds sent by the GPS (USA) satellites. Until all of the data (see Figure 19) is acquired, the correct time value cannot be obtained. Empirically, it is recommended to use the receiver for occultation observations about 20 minutes after the receiver is activated. However, in order to know when a stable time can be obtained, it is necessary to know how the receiver works when using the GPS (USA) satellites. The basic data used by the receiver to calculate position and time is called the "navigation message" and is transmitted in frames such as the one shown in Figure. 19, which consists of five subframes of 300 bits each, with each frame having a size of 1500 bits. The navigation message is transmitted at 50 BPS and a frame is transmitted in 30 seconds. Subframes 1—3 contain information about the transmitting satellite itself and its precise orbit, called the ephemeris. Subframes 4—5 contain information about the orbits (almanac), ionosphere and UTC of all satellites.

For subframes 1—3, the data of the transmitting satellite is sent each time, so the receiver can receive information from four or more satellites simultaneously because the GPS receiver has multiple receiving channels. However, it takes more than 30 seconds ($\sim$ several minutes) to receive the

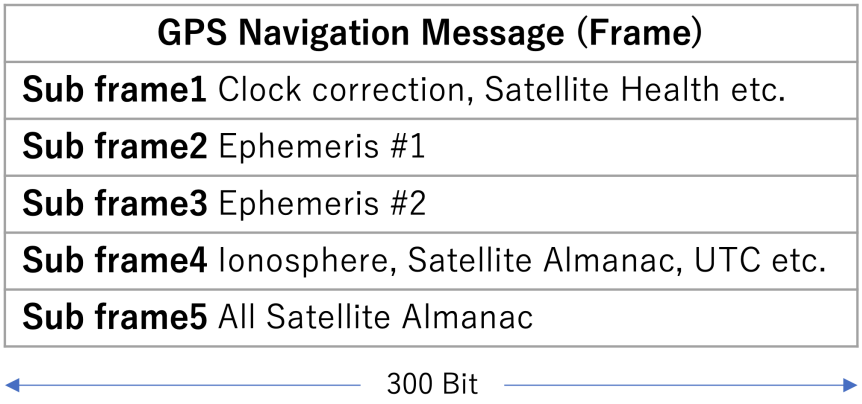

Figure 19: Data structure of navigation messages sent by GPS satellites

data because of the time difference in the start of reception depending on the channel (satellite). In most cases, the receiver calculates and outputs the position (latitude/longitude) and the exact time based on the data received from the satellite after a few minutes. When the receiver is ready to calculate the position and time, the 1PPS LED will blink. The precise time (called GPS time) handled inside the GPS receiver at this time is synchronized to UTC at the timing of 1 PPS, but the time value is different from UTC. As of January 6, 1980, GPS time has been equal to UTC, but since then, "leap seconds" have been inserted into UTC as needed to adjust for changes in the Earth's rotation speed, so that currently (January 2022) GPS time is 19 seconds ahead of UTC. The internal program of the GPS receiver has data on the number of leap seconds inserted up to the time the program was written, so a program written on July 1, 2012, for example, will have the GPS time corrected (subtracted) by 17 seconds from the GPS time For example, a program written on July 1, 2012 would display the current time as the value corrected (subtracted) by 17 seconds from the GPS time. However, this is a time value that is 2 seconds ahead of UTC. In some cases, another "leap second correction" is made later and the correct time is displayed. Therefore, the user must be aware of the discrepancy between the GPS time and UTC and the correction mechanism to compensate for this discrepancy.

When the above "further leap second correction" is made depends on the type of receiver, its history, and the situation. This is one of the major sources of confusion and embarrassment for occultation observers.

If the GPS receiver has a history of operating in synchronization with GPS satellites in its internal memory, it will retain the leap seconds and

other data read at the time of the last reception. Therefore, almost as soon as the receiver is turned on, the 1PPS LED will start flashing to indicate that the receiver is synchronized, and the output (displayed) time value will be fully corrected for leap seconds, indicating the correct UTC time. However, the battery capacity differs depending on the receiver model; a receiver with a large capacity such as a CR2032 battery will hold the time for a year, while the GT502MGG-N will hold the time for a few hours and the VK172 will hold the time for a few minutes. In any case, to verify that leap second data is being received, check the time on the GPS receiver using a telephone time signal or Timeis if tethering is available. If the two match, leap second correction is complete. After that, the GPS receiver can be treated as a UTC clock unless the GPS receiver is turned off. It is important to make this an observation routine to check if the time is correct or not.

What should we do if the leap second has not been corrected and the time difference from UTC has occurred? The answer is "wait 12.5 minutes". To explain this, let us return to the frame data of the navigation message.

While subframes 1—3 repeatedly send the same data for each transmission, the contents of subframes 4—5 are different for each transmission. This is because the amount of data stored in subframes 4—5 is so large that it cannot be sent in a single frame transmission. Therefore, the data is divided into 25 pages, with the first page sent in the first frame, the second page in the second frame, and so on. The leap second data mentioned above is on page 18 of subframe 4. If this page is missed, the next time the same data is read it will be 25 frames later, or 12.5 minutes, since each frame takes 30 seconds to transmit. In other words, if you wait 12.5 minutes, you will get the correct UTC time value. Once the leap second correction is done correctly, the UTC time value is stable as long as the receiver is not turned off.

In the case of the author (KM), the following procedure is used for observing. First, turn on the GPS receiver, and wait the flashing LED indicates that a signal has been received, then set up the telescope and other equipment. The setup process takes at least 15 minutes, by which time the receiver should have received the leap second data and output the correct UTC time value. Once the GPS receiver and GPS satellites are synchronized, the PC's system clock must be synchronized to the GPS clock. See "GPS Caddie Course–6. GPS Satellite System (2) Navigation Messages", https://greenon.jp/gpslecture/2011/01/26/2849/ for an explanation of GPS satellite communication and navigation messages.

2.5.7 Other Clocks

Radio clocks (clocks that are automatically set to the correct time using standard time radio signals) are a convenient way to verify that the time displayed by a PC clock is correct. Although the accuracy of the synchronization is not as high as that of NTP, it is an easy way to verify that the time on a PC clock is correct. Shortwave standard time broadcasts and telephone time signals (so-called "time signals") have long been used for occultation observations. Both can be used to check the accuracy of a PC clock.

2.5.8 Improving reception conditions

Since CMOS cameras have been used for observation, there have been many reports of GPS receivers stopping operation during observation. This is because the signals flowing in the circuit, including the USB3.0 cable used to connect the CMOS camera to the PC, overlap with the GNSS radio band and are a strong source of interference. The GPS receiver needs to acquire signals from at least four satellites, and if the number of satellites is not met, the receiver will stop working.

To prevent this, it is very effective to use a shielded USB 3.0 cable instead of the USB cable supplied with the camera. Although some methods have been tried, such as wrapping the USB 3.0 cable with aluminum foil or adding a ferrite core, these methods are not very effective. Therefore, it is better to use a shielded USB 3.0 cable. Otherwise, it is recommended that the camera cable and the GPS receiver cable be installed at least 60 cm apart. Even if it is difficult, it is better to install them as far apart as possible.

The new generation of GPS receivers can significantly improve poor reception. In addition to GPS (USA), the new generation of GPS receivers can receive signals from GLONASS (Russia) and GALILEO (Europe) satellites, almost doubling the number of satellites that the previous generation could receive. As a result, it can easily meet the requirement of receiving from four satellites.

2.6 Record UTC time values in video images

When using the QHY174-GPS, a video camera with a built-in GPS receiver, the camera can directly receive the GPS signal and output the correct time in the captured image. (Note: For QHY174GPS, when GPS is on, it is the time (UTC) when the exposure started; when GPS is off, it is the time when the exposure ended) (see Figure 20 for the recording format). Since

Figure 20: Time values that SharpCap records in the frame image. The values are superimposed on the image. The seven pixels at the top left corner contain the time since 0:00:00 A.D. in units of 10^{-7} as pixel data.

this camera has a global shutter, this time value can be used to determine the time of disappearance/appearance no matter where the target star appears on the image. However, the sensitivity of this camera is lower than a rolling shutter camera, so it is a good choice when the occultation target star is bright or when observing with a large aperture telescope that can collect enough light. Since the target stars of many occultation events are faint and there are few opportunities to observe the target occultation with a large telescope that cannot move, most amateur observers in Japan use the method described in the next section.

2.7 Record PC time values in the video image

Video cameras other than the QHY174-GPS do not have a built-in GPS receiver. In the case of such cameras, various methods must be taken to correlate the GPS time with the time of the captured image. Unless otherwise noted, the descriptions in this manual refer to occultation observations using a camera without a GPS receiver. For cameras without a GPS receiver, SharpCap records the time of the PC system clock at the top of the image when the image data is read.

First, it is important to note that "this time value cannot be used as a time reference to accurately determine the time of occultation". As mentioned earlier, in rolling shutter mode, the start and end times of the exposure are different in the vertical direction of the image. In addition, there are several other errors. Since the recorded time values are derived from the system clock of the PC, there can be a synchronization error of several milliseconds in the case of a GPS receiver, and up to one hundred milliseconds when using an NTP server, if the system clock is synchronized to UTC. In other words, this degree of delay occurs at the time of synchronization.

In addition, the PC's system clock is driven by a crystal oscillator, which introduces a delay due to its error. The accuracy of the crystal oscillator varies depending on the PC model, but the delay can be more than tens

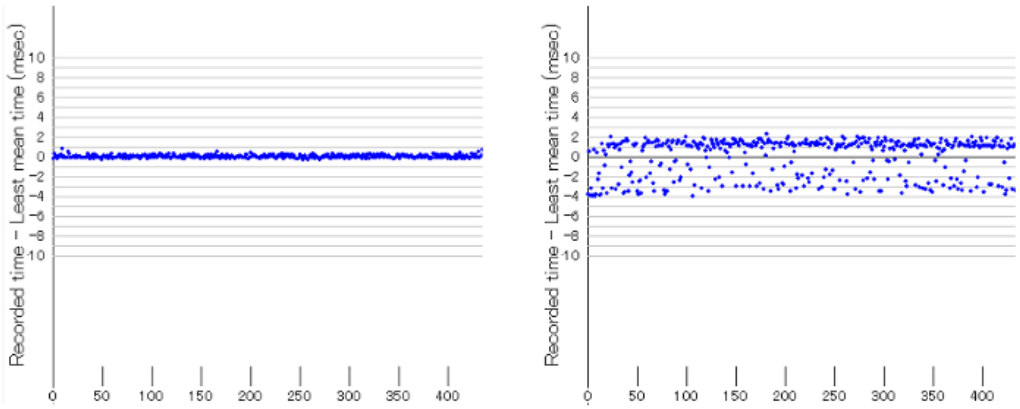

Figure 21: Changes in the time recorded by the capture software in the frame images. The horizontal axis is the frame number. Since frames are output at regular intervals, the time at which a frame is output should advance at a constant rate. However, because the time required by the PC to process the data varies from frame to frame, subtracting the estimated time that advancung at a constant rate from the time value recorded in the frame produces the variation shown in the figure. This variation depends on the PC and its operating environment. The left and right panels of the figure were measured on different PCs. It is not clear at this time what specifications and conditions of the PCs are responsible for this variation.

of milliseconds per hour for large oscillators. In addition, because of the transfer and processing time required between the time the data is output from the camera and the time the capture software reads the data and prepares to write the file, the time value written to the file is later than the time when the frame exposure is completed. The amount of this "delay" varies from frame to frame and is not constant because the PC has multiple processes running and the capture software cannot occupy the CPU, so some frames may be processed faster than others, or some frames may be processed later than others, depending on timing. To avoid such a situation, do not run any software other than the capture software during observation, so that the capture software can occupy the CPU as much as possible. Otherwise, frame dropping may occur due to the processing capacity of the PC being exceeded when continuously repeating capture with very short exposure times.

Thus, the time value written by SharpCap may contain an error of 100 milliseconds or more with respect to the time of the end of the camera

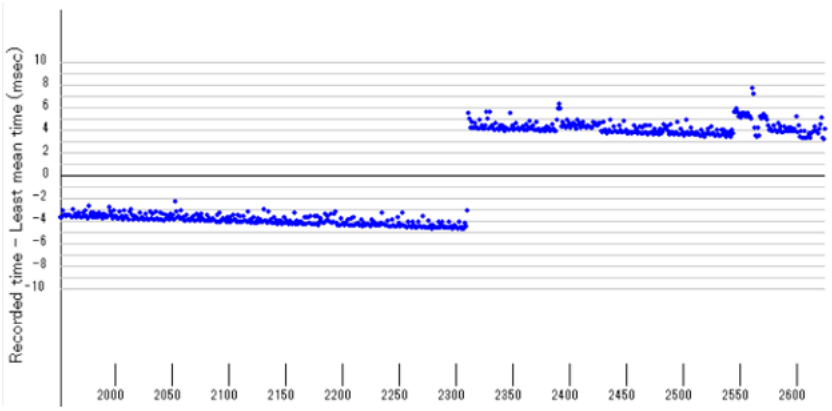

Figure 22: The difference between the average advance in time when a frame drop occurs and the time recorded in each frame.

exposure, even if the PC system clock is well synchronized. Therefore, the PC system clock cannot be used directly for precise time observations of occultations. However, it is necessary and plays an important role in the following cases.

(1) Obtaining the frame time using 1PPS LED light emission.

The method for obtaining accurate time values described in the next section requires an integer time value in seconds at a given frame. This time value must be obtained from the PC system clock time written into the captured image.

(2) Detecting frame drop

Frame dropping is a phenomenon that occurs when the capture software fails to process the captured data before outputting the next frame. The frame is missing between the previous frame and the next frame. This is a major obstacle to obtaining accurate time using the 1PPS synchronized LED light as described below. When a frame drop occurs, the gap appears on the recorded time at the point of the missing frame, see Figure (22). To avoid this, it is important to test the capture beforehand and select a frame rate that avoids frame dropping, but if this happens, the analysis must be performed by avoiding the missing frames.

(3) Not available GPS (LED) correction, which is described below. If time correction using a GPS receiver is not possible, a PC synchronized with NTP can estimate the time of the event within the accuracy of that synchronization. It is important to keep the PC's system clock as accurate as possible as a backup in case of failure.

2.8 Obtain precise time from LED light imaging synchronized to 1PPS

The frame output of a video camera is itself an accurate clock. However, the time is given as a relative number of frames and is not tied to UTC, so it is necessary to relate the frames to UTC. For CMOS cameras without a built-in GPS receiver, the method described below is currently the only way to accurately measure time.

2.8.1 Capture 1 PPS LED light with non-integer frame rate

The 1PPS LED light is a pulse signal that rises in a positive second and falls 100 milliseconds later. It is captured by a CMOS camera. If the number of frames output per second is an integer, the brightness recorded in the frames appearing at fixed intervals will be constant. Therefore, as in case A and case B of Figure 23, it is impossible to know which part of the exposure period of the frame is a positive second. On the other hand, if the number of frames per second is not an integer, as in case C, the brightness of the light in the frames at fixed intervals increases or decreases at a constant rate. By examining this change in brightness, it is possible to determine the starting point of the brightness, i.e. the positive second of UTC. The difference from this positive second can then be used to determine the time at which the exposure ends (see Figure 24). Limovie provides a function called SharpCap Timing Analysis to perform this process, which can accurately determine the center time and end time of the exposure for each frame.

2.8.2 Frame rate and the recording time of the LED light emission

Here we define that Ex: Frame Exposure Time (msec) = Frame Output Interval, Sh: Shift amount of the PPS signal in the frame (msec), Rn: LED recording time to complete one shift cycle (sec), An: The number of seconds (dots) in the shift where the light increases (decreases), L: Minimum LED recording time (seconds), the amount of shift of the PPS signal in one frame, the LED recording time to complete one cycle of shift. Then the minimum required LED recording time, and the number of seconds (points) in which the shift appears as an increase (decrease) in light intensity can each be expressed as follows.

$$Sh = Abs(1000 - Ex * Round(1000/Ex, 0)) \tag{5}$$

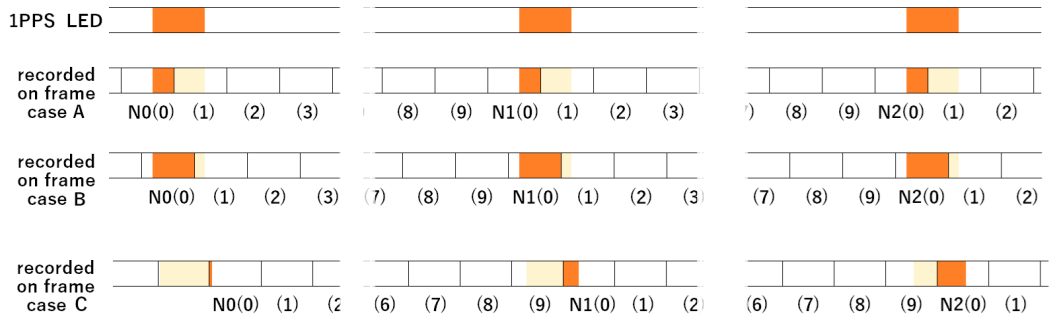

Figure 23: The frame rate and the recorded 1 PPS of LED light; the light intensity of the LED light recorded in the frames at 10 intervals is shown in orange. When the frame rate is an integer (Case A, Case B), there is no change in light intensity, but when the frame rate is not an integer, the brightness changes at a constant rate.

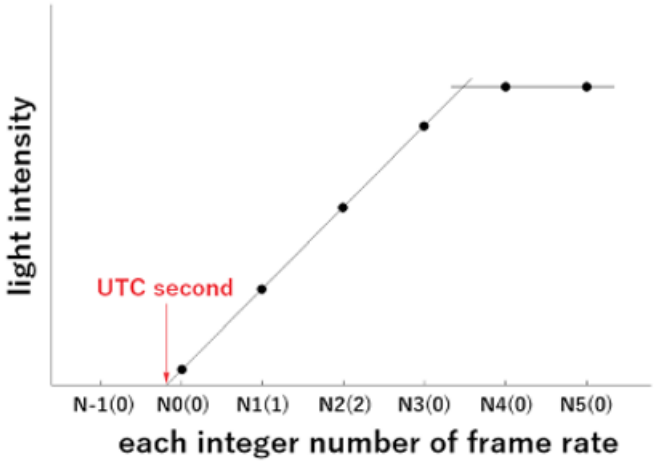

Figure 24: Frame rate and the recorded 1 PPS LED light. The light intensity variation of case C in Figure 23 is shown in the figure.

$$Rn = RoundUp(Ex/Sh, 0) \tag{6}$$

$$L = 2 * Rn \tag{7}$$

$$An = Min(RoundDown(Ex/Sh), RoundDown(100/Sh)) \tag{8}$$

These formulas are expressed using EXCEL functions. The reason why L is twice as large as Rn is because the timing of recording the LED is sometimes recorded from the middle of the brightness increase (attenuation), for completing the recording of the LED brightness increase (attenuation) shown in Figure 24, L should be twice as large as Rn.

For Rn we want to ensure at least 3 seconds (points) as shown in figure 24. For example, if L is 300, it will take 300 seconds = 5 minutes to record the LEDs, which will not only overwhelm the preparation time during the observation, but also require a lot of effort during the analysis. In addition, as Rn increases, the slope of the light amount increase (decrease) becomes slower, and the error in the time of positive seconds, which is the intersection of the shaded line and the horizontal axis of the graph in Fig.24, becomes larger. LED exposure support software CaSEDLEP is available to set Rn to about 5—20 times (see below). In this way, the exposure time of the LED light will be about 30 seconds, which does not exceed the observation preparation time.

For example, since LEDs emit light for 100 ms, if Sh is 50 ms, the light amplification is $100/Sh = 2$, which means that only two light amplifications can be obtained. Long exposures requiring this amount of shift are not normally used, but in some cases it is necessary to keep this in mind.

An example of the settings is shown below.

example setting

If Ex is 41.8 ms,
Sh = Abs(1000 – 41.8*$Round$(1000 / 41.8,0))
= Abs(1000-41.8 $*$ 24) = Abs(1000-1003.2) = 3.2
Rn = $RoundUp$(41.8/3.2,0) = 14 (times)
L = 28 (sec)

Since it is difficult to calculate appropriate values for various different frame rates, it is recommended to use CaSEDLEP (Calculation of Suitable Exposure for Decision of LEd's Pulse light), a software program that helps to determine the exposure time.

2.8.3 Measure "multiple sets" of LED light increase (decrease)

To realize the above method, the frame exposure time must be chosen so that the frame rate is not an integer, and the LED light increase (decrease) must be recorded several times so that a graph like Figure24 can be drawn. This is an important setting for occultation observations, and the method is described below.

The oscillator that controls the timing of the camera's frame output is very stable, and the camera itself is a highly accurate clock. However, the camera has no way of knowing the time value, and the frame output interval is specified by the capture software, but is not output as a numerical value. This situation can be expressed by the following equation.

$$Tn = To + Ex \times n \tag{9}$$

Tn is the time representative of the nth frame (here assumed to be the frame exposure center time), To is the exposure center time of the 0th frame (first frame), and Ex is the frame exposure time (frame output interval). Since To and Ex are not available from the video frames output by the camera, they are unknown. Therefore, if we determine the positions of positive seconds at at least two arbitrary locations on the video using LED light as described above, we can accurately determine To and En by a simultaneous equation. If more locations of positive seconds can be determined, the least squares method can be used to further improve the accuracy.

2.8.4 Area of LED light emission on the image and temporal stability of LED light

As mentioned several times before, a rolling shutter video camera must be able to capture LED light from the top to the bottom of the image because the image capture time is slightly different at the top and bottom of the image. The LED light does not need to be uniform across the image; it just needs to "shine". On the other hand, it is important that the brightness of the LED light remains constant while the LED light is blinking. This is the same for all shutter types.

Figure 25 shows an example of the illuminated area of the LED light. There are two methods of illumination: one is to illuminate the entire video image (bright-field illumination), and the other is to illuminate a part of the image (partial-illumination). Bright-field illumination requires the LED light emitters to be securely attached to the end of the telescope tube, but it is a relatively simple method. If the distance between the reducer or reducer

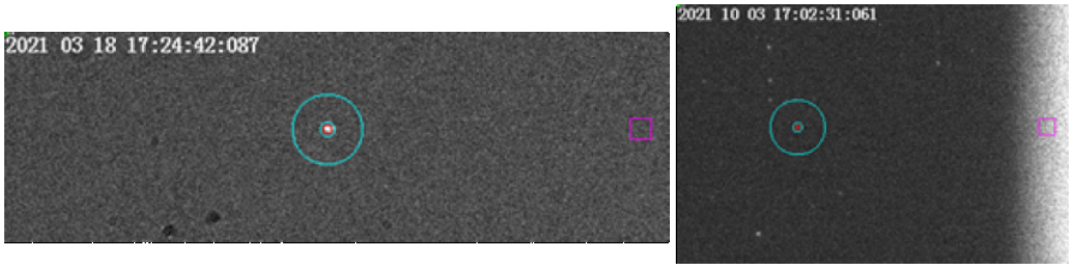

Figure 25: Area of LED light emission. Left: brightfield-illumination was performed at the end of the telescope tube; the entire field of view is illuminated by the LED light. When using this method, the LED light is recorded before/after the timing of the occultation event so as not to interfere with the occultation recording. Right: Only the right side of the image is illuminated by modifying the off-axis guider, which is a prism placed at the edge of the field of view in front of the camera to guide the star image to a guide camera installed orthogonally to the optical axis to obtain a point image of stars when taking astrophotographs with long exposure times. With this method, the flashing LED light can be captured even during the occultation event.

optics and the image sensor is short and there is no place to install a partial illumination device, you have to choose bright-field illumination.

Partial illumination, on the other hand, is somewhat more difficult to set up in terms of the size and position of the LED light emitter, but it can emit light even during occultation, which is somewhat advantageous in terms of time measurement accuracy. Partial illumination also reduces the recording time required for observation.

2.8.5 If only one LED light brightness increase (or decrease) could be recorded

Although it does not happen very often, such a situation can occur, for example, when the LED light increase is recorded only before the occultation event, and a frame drop occurs shortly after the light increase. What to do in such a case? As shown in Figure 17, the PC system clock is not very accurate. However, if the frame drop happens within a few minutes, the error is expected to be 1-2 milliseconds or less. Therefore, only Ex in the equation (9) is obtained from the PC system clock value recorded at the time of capture. Specifically, it examines the advance of the PC system clock for the interval in which no frame drop has occurred, and then calculates Ex. Since the time between the LED light and the occultation event is shorter

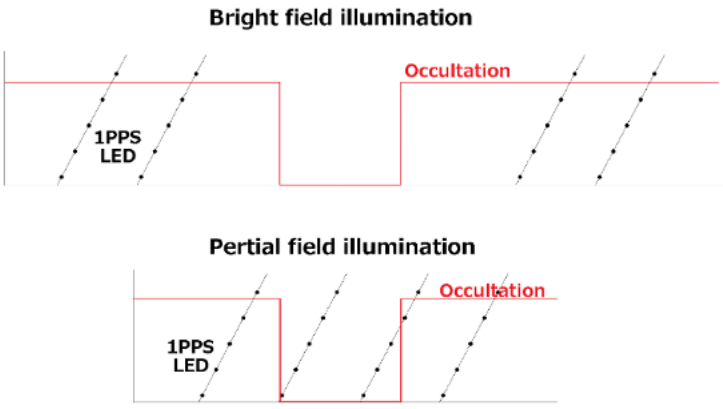

Figure 26: Illumination method and duration of LED illumination. Above: Recording LED light with bright-field illumination. LED light cannot be recorded during an occultation event because it interferes with photometry. Therefore, LED light emission is recorded before and after the event to improve the accuracy of time determination. Bottom: When only the right or left edge of the image is illuminated, the LED light does not "interfere" with the brightness change of the target star, so the LED light can be continuously illuminated and recorded.

than the interval examined, the time can be obtained with relatively high accuracy. Limovie, described in the chapter 5, checks the recorded value of the PC system clock at the frame drop search step, calculates a preliminary Ex, and uses it for the time calculation, even if only one set of LED light increase/decrease is used.

2.8.6 If LED light is not available

If the LED light cannot be obtained correctly due to malfunction of GPS-related equipment, etc., you have no choice but to rely on the PC system clock mentioned above. If the PC system clock is accurately synchronized to UTC, the time is obtained assuming the PC system clock is accurate. The problem then is that the timing of the capture varies from frame to frame, as shown in Figure 21. To solve this problem, we can assume that the PC system clock advances at a constant rate and find the average advance. Specifically, the PC system time captured in the frame is approximated as a linear function using the least squares method. If we measure the time required to capture the same PC and camera with LED light on a different occasion than the observation, we can use this as a correction value to obtain

a “relatively” correct occultation time value.

3 Observation Instruments

3.1 Using a high-sensitivity astronomical CMOS camera for occultation observations

Occultation observations have been made using high-sensitivity analog video cameras. When the target star is faint, the exposure time is extended and moving images are taken. For example, the system used by the authors (HW, HY) to observe the occultation of a 12th-magnitude star requires 32 frames of analog video (NTSC system), with a time resolution of about 1 second. Therefore, it was difficult to observe phenomena of less than one second. In recent years, a powerful observation device that can replace analog video cameras has become popular. This is an astronomical CMOS camera that can capture moving images. Back-illuminated CMOS cameras can capture moving images with much higher sensitivity and lower noise than analog video cameras. The high sensitivity of this CMOS camera can be used to shorten the exposure time when capturing occultation phenomena. The camera is also suitable for occultation observations because it is an astronomical camera, and the amount of light captured by the image sensor is output linearly, without gamma correction or other image processing corrections. In the case of occultation of bright stars, the frame rate is much higher than that of the NTSC system that has been widely used until now, and it is also possible to observe dimming of less than one second. Recently, occultation by small asteroids with diameters of 5 km or less has also become a target of observation; the successful observation of occultation by (3200) Phaethon with a diameter of about 5 km observed on October 3, 2021 (UT) in western Japan is still fresh in our memory [42]. It is also possible to obtain the visual diameters of massive stars and stars with small separation angles. This section describes the software and equipment required to perform occultation observations with an astronomical CMOS camera.

3.2 Camera control software “SharpCap”

SharpCap was developed in 2010 by Robin Glover from the UK as a webcam capture software for astronomical use (the name comes from the programming language “C#”). Today it supports a wide range of astronomical imaging hardware (cameras, focusers, filter wheels, and mounts). It is basically free software, but there is a paid version called SharpCap

Pro with additional features. The free version is sufficient for occultation observations. You can download it from the following page. https://www.sharpcap.co.uk/sharpcap/downloads
The primary reason why SharpCap is useful for occultation observations is the ability to record time on the video. Depending on the settings, time up to 1/1000sec is displayed at the top of the image. At that time, the time starting at 0:00:0:0 on January 1, AD is written as 24-bit data in units of 100ns (nanoseconds) into the eight pixels in the upper left corner of each frame of the image (see Figure 20 in the previous chapter). Analysis software such as Limovie and PyMovie can read this time value, display the time on the software screen, and analyze the occultation time. Therefore, if you use SharpCap, you should use Limovie or PyMovie for analysis. You can download them from the following links.
Limovie:
http://astro-limovie.info/limovie/program/limovie-P02.zip
PyMovie:
https://occultations.org/observing/software/pymovie/

SharpCap can also handle CMOS cameras with high sensitivity, low noise, and high frame rate as described above, and the frame size can be set freely to some extent. When observing only one or two target stars, as in occultation observations, the frame size can be reduced and even higher frame rates (higher temporal resolution) can be used. The temporal resolution of a CMOS camera is several to ten times higher than that of a conventional CCD camera, and it is possible to analyze non-instantaneous changes in light intensity due to light diffraction. The introduction of CMOS cameras to occultation observation is a great breakthrough for occultation observers.

3.2.1 Operating Environment

The target OS is Windows only, and the latest versions 4.1, 4.0, 3.1, or 3.2 is supported on Windows7sim11. Supported cameras are astronomical cameras: Altair, Basler, Celestron, Imaging Source, iNova, QHY, ZWO, and Windows Webcam compatible cameras and ASCOM compatible cameras. Since occultation observations require a large number of images with high time resolution, the use of SharpCap requires a PC that can write at high speed. The recommended PC specifications are as follows.

- CPU: COREi5 or i7 is recommended.

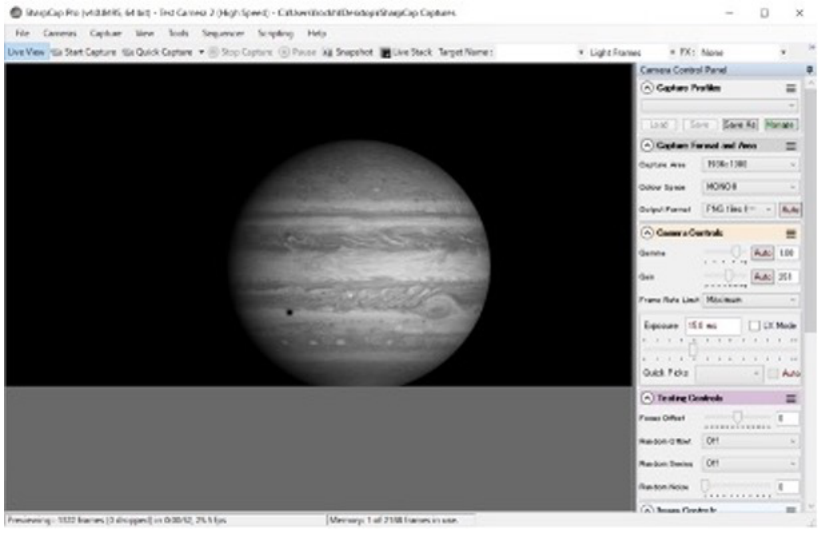

Figure 27: SharpCap4.0 Display of image captured by connecting test camera 2 (high speed)

- Memory: 8Gb or more is recommended for 64bit OS. Larger memory is safer.
- Disk: SSD (Solid State Drive) is better than existing HDD because of its faster write speed.
- USB: USB3 (transfer rate 5Gb/s) is recommended. It is 10 times faster than USB2 (transfer rate 480Mb/s) and with minimum delay.
- Windows version: 64-bit version is recommended because it can use more memory.

3.2.2 Install

The installation procedure for SharpCap is shown below.

1. Download SharpCap from https://www.sharpcap.co.uk/sharpcap/downloads. Select either the 32-bit or 64-bit version, whichever is most appropriate for your environment.
2. Go to the folder where you downloaded SharpCap and double-click Sharpcapinstall-[version-number].exe. The installation will start.

3. When the “License Agreement” dialog box appears, check the box and click the “Install” button.

4. If necessary, enter your account name and password (this is usually not necessary).

5. When the “Installation Successfully Completed” message appears, click “Close” to exit, or click “Launch” to start SharpCap.

This completes the installation of SharpCap.

3.3 Equipments

3.3.1 CMOS Camera

The most readily available are probably those from Celestron, QHY, and ZWO. Each company sells many types of cameras, but it is best to choose one that uses a monochrome CMOS chip (currently IMX290 and IMX492 are suitable) with high sensitivity (high quantum efficiency: QE), high speed (high fps), and low noise (minimum read noise of <2e) (these chips are often used for planetary imaging devices). (These are also often used as planetary imaging elements).

A 1.25” (31.7mm) diameter sleeve on the end of the camera is often used to connect to the optical tube.

When installing the camera driver, please note the following points.

1. Do not connect the camera to the PC until the driver is installed on the PC.

2. It is recommended to install the driver with administrator authority.

3. The driver should not be downloaded from the CD-ROM supplied with the camera, etc., but the latest version should be downloaded from the camera manufacturer’s website.

4. After installing the camera driver, restart Windows, connect the camera, and verify that the camera is listed under →Devices in the Control Panel.

3.3.2 Telescope tube

Astronomical telescopes such as refractors, reflectors, Schmidt-Cassegrain, and medium-telephoto camera lenses are suitable. The larger aperture, the

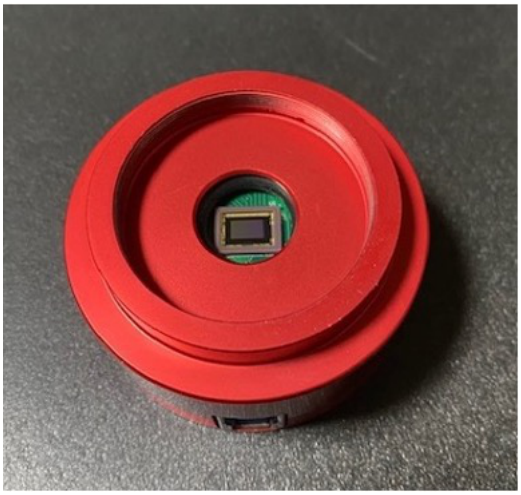

(a) IMX290 sensor on ZWO's ASI290MM camera

(b) How to attach to the telescope

Figure 28: Astronomical CMOS camera (ZWO ASI290MM). Upper: Light-receiving sensor, Bottom: Example of mounting on optical tube (with x0.33 reducer and PPS-LED light-introducing off-axis guider)

more fainter occultation phenomena can be observed, but since occultation observations are often made by traveling to the occultation zone, the optical tube should be selected for portability. The F-number (= focal length of objective lens or primary mirror/aperture (effective diameter) of objective lens or primary mirror) should be as small (bright) as possible; a small F-number gives a wider field of view, making it easier to identify the target star and select stars for comparison. A smaller F-number also makes the star image smaller, which increases the S/N ratio (more light from the star is received by each pixel of the detector element), making it possible to observe fainter stars. In the case of an astronomical telescope, it is recommended to use a reducer or reduced optics (a camera with a single focal length lens attached to the eyepiece) to reduce the F6 (preferably F4—2) (Figure 29). Recently, there have been some cases of F2 class by combining a 0.63× and 0.33× reducer on an F10 Schmidt-Cassegrain system, or F3 by combining a 0.63× reducer and a 0.5× eyepiece reducer (Figure 29). There are some cases where a 0.63× reducer is combined with a 0.5× eyepiece reducer to obtain an F3 class (Figure 30). However, when the target star is close to other fixed stars, or when the image field is bright due to moonlight and the contrast to the target star is small, it may be better to use a larger F value.

3.3.3 Telescope mount

Either an equatorial mount or an altazimuthal stand with an automatic introduction system can be used. In the case of asteroid occultation observations, the magnitude of the target star is usually fainter than 10th magnitude, so it is very convenient to have an automatic introduction system using a PC, smartphone, or tablet with a star catalog. Especially in the case of mobile observations, it is necessary to introduce the target star in an unfamiliar sky region, so it is better to have an automatic introduction system. If the automatic introduction system is controlled by a PC, it is recommended to prepare a separate PC dedicated to capturing images from the CMOS camera for the reason described in the previous section 2.7 (because the capturing software occupies the CPU of the PC).

3.4 Tools for setting the clock

In the previous sections 2.5.1 and 2.5.2, we described the PC system clock error and how to correct it using an NTP server. In this section, we describe how to use a GPS module (GT902PMGG, GT502MGG-N, VK-172, etc.) with a USB port to accurately set the time on a PC during an expedition

Figure 29: Example of a reduced optical system configuration

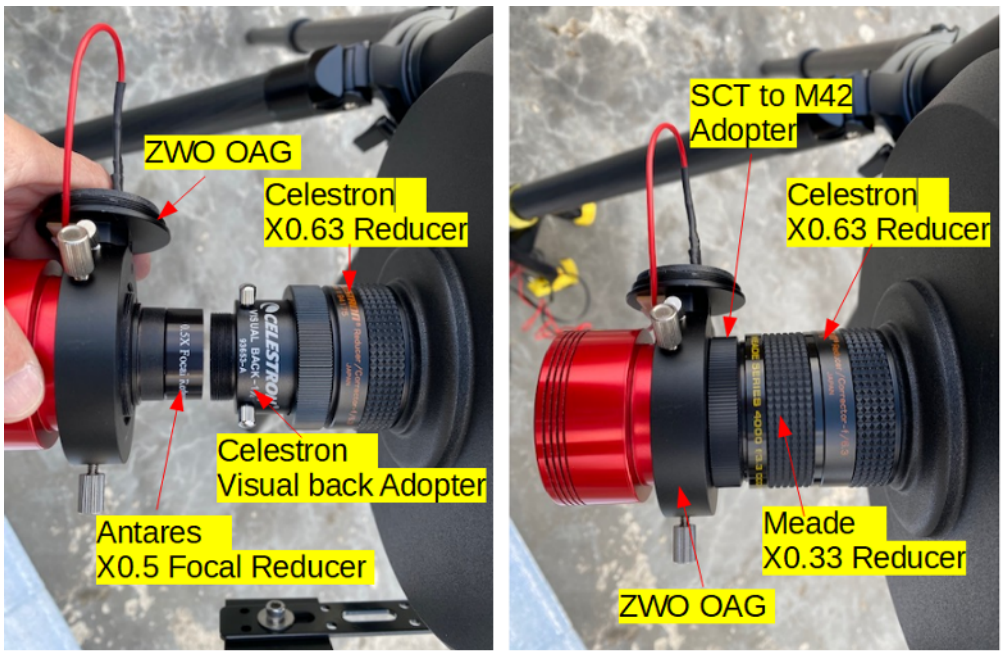

Figure 30: Examples of reducer combinations. Left:×0.63+×0.5 reducer combination. Right:×0.63+×0.33 reducer combination

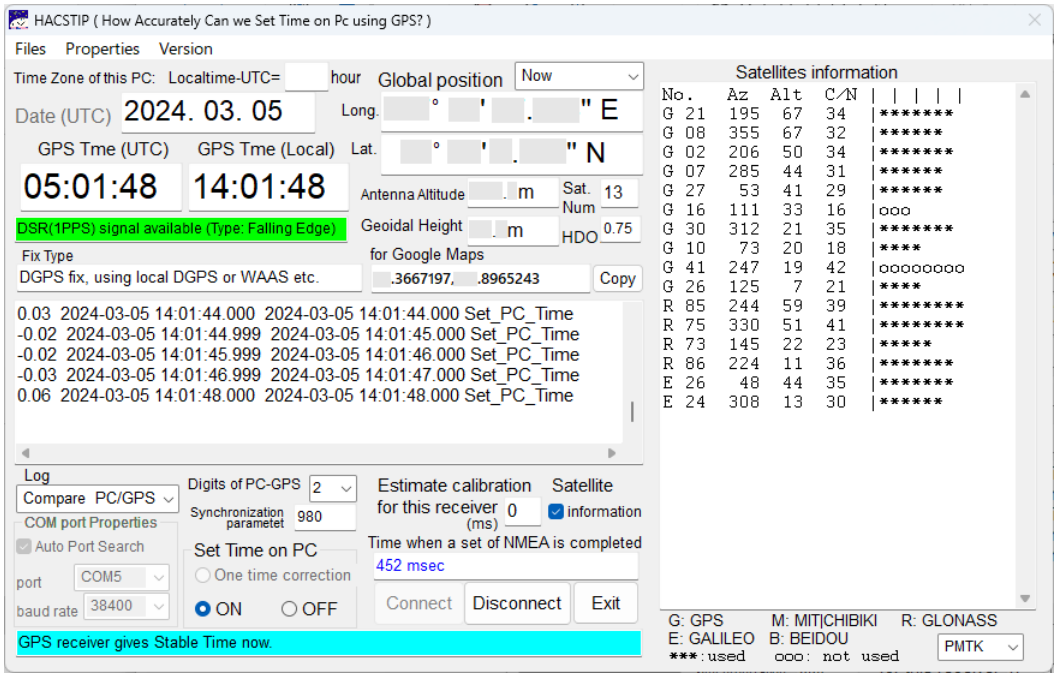

Figure 31: Time correction software for occultation observation "HACSTIP-GPS"

and to determine the location (latitude and longitude) of the observation site.

Software "HACSTIP-GPS" enables time synchronization using a GPS module. The circuit shown in Figure 32 can synchronize the PC time to UTC with an error of 0.2 milliseconds or less for receivers that can transmit a 1PPS signal to the PC via the DSR signal line. A model connected directly to the USB port (e.g., VK-172) can be synchronized to UTC with a delay of several tens of milliseconds. As for the correct time, you can get it from the NICT (National Institute of Information and Communications Technology) site https://www.nict.go.jp/JST/JST5.html or Time.is (https://time.is/

In addition, if you want to keep the PC time within a few milliseconds of standard time, you can use the following devices.

- Sheltak Instruments:「TimeBox」 http://www.timeboxutc.com/
- Sidereal Technology:「SiTechTimeServer」 https://www.siderealtechnology.com/store.html

3.5 LED light-emitting device with GPS PPS signal

To obtain the precise time of the occultation from the 1PPS synchronized LED light imaging, as described in 2.8, a device that emits LED light using the GPS PPS signal should be prepared. Figure 32 shows a GPS module with PPS output, a variable resistor (10—20 k*Omega*), a switch, LEDs, and a fixed resistor (about 330 *Omega*). Since we can control LED emission intensity, it is easy to use for observation. In addition, by placing the tip of the LED on an off-axis guider (with the optical path-changing prism pointing in the opposite direction) in front of the CMOS camera and directing the LED light directly onto the CMOS camera sensor, it is possible to capture reliable PPS luminescence. If an off-axis guide is not used, the LED can be attached to the end of the optical tube to direct the LED light directly to the primary mirror.

Those who have difficulty building this device can use a small GPS module with PPS emission function (Figure 33). The USB VK-172 GPS receiver (Figure 33) is the best choice for such a small GPS module. When used, it has a red LED (pilot) that is always on and a green LED that emits 1 PPS. Since the red LED is not needed, it is necessary to remove the cover and destroy the red LED with the tip of a cutter knife blade or the like, as shown in the left figure of Figure 33 in advance.

The GPS module is attached to the end of the optical tube using a small flexible clip, as shown in the right photo in Figure 33, to ensure stable reception of the LED light. Adjust the amount of LED light received by changing the position of the GPS module.

In both cases of the instruments shown in figures 32 and 33, it is necessary to have a mechanism to place the LED light in the optical path of the telescope for a few tens of seconds at the right intensity and at the right time before and after the observation. For observations, we use modules that emit PPS light for only 0.1 seconds. Some modules emit light for 0.9 seconds and disappear for 0.1 seconds. Such products cannot be used for time correction, so be careful when choosing a GPS module.

4 Observation Methods

4.1 Preparation for observation

From Occult4 (http://www.lunar-occultations.com/iota/occult4.htm) or the OccultWatcher (http://www.lunar-occultations.com/iota/occult4.htm) application, we can obtain the date and time of the occultation, the lo-

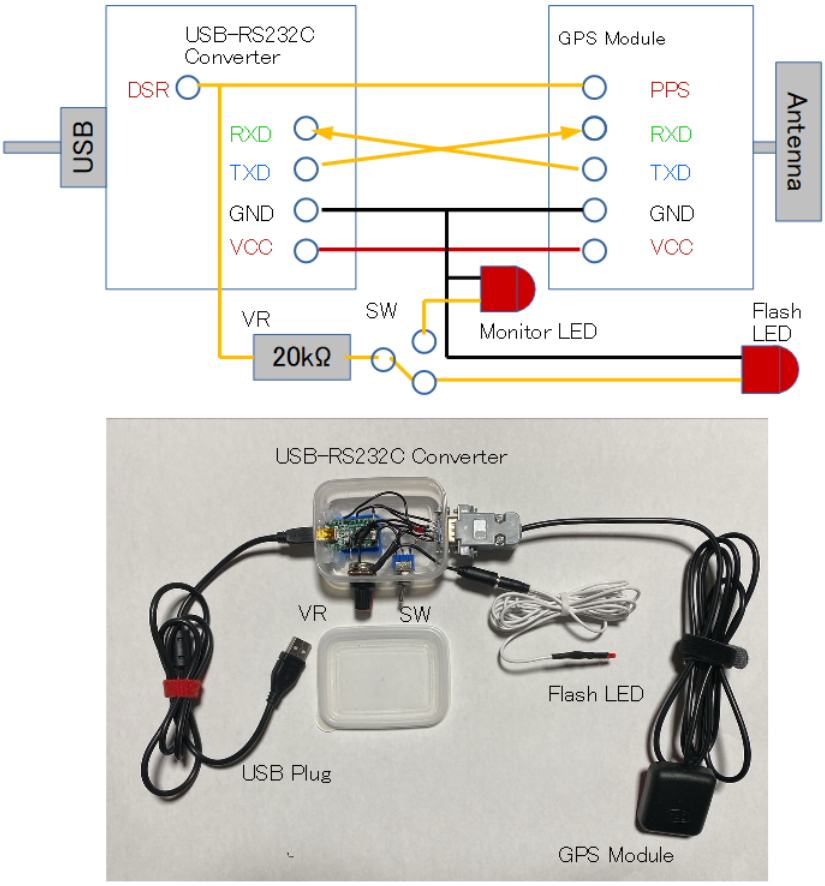

Figure 32: GPS-PPS-LED light-emitting device example and circuit diagram for self-building

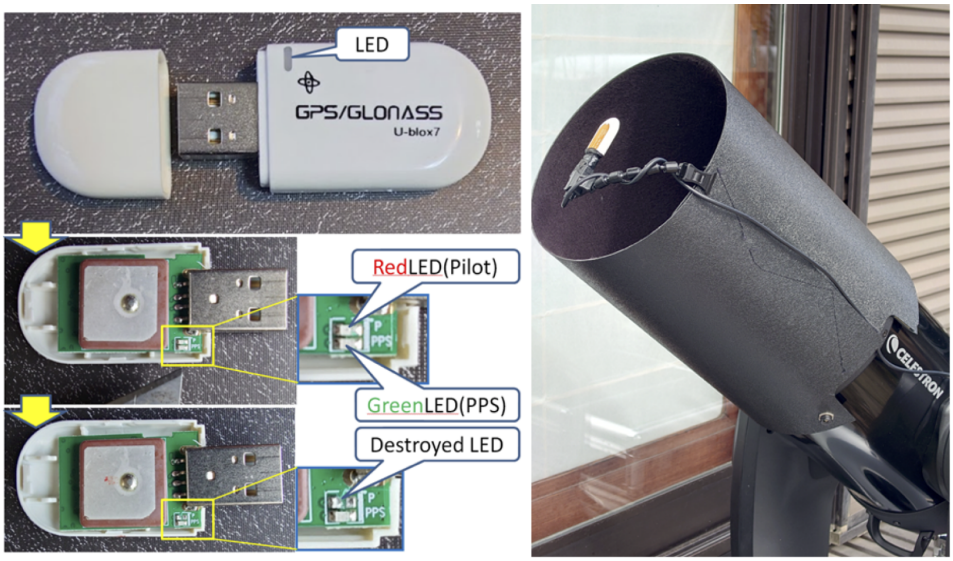

Figure 33: USB-connected GPS receiver (VK-172) and destroy Red LED (left), mounted on optical tube tip (right)

cation of the occultation zone, and then decide your observation site. First, the date and time of the occultation and the coordinates of the target star are used to determine the direction (and altitude) in the sky where the occultation will occur. The altitude of the occultation target star, solar elongation, and the distance between the Moon and the target star can be checked using StellaNavigator or, for example, https://www.not.iac.es/observing/forms/visibility/. Search for an observation site as far away from houses as possible without disturbing the surroundings by using Google Earth's Street View. If you are allowed to use a parking lot or public space, you may need to get permission in advance. Check which direction of the sky is open from the observation site and confirm that the occultation target star can be observed. In the case of mobile observation, it is important to secure a power supply. The power supply of a PC, even a notebook with a built-in battery, consumes a lot of power when connected to a CMOS camera or a GPS module. So it is necessary to obtain a 100 V power supply from a 12 V power supply of the car used for transportation using an inverter or a portable battery to prevent power failure during observation.

4.1.1 Prediction of Occultation Phenomena

The occultation predictions are available from Occult4 (http://www.lunar-occultations.com/iota/occult4.htm) and the OccultWatcher application (https://www.asteroidoccultation.com/). They provide information on the date and time of the asteroid occultation, the target star (RA, Dec), the asteroid (number and name), the magnitude (magnitude of the star, combined magnitude with the asteroid), the duration of the occultation, the depth of the occultation, and the position of the occultation zone, etc. Occult4 can derive its own predictions for various occultation phenomena, and especially for asteroid occultations, the latest orbital elements from the NASA-JPL Horizons system and the Gaia catalog provide highly accurate predictions. Occultation data is stored in XML format, and Occult4 can display a list of phenomena and a map of the occultation zones, and can also display the occultation zones in Google Earth. OccultWatcher filters the world's asteroid occultation predictions and displays events passing near the observation location. In addition, the observer can declare the location of the occultation in advance and display the occultation zone and line of sight on the map. The "ERC Lucky Star Project" of the Paris Observatory, which carries out occultation observations of TNO and Trojan asteroids, also provides predictions.

4.1.2 Selection of observation sites

Select your observation site in the occultation zone displayed on Google Earth that is suitable for the purpose of the observation. In the case of a team observation, the observation line is determined in advance according to the purpose of the observation, and a location near the line should be chosen where observation is possible. Check the surroundings using Street View or other means. The selection criteria are that the target star must be observable from the observation site, and the stars for using the telescope alignment must be visible. (2) There should be enough space for parking and observation (public parking lots, vacant lots, harbors, country roads, etc. are good locations). The location should be as far away from houses as possible so as not to disturb the surrounding area. No traffic (e.g. dead-end country roads). The sky should be as dark as possible (avoid city lights rather than nearby street lights). Toilet facilities should be nearby. Permission to use a parking lot or public place may be required in advance. For important observations, it is advisable to visit the proposed observation site in advance and consider the above selection criteria.

You may want to use large telescopes at public observatories, public facilities, and educational institutions. Large telescopes have the advantage of being able to observe faint targets, reduce exposure time, and increase frame rate. However, public observatories are often used exclusively for visual observation by the general public. You have to confirm the following things.

- Can a camera be attached to the eyepiece?
- Can a shorter focal length be used for photography?
- Can you get permission to use the observatory?

In many cases, the cooperation of the facility staff is required for observation.

4.1.3 Confirmation of target stars

Confirm the direction and elevation of the observation field based on the date and time of the occultation event and the coordinates of the target star. Check the azimuth and elevation of the target star, the solar elevation, and the presence or absence of moonlight using StellarNavigator or, for example, https://www.not.iac.es/observing/forms/visibility/. Check the field of view of the target star with appropriate photographic equipment. If you are going to use your eyes to get to the target star, you will need to create a star map with a progressively smaller field of view, showing the brightness of the star down to the fainter stars. For important observations or observations near twilight, it is better to practice guiding the target star and perform a photographic test (see section 4.4.1).

4.1.4 Secure power supply

For mobile observations, it is important to have a power supply. In addition to the power supply for the telescope mount, the power supply for the PC, even a notebook with a built-in battery, consumes a lot of power when connected to the CMOS camera and GPS module. A portable battery or similar device should be used to avoid power failure during observation.

4.2 At the observation site

After setting up the telescope mount and mounting the optical tube and camera, the PC should be booted. To initialize the PC, it is recommended to perform a cold start or reboot instead of resuming sleep or hibernation.

In addition, turn off wireless LAN and Bluetooth after startup to stop unnecessary communication. If you want to use an NTP server to set the time via wireless LAN, set the time first and then turn it off. After that, follow the steps below.

1. If you use a GPS module to set the time on your PC, turn on the GPS module 30 minutes before the scheduled time and start positioning, so that the coordinates of latitude and longitude and time will be stable during the observation.

2. Set up the telescope mount. For equatorial mounts, set the polar axis. For automatic introduction (both equatorial mount and altazimuth), ensure three-point alignment.

3. Use GPS applications (e.g. GPS Clock, BktTimeSync, NEMAMonitor for Windows) to determine the coordinates of the observation site and correct the time on the PC. To be sure, check the time signal service such as 117 (117 in China and Taiwan, 02-116 in Korea, 1711 in Singapore, etc.) to see if there is a deviation in seconds.

4. Elevation is obtained according to 6.1.2 described below.

5. Start SharpCap, right-click on SharpCap in the Task Manager and select "Show Details" → Right-click SharpCap.exe and select "Real Time" from "Set Priority" to increase the priority of SharpCap use in the PC.

6. Select the connected camera from "Cameras" in the SharpCap menu. The preview monitor will immediately display a movie image that can be captured. At this point, maximize the CaptureArea, introduce a suitable bright star, and focus the camera.

7. Introduced the target star. Even if the mount is an automatic introduction, it is necessary to perform a two- or three-point alignment beforehand. This procedure may be difficult to perform with a CMOS camera with a small light-receiving element (such as the ASI290MM), so it is recommended to guide the target stars in sequence, starting with the brightest stars. If you are using an electronic finder that can detect stars down to about 10th magnitude, you can introduce the stars even more smoothly.

4.3 Setting parameters for SharpCap

This section describes the SharpCap settings. Figure 35 shows the capture screen of SharpCap. The right panel is the control panel, and the following settings are made in each panel.

< Capture Format and Area >

1. In "Color Space", select either [MONO8] (8bit) or [MONO16] (16bit, but actually about 12bit) because monochrome images are recorded. [MONO8] records a smaller amount of data. Even when using a color CMOS camera, it is better to record in MONO because the data size is smaller and the PC memory is less compressed.

2. In the "Capture Area" it is better to make the screen as narrow as possible, especially in the height direction, to record at a high frame rate. However, if only the target star is captured, it cannot be distinguished from cloud dimming, so the frame size should include some nearby stars as comparison stars.

3. Binning is recommended [2]. The sensitivity is much higher than [1], and it is possible to image fainter targets with shorter exposures.

4. The default "Output Format" is [AVI files] for MONO8, and [SER files] or [FITS files] for MONO16. If Limovie is used for analysis, [AVI Files] is required. If PyMovie is used for analysis, [AVI files], [SER files] and [FITS files] are all supported.

(Note) Many people overseas use 16-bit SER or FITS for PyMovie, based on the idea that the more bits used for faint stars, the easier to analyze. This will increase the size of the capture file.

< Camera Controls >

Select the exposure time in "Exposure" or "Quick picks". To do time correction using GPS PPS emission and Limovie (ver. 0.9.99.5A(Aqua)5i5 or later) as described in section 2.8, the appropriate exposure time should be obtained by the CaSEDLEP reference software (http://astro-limovie.info/limovie/program/CaSEDLEP101.zip) or by using the derived list (http://astro-limovie.info/limovie/cmos/LEDRecTime3.pdf). The maximum exposure time that can be corrected by this method (PPS emission: 0.1 sec) is less than 500 ms. If the "Gain" setting (described below) is increased to a level where the noise does not become too large, and the exposure time is shortened to compensate for this, image capturing with high time resolution can be achieved. However, the actual maximum frame rate is greatly

affected by the specifications of the camera used, PC performance, frame size, and color space, so it is necessary to verify this in the Previewing state. After the camera is connected and displayed, the Previewing display appears at the bottom of the SharpCap capture screen, so it is necessary to confirm that there are no dropped frames (0 dropped is maintained) at the frame rate set here.

< Gain >

Adjust the gain of the camera. The higher the gain, the more faint stars can be seen. In particular, the gain changes greatly between 90% and 100% of the scale, but this also increases the noise, so the gain should be increased to a level that does not interfere with the analysis. For example, it is easier to analyze ZWO ASI290MM with a maximum gain of 400 500 than with a maximum gain of 600.

< Frame Rate Limit >

This will limit the maximum frame rate. The maximum frame rate is set by [Maximum]. It is also possible to specify a frame rate such as [480fps], but from the results of the author's (HW) check, it does not seem possible to record at that frame rate.

< Flip >

It is a function to flip the screen horizontally or vertically. It is easy to identify the target star by setting the image to be the same as that of a star map.

< Turbo USB >

Setting to "AUTO" is said to reduce frame dropping, but may result in a loss of frame rate.

< High Speed Mode >

It is said that setting High Speed Mode to "On" may improve the frame rate in some situations. It is also said that High Speed Mode "On" can produce noise when the gain is set low. In the author's (HW) experience, it seems that setting it to "OFF" produces less noise in the ZWO ASI290MM, and setting it to "ON" is better when frame dropping occurs in high-speed recording of 10 ms or less.

< Hardware Binning >

This is a mode in which the binning is done by the camera itself, not by the camera driver. Both gain and noise are increased, and the frame rate is also increased (depending on the camera type, the selection may not be displayed).

< Image Controls >

"Timestamp Frames" must be set to "On". This will record the time. The time is displayed to the nearest 1/1000th of a second in the upper left corner

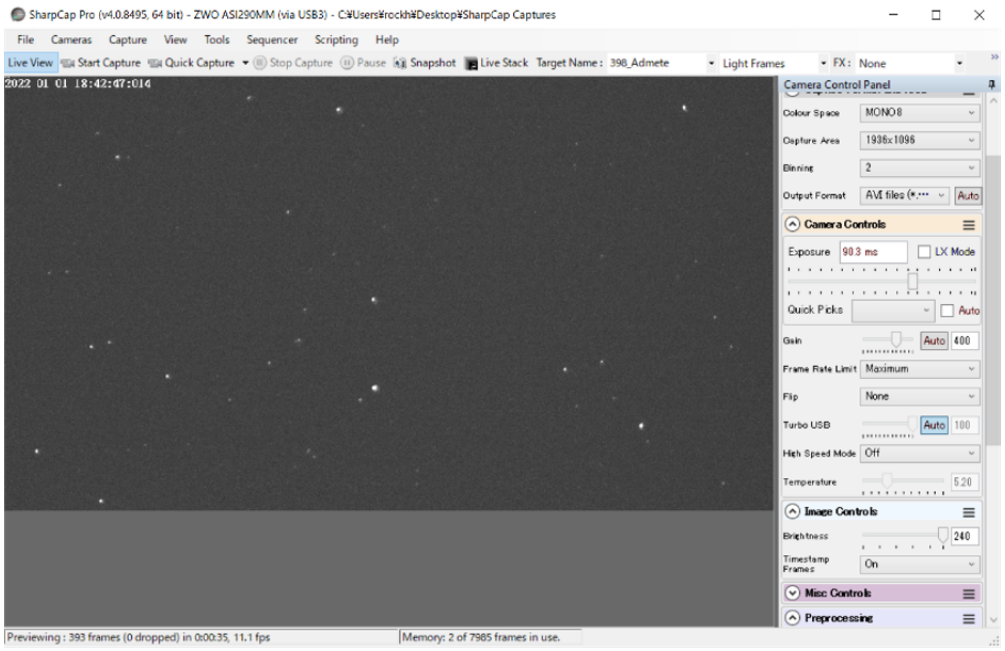

Figure 34: SharpCap capture screen. The right side is the control section, where settings are made as described in the main text.

of the screen. In addition, time data in increments of 100 nanoseconds is written into the left 8 pixels in the upper left corner of each frame, so that the analysis software (Limovie or PyMovie) can read this time data directly instead of the time displayed on the screen.

4.4 Observation

4.4.1 Test observation

At least 10 minutes before the predicted occultation time, take a test image for about 10 seconds with the appropriate exposure time and gain for observation purpose, and check that the count is within a few hundred to a few thousand. In particular, you need to check that the CMOS device is not saturated with light using analysis software such as Limovie. By making the exposure as long as possible within the exposure time constraints, the signal-to-noise ratio (S/N) improves and the time error during analysis can be reduced. To adjust the brightness of the LED PPS emission, it is necessary to adjust the LED brightness with a variable resistor or dimming film so that the SarpCap preview monitor is not completely white, but moder-

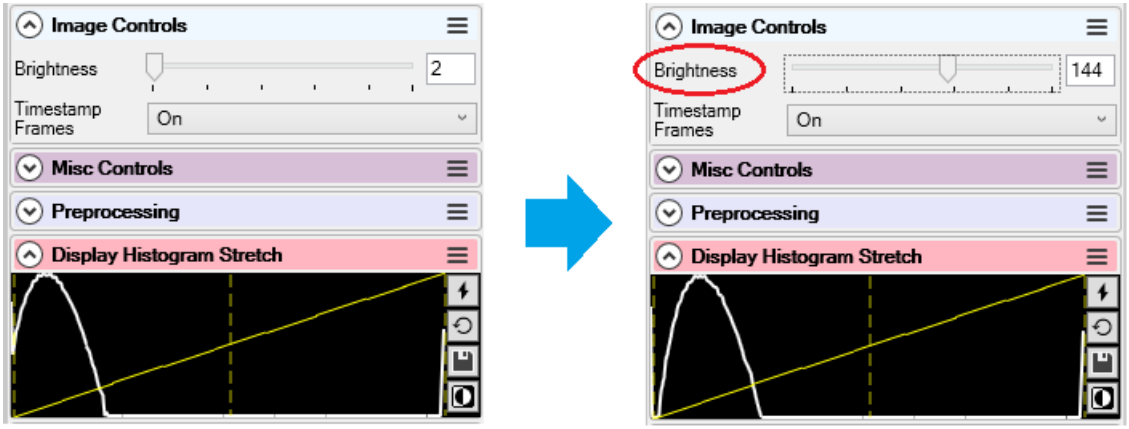

Figure 35: If the left edge of the mountain curve displayed in the histogram touches the leftmost vertical axis, increase the luminance value to move it away from the vertical axis.

ately bright. The CaSEDLEP software described above has an indicator to show the brightness of the LED light on the SharpCap monitor. As shown in Figure 36, SharpCap monitors the target star at the exposure time and gain appropriate for the imaging conditions, and the LED light of the PPS is superimposed on the monitor. Next, SharpCap displays the Braightness Index of CaSEDLEP on the monitor and compares this area with the area of the Compare LED light to the brightest LED light in the preview. Then observer can adjust the brightness of the LED light approximately equal to the recommended pixel brightness of 230 by adjusting the variable resistor. If the exposure time is very short and the LED light is not bright enough, increase the gain significantly without changing the exposure time and capture only the LED light before and after the target star.

4.4.2 Main observation

When the PPS emitter for GPS is placed at the tip of the optical tube, as the occultation prediction time approaches, the LED light of the PPS emitter for GPS is imaged at the same time as the target star at least 30 seconds before the target star is imaged. The light from the PPS light-emitting is captured for approximately 30 seconds or longer. At this time, it is possible to change the gain while adjusting the PPS emission. The target star is then imaged for 30 seconds to 1 minute before or after the prediction time, depending on the accuracy of the prediction. During this time, the LED

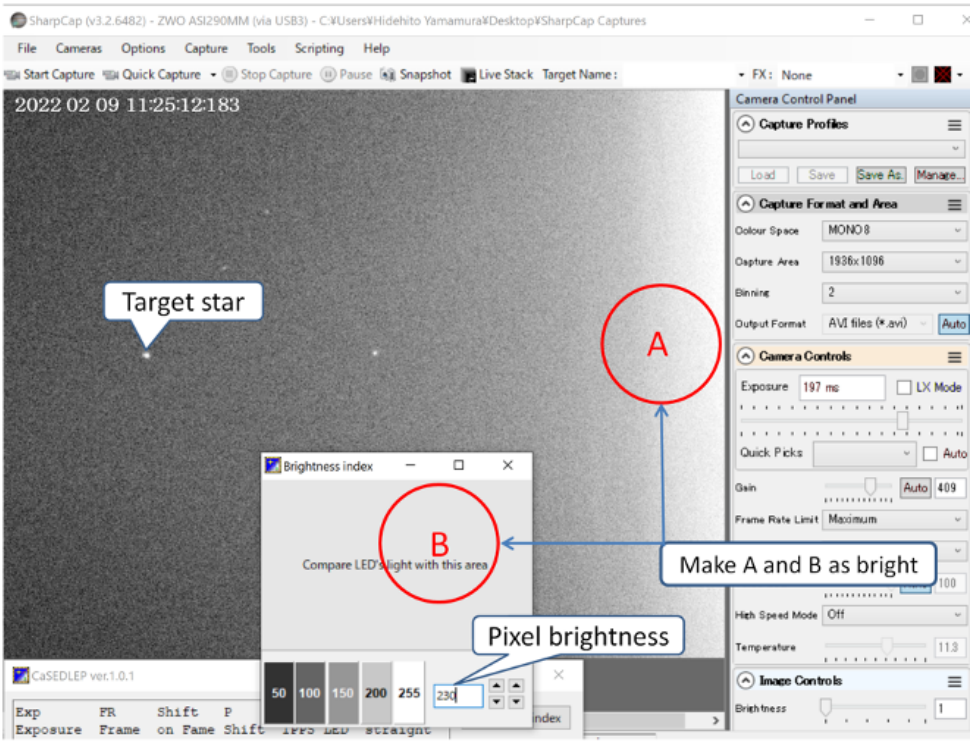

Figure 36: PPS-LED light brightness adjustment

light should not be in the field of view. Exposure time and gain should not be changed while observing the target star during the occultation. After observing the target star before/after the predicted time, record the LED emission of the GPS PPS device again for at least about 30 seconds to complete the observation. At this point, continuous recording (as a single avi file) will facilitate analysis of the results. If continuous observation is not possible, separate files can be taken if the difference is only a few minutes, but do not change the exposure time.

References

- 高感度天体用 CMOS カメラを用いた掩蔽観測の方法：星食観測ハンドブック 2020 第 1.00 版星食観測日本地域コーディネーター (JCLO) 編 http://astro-limovie.info/jclo/doccuments/Handbook/
- 天体用 CMOS カメラの露光･データ記録シーケンスの推定 (Rev. 1.02) 宮下和久https://astro-limovie.info/limovie/cmos/SequenceR102.pdf

5 Data Analysis

5.1 Fundamentals of Photometry

Video is presented as moving images by continuously displaying a large number of frames. Although video photometry can be performed with each frame as a still image, it requires some considerations and innovations that are not required for still image photometry. The similarities and differences between video and still photometry are described below. There are several software packages for photometry, but we will use Limovie as an example.

5.1.1 Measurement region and photometry procedure

First, the measuring region is explained. Basically, it is the same as in still image photometry.

The PSF measurement can determine the FWHM of a star image, and Limovie displays this value at the bottom left of the screen. If the “Fix” checkbox below the FWHM value is checked, select and click on a star with a less distorted image, the FWHM value will be saved and applied to subsequent measurements. This allows PSF photometry to be used to reduce noise over time when the atmosphere is relatively calm and there is

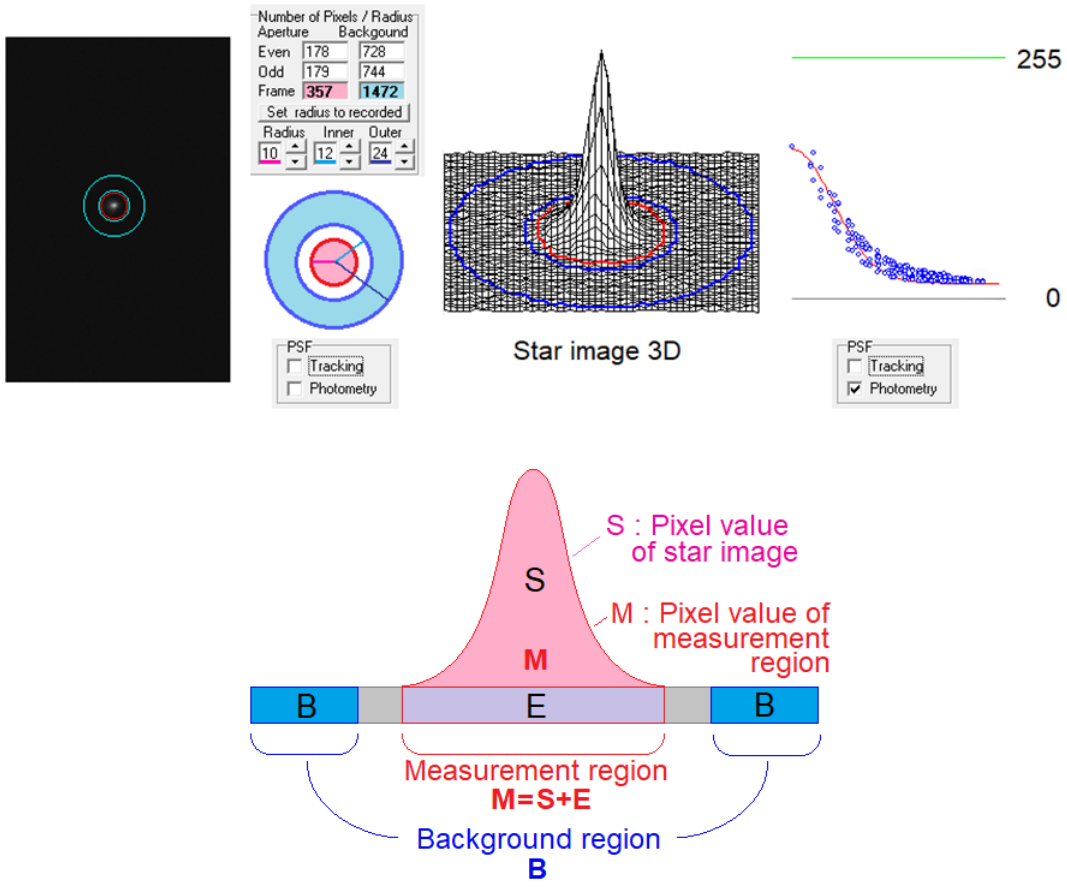

Figure 37: Measurement region on Limovie. The total pixel value S, which indicates the brightness of a star image, can be obtained as $S = M - \frac{Nm}{Nb}B$, where Nm : pixel number of the measurement region and Nb: pixel number of the background region. Aperture photometry is the simple sum of the pixel values of Measurement regions, and PSF photometry is the calculation of the pixel values by fitting a theoretical formula.

little distortion of the star images. In particular, when light levels are low during dephasing, it can reduce the effect of noise such as readout noise (noise visible as background roughness) on the image, and is effective for detecting the positional component of a massive star, etc. On the other hand, if "Fix" is unchecked, the star image and rotation curve are fitted to each frame image. In this case, the result is almost the same as in aperture photometry, so it is rarely used. Aperture photometry is effective when the stellar image is highly deformed, such as when an object is low in altitude or in a strong jet stream. In such cases, the stellar image deviates so much from the rotating ellipsoid that PSF photometry cannot properly fit the image.

As described above, it is important to use different photometry methods depending on the atmospheric conditions at the time of observation to obtain a more reliable analysis.

5.1.2 Tracking of the star images

One feature of video imaging that is not found in still imaging is the tracking function. Even if the position of a star image is determined in an image, if the star image moves in the image due to the vibration of the optical tube or the misalignment of the polar axis during observation, the star image will be out of the measurement region. In the past, photoelectric photometry was performed by preparing a fixed aperture with a large size so that the star image could enter the aperture. However, the large aperture has a large area that is not the star image, so it picks up noise in that area. Therefore, video imaging software such as Limovie has a function to align the measurement region with the star image for each frame, which is called the tracking function.

Tracking has two modes, "Anchor mode" and "Drift mode", to deal with the motion of the star image, and also to select whether to use PSF or aperture photometry for positioning when tracking the star image.

5.1.3 "Anchor mode" and "Drift mode'

Anchor mode is mainly used to track the movement of a star image caused by the vibration of the optical tube. The amount of this vibration depends on the observing conditions. The longer the focal length and the smaller the size of the image sensor, the greater the amount of movement caused by even the slightest vibration. Therefore, the tracking range can be set to different values. The system can move from a fixed point to a distance up to the tracking radius by clicking on a star image. The name of this function is

derived from the fact that a ship can only move within a circle whose radius is the radius from the point where the ship is anchored to the point where the ship's chain extends. If the star position oscillation is large, the radius value should be set to a large value. However, if there is a star brighter than the target star or a mountain near the edge of the bright side of the moon shines as a dot within the movement area defined by the radius, the measurement area may overlap with the star image within the movement area defined by the radius. Therefore, the radius should be set to avoid such overlapping.

On the other hand, if the polar axis of the equatorial mount is misaligned, the star image will move in the image at a constant speed and in a constant direction. In reality, the vibration of the optical tube adds to the image. The "Drift mode" is designed for such cases and places a measurement region at the center of the star image in each frame without a fixed point. This allows the system to track the star image even if it moves significantly during the observation period. In this case, it is necessary to set an appropriate radius value according to the amount of motion (speed) of the star image. It should be noted, however, that the drift mode may shift the measurement region to other star images, noise, or bright spots such as the limb of the moon if they are within the radius.

5.1.4 PSF tracking and Aperture tracking

To determine the position of a star image for tracking, you can use the same photometry used to measure brightness and find the point where the value is largest. Two methods are used: aperture photometry and PSF photometry. To toggle between the two, check or uncheck the Tracking checkbox in the PSF box near the bottom center of the screen. When checked, PSF photometry is used; when unchecked, aperture metering is used.

When using aperture photometry for tracking (uncheck Tracking in PSF), you can specify how much of the pixels in the star image from the peak should be used for tracking. This is done by setting the Threshold value in the Tracking frame. A value of "100" tracks only the top of the star image, while "0" tracks the entire star image. For aperture photometry, it has been shown empirically that good measurement results with high S/N can be obtained by setting the value to 95 and aligning the center of the measurement region with the bright part of the star image. This is because the deformation of the star image due to atmospheric turbulence is mainly manifested as a shift in the peak position, and setting the aperture centered

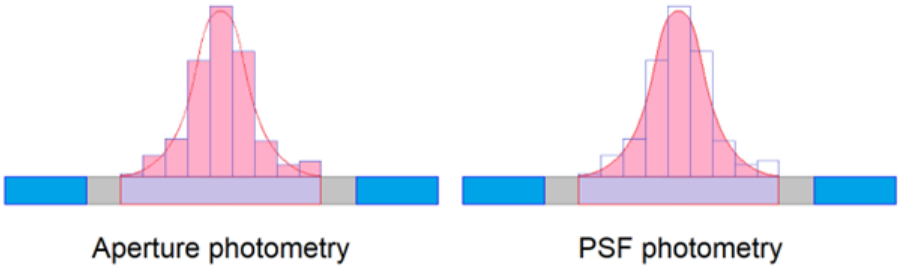

Figure 38: Aperture photometry and PSF photometry. Aperture photometry calculates the light intensity by summing the pixel values within a measurement region, while PSF photometry calculates the light intensity as the integral of a rotating Gaussian curve that approximates the peak of the pixel values. Aperture photometry is suitable when atmospheric turbulence causes large deformations in the star image (pixel value distribution deviates from the ideal state). On the other hand, PSF photometry can reduce noise over time.

on this point ensures that the "bright part of the star image", which has a large effect on the photometric value, is within the aperture. For the same reason, even in the case of PSF photometry with a lot of atmospheric turbulence, the photometric environment can be improved by setting the tracking to Aperture mode (only PSF tracking is unchecked).

On the other hand, when using PSF photometry for tracking (PSF tracking is checked), the measurement region is adjusted to the point where the star image and the theoretical curve coincide. This can be used effectively when the atmosphere is relatively calm. The bright area of the moon's limb or the base of a sudden noise will not shift the measurement region to it. This makes it an indispensable tool for lunar eclipse tracking. The threshold value is not as sensitive as in aperture metering, and the default setting of 50 is sufficient.

5.2 From the measurement of the time of the event by Limovie to the reporting of the observation

This section describes the process of analyzing video files of asteroid occultation recorded with a CMOS camera and GPS 1PPS-LED signal using Limovie and reporting the results to IOTA/EA, etc. (For the case of lunar eclipses, see the Handbook of Star Eclipse Observation. (In the case of lunar eclipses, see the Handbook of Star Eclipses).

5.2.1 Preparation

In addition to the avi file, a camera setting file named as $xx_xx_xxZ_$CameraSetting.txt is created in the folder captured during the observation. Put these two files in a working folder (you can leave them in the captured folder). Also put the prediction xml file (OccElmnt$_{*******}$.xml) created by OCCULT4 in the same folder.

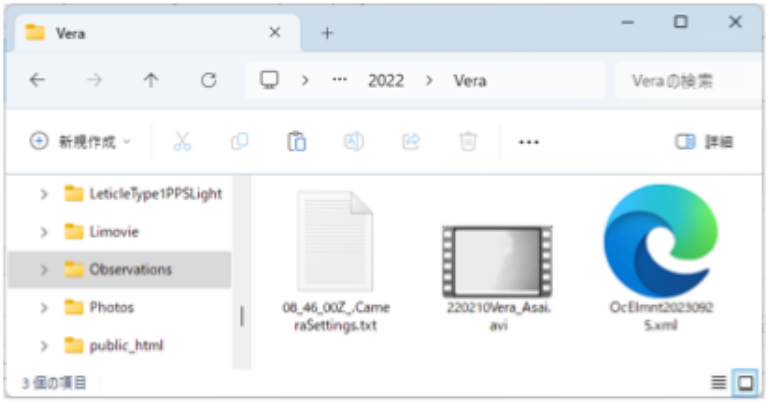

Figure 39: Where to place observation files

5.2.2 Main flow

At the bottom left of the Limovie start screen, there is a section labeled "Timing process indicator". This shows the general progress of the processing (operation). When a step (stage) is completed, the frame turns light blue from left to right to indicate how far the process has progressed. The order of Steps 2 and 3 can be reversed, but it is recommended to work in this order until you become familiar with the operation.

5.2.3 Detailed Operation Procedures

The meanings of the symbols in the following figures in this section are roughly described in Figure42.

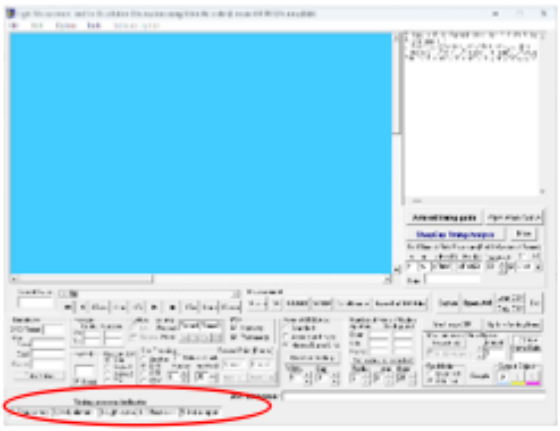

Figure 40: Limovie's startup screen

Timing process indicator

1. Time correct	2. XML element	3. Light curve	4. Diffraction tit	5. Make report

0. click the Open AVI button to load an AVI video file.
※If you click on the OpenAVI button, all the asteroid data and analysis results etc. that you have done before will be erased. However, such data will be retained unless you reload the AVI file (unless you delete the photometry data) or quit Limovie.
1. Time correct: Time correction by LEDs.
※ This is a series of operations performed by clicking the SharpCap Timing Analysis button.
2. XML element: Read various information about the phenomenon from the file Occelmntxxx.xml, which was saved in a folder at the time of preparation, and enter information about the observer and the observation location.
3. Lightcurve: Perform photometry, a key feature of Limovie. A graph will appear.
4. Diffraction fit: Calculate a diffraction simulation from the information read in 2. and obtain the time of the phenomenon.
5. Make report: Make a report (text data).

Figure 41: Enlarged view of the area circled in red in Figure 40 and its explanation

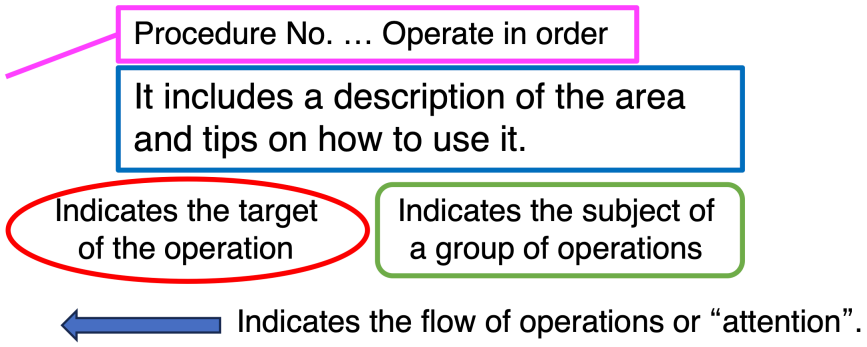

Figure 42: Explanation of symbols in the figure

Step 0. Limovie's startup screen → Open AVI → File selection
On the Limovie startup screen, click "Open AVI" (see Figure 43) to load the AVI file, then the AVI file will be displayed in the screen.

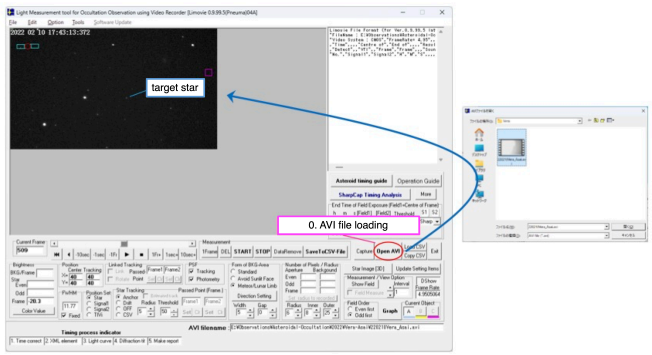

Figure 43: Load an AVI file

Step 1. Time correction

1-1. Click the star in the frame just before (or after) the event.
Leave the tracking mode at Anchor, move to a frame near the event by the slider, click the star image to display the LED light photometry area and find the frame of the star image that fits well by performing the operations shown in the right panel of Figure 45.

1-2. LED Light Photometry
The timestamp of the AVI image (see Figure 46) is the time at which the capture software receives and processes the image from the camera. It is slightly delayed from the time the image was captured. To compensate for this, the flashing LED light should be recorded at 1 PPS for the first and last 0.5 $\sim$ 1 min in the video recording of the phenomenon. The change in brightness of the LED light is measured to determine the exact capture time of each frame.

1-3. SharpCap Timing Analysis (time correction function using LED light)
The blue dots continue horizontally in figure 47 indicate whether the timestamps recorded in each frame advance at a certain rate. Here we confirm that using the timestamps as they are would result in an error of a few milliseconds. Then we move on to the next task.

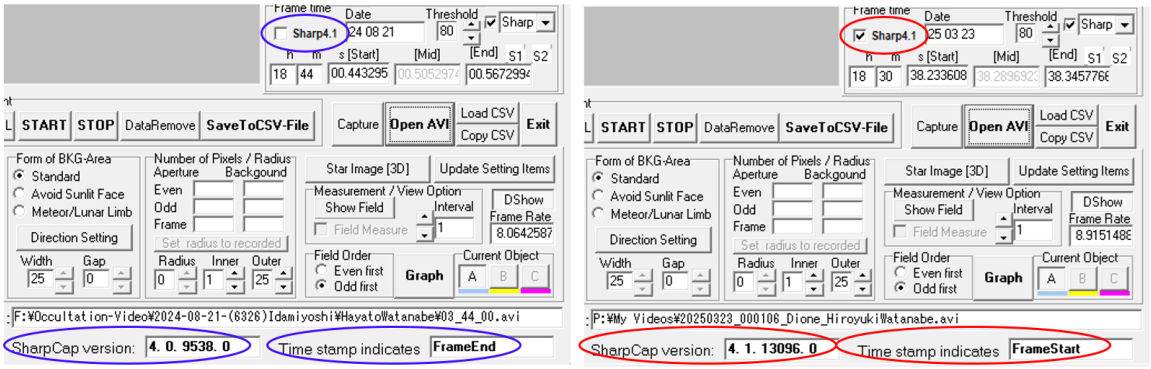

Figure 44: Depending on the version, SharpCap will show a different frame exposure position in the timestamp.
(left) Before Ver. 4.1.11756, SharpCap indicates the end time of the frame exposure
(right) After Ver. 4.1.11767, SharpCap indicates the start time of the frame exposure
After Limovie 1.0.1.8, the version of SharpCap is automatically read from the camera settings file when loading the AVI file, so the correct time can be obtained.

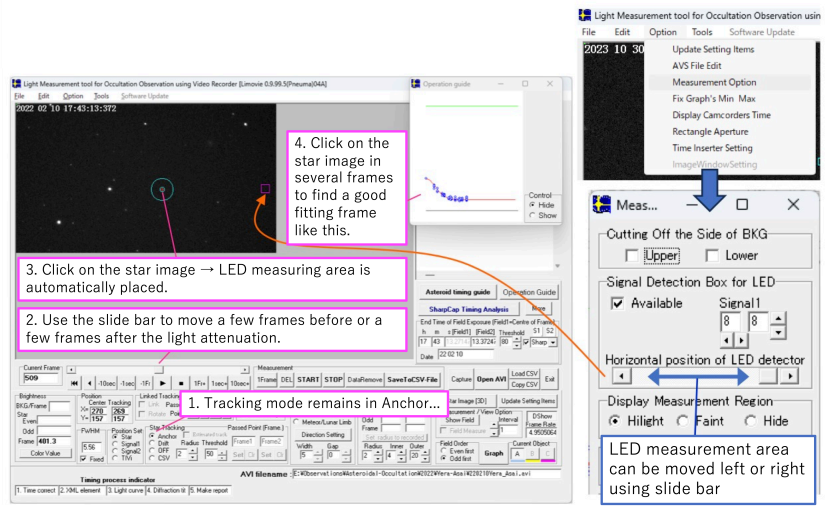

Figure 45: Preparation for LED Light Photometry

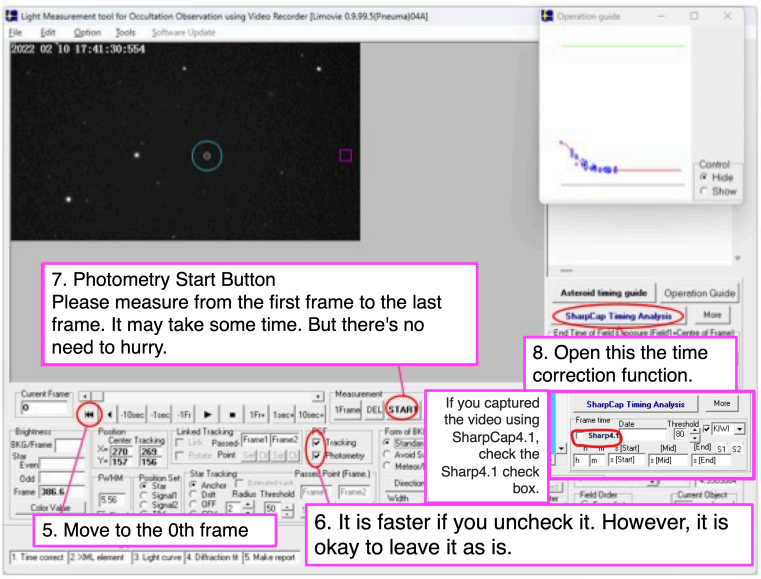

Figure 46: LED Light Photometry

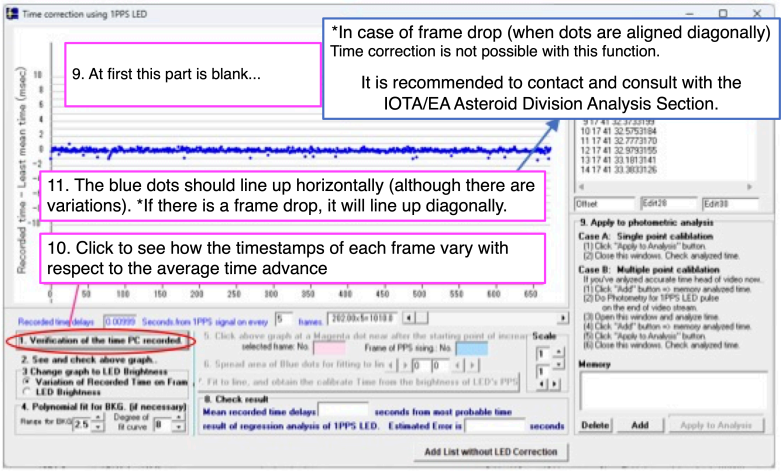

Figure 47: Screen after LED light photometry

Figure 48 is a graph showing the change in LED brightness. The magenta dots are diagonally aligned because the LED light in the image is not constant when the number of frames captured per second is not an integer. Using this fact, the position of the second is determined by the phase difference and the time is corrected accordingly (see Figures 49, 50, 51).

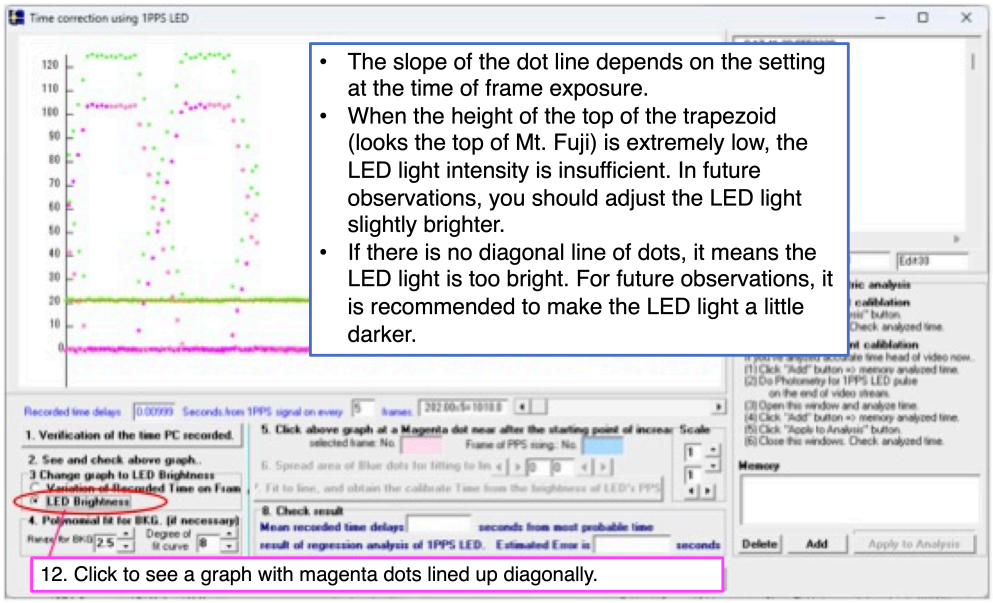

Figure 48: LED light brightness change

A calibration curve is plotted for a set of diagonally aligned points, and the intersection of the curve with the x-axis is the second. Based on this, we will know the second is ◯. ◯ ◯ ◯ ◯ milliseconds before the end of exposure of the ◯◯th frame. The data is added to the list by clicking the Add button.

Register 1 ∼ 2 pairs of listings before and after the event (at most four pairs before and after are acceptable; 1∼4 pairs either before or after are acceptable when using the HACSTIP Ver.2 series in combination with a GPS receiver that sends 1PPS signals to the PC via the RS232C DSR signal line). Click the "Apply to Analysis" button to apply the results to the analysis, and the time section of the main window will turn light blue.

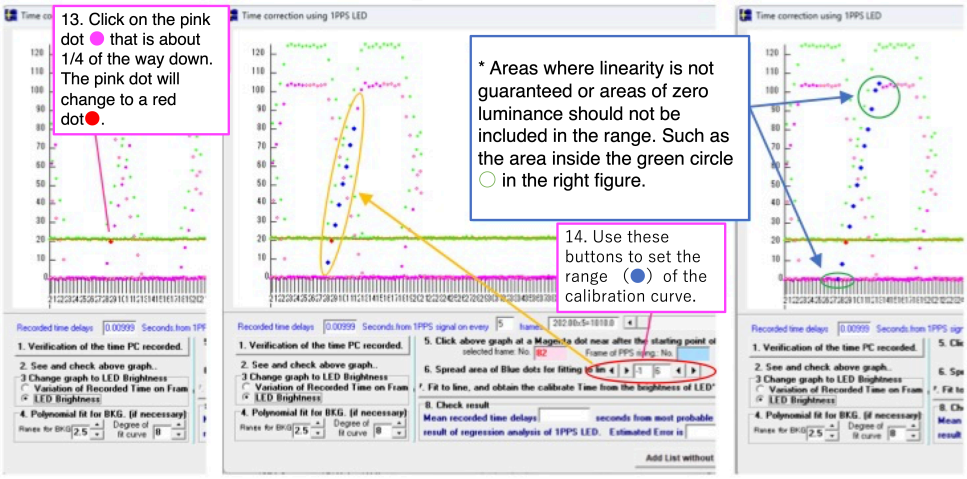

Figure 49: Operation 1 : Measurement of LED light brightness change

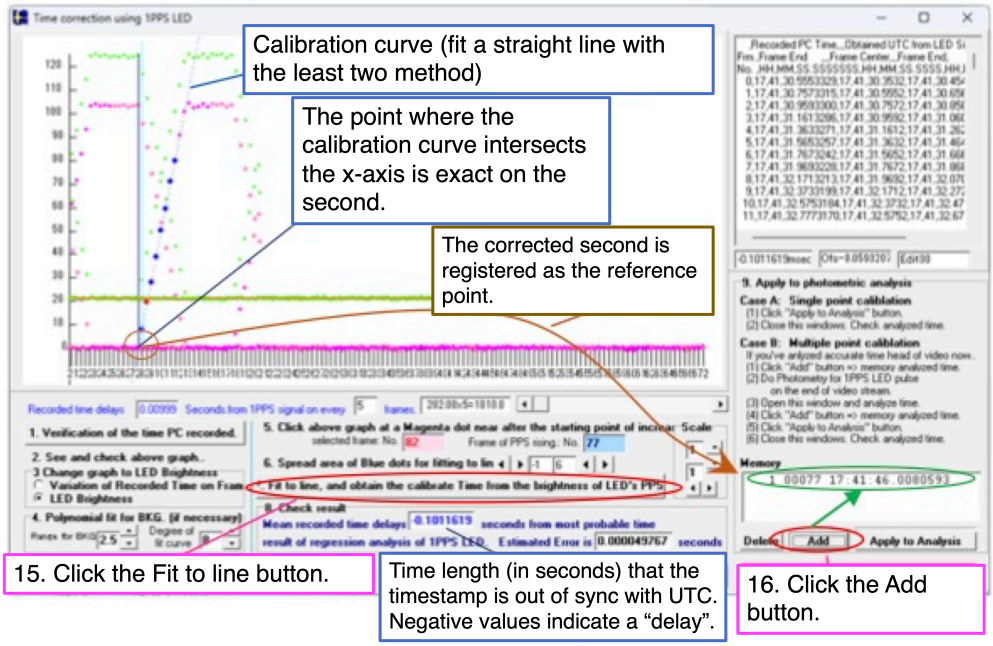

Figure 50: Operation 2 : Measurement of LED light brightness change

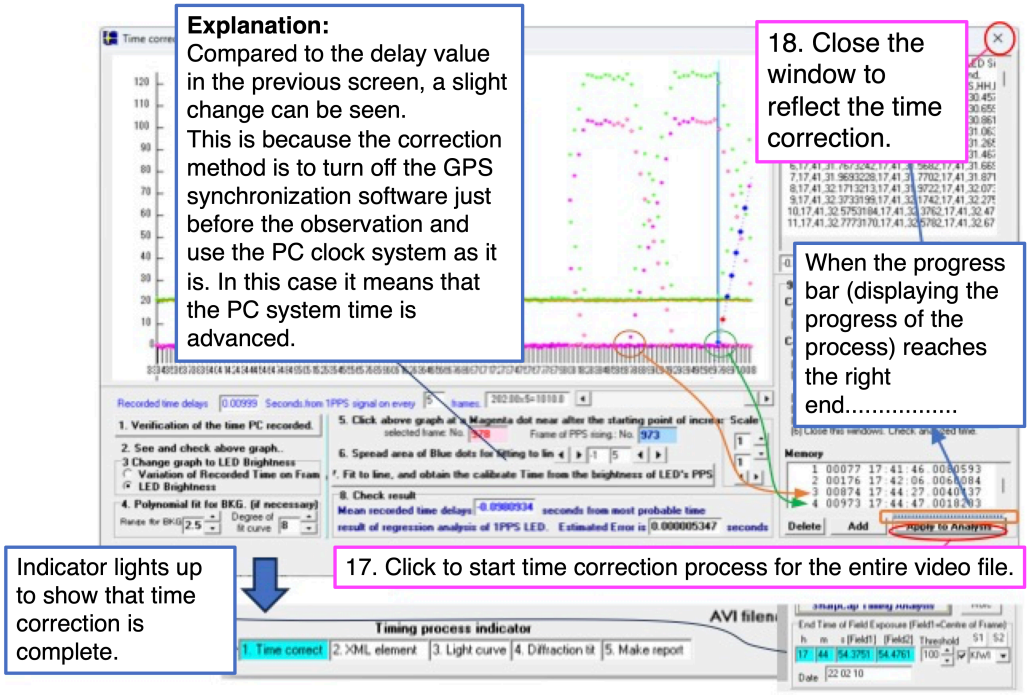

Figure 51: Operation 3 : Measurement of LED light brightness change

Step 2. XML element

2-1. Open asteroid information input screen

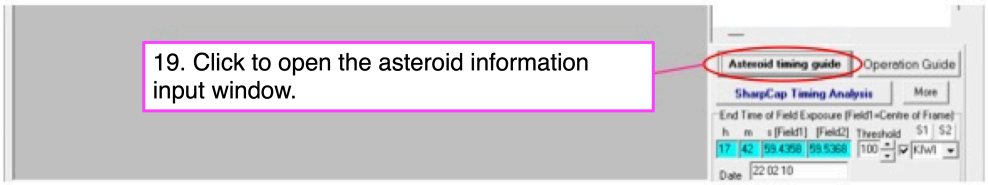

Figure 52: Asteroid information input screen

2-2. Read information about the occultation event (asteroids, stars, etc.)

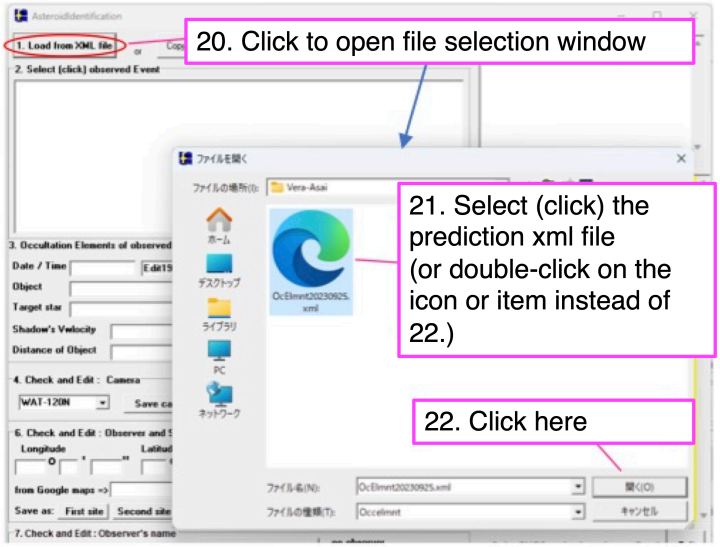

Figure 53: Read information about the occultation event (asteroids, stars, etc.)

2-3. Input observer, location, camera model, etc.

The various information entered here will be used as parameters for the calculation of diffraction simulations or as descriptions in observation reports. The information read from the xml file does not need to be changed.

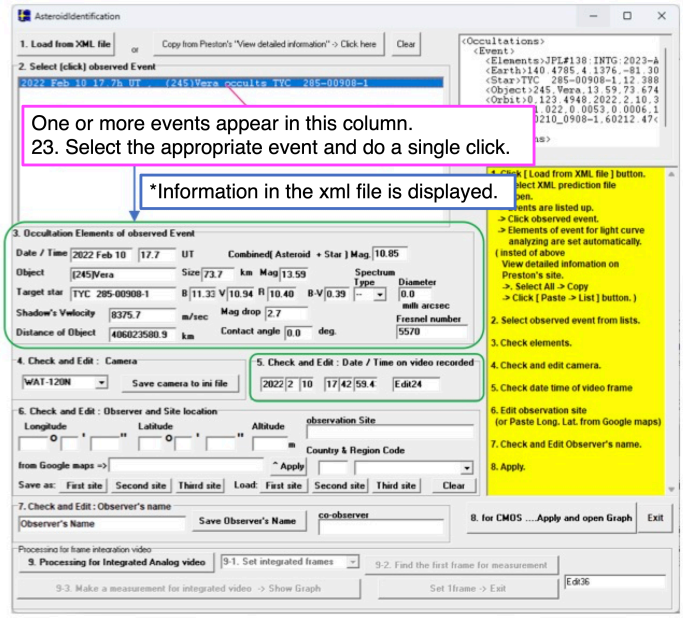

Figure 54: Reading information from xml files

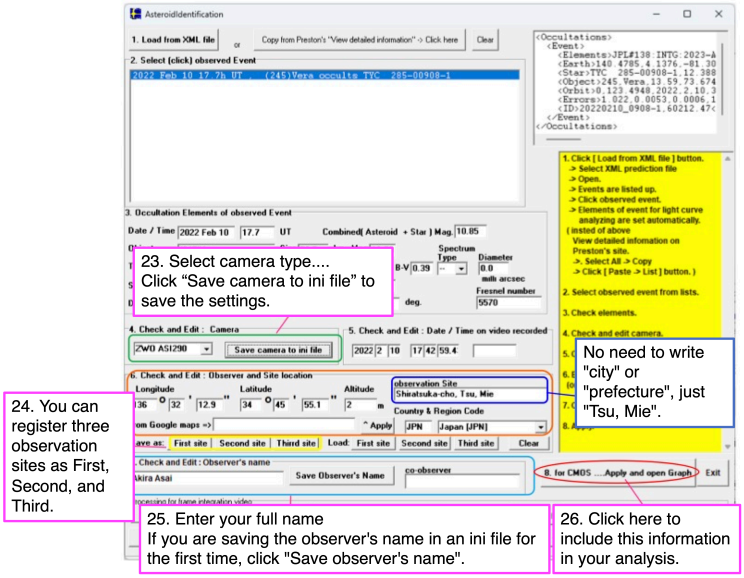

Figure 55: Save observation site information

(In the current version, once you proceed to the report generation step, you cannot make any changes there). If you save your name and observation location, they will be automatically loaded the next time you start the application. The camera information is often forgotten here: in the case of CMOS cameras, select ASI290MM. The settings can be saved by clicking "Save camera to in file" and will be automatically loaded the next time.

Step 3. Lightcurve

3-1. Photometry

Either Aperture photometry or PSF photometry can be used as the measurement method.

- Aperture photometry: A method of obtaining the average of the pixel values of the surrounding (background) pixels by area conversion and subtraction from the sum of pixel values in the central circle of the measurement region. This method is suitable when atmospheric turbulence is high.
- PSF photometry: A method of obtaining the brightness of a star by fitting a model of a rotating Gaussian curve to the actual star image. It can be used effectively when atmospheric turbulence is low or background noise is high to reduce variability.

Figure 56: Photometry of occultation events

Step 4. Diffraction fit

4-1. Preparation (setting) for fitting during disapparance

Limovie compares the light curve obtained by photometry with a diffraction simulation (a frame-by-frame value obtained by integrating the light intensity change curve due to diffraction) and selects the position that best fits the simulation as the time of the phenomenon. Visually, this means that the red curve coincides with the measured point on the graph. To compare the two, the height of the horizontal portion of the red curve before and during the disappearance must match the photometric results. The height is obtained from the area selected by •○ (green) before and during the disappearance. The simulation created in this way is compared with the photometric results, but no matter how many horizontal sections there are, it is not possible to find a match in the time direction (horizontal direction). Therefore, it is sufficient to compare 20 to 30 points across a change in light intensity. The range of the comparison is defined by textcolorblue○○. In summary, the green color represents the "height" in vertical direction and the hollow ○ represents the "comparison range" in horizontal direction.

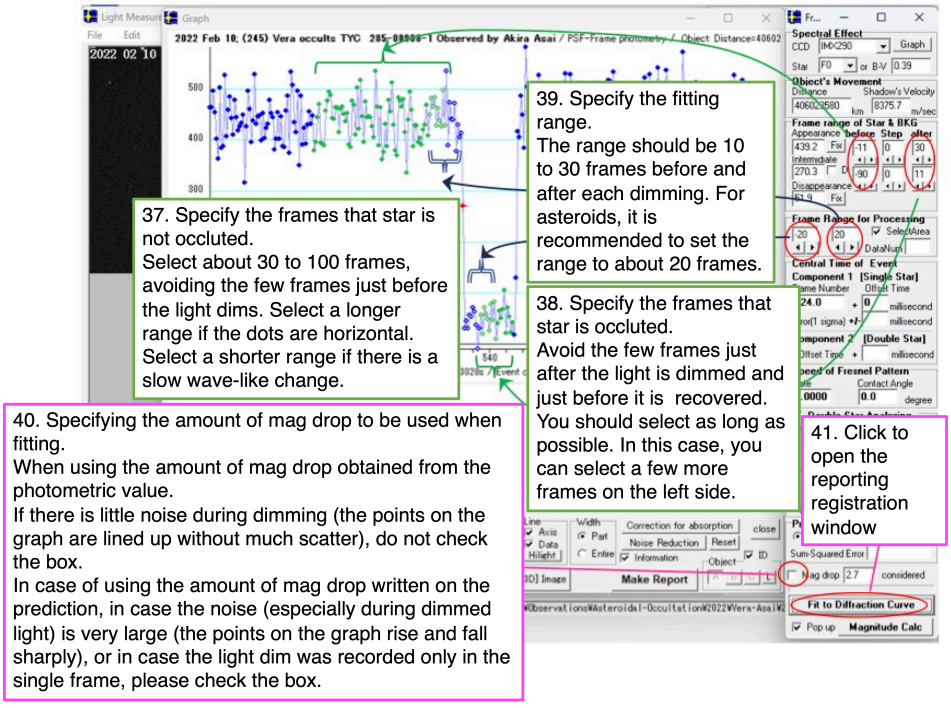

Figure 57: Preparation (setting) for fitting

4-2. Fitting and registration of the disappearance time

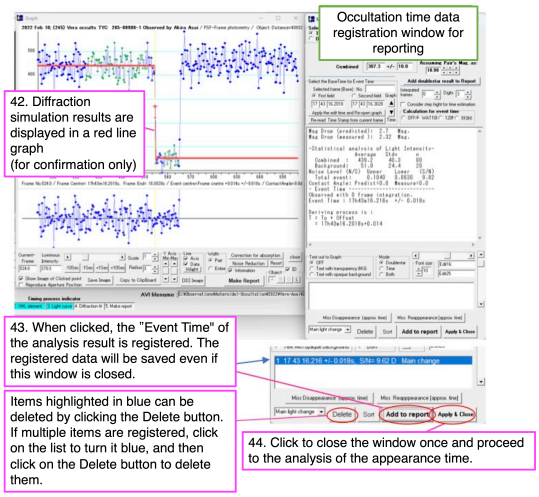

Figure 58: Fitting and registration of the event time data.

4-3. Preparation (setting) for fitting during apparance

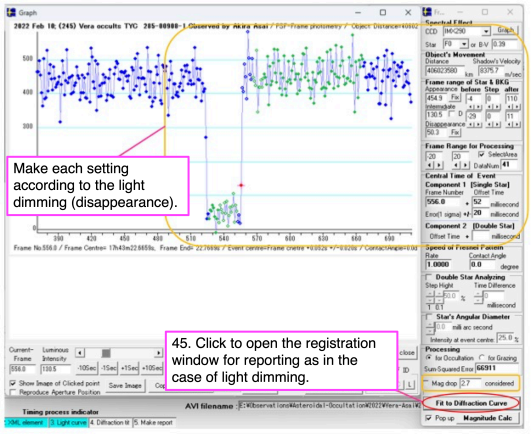

Figure 59: Preparation (setting) for fitting

4-4. Fitting and registration of the appearance time

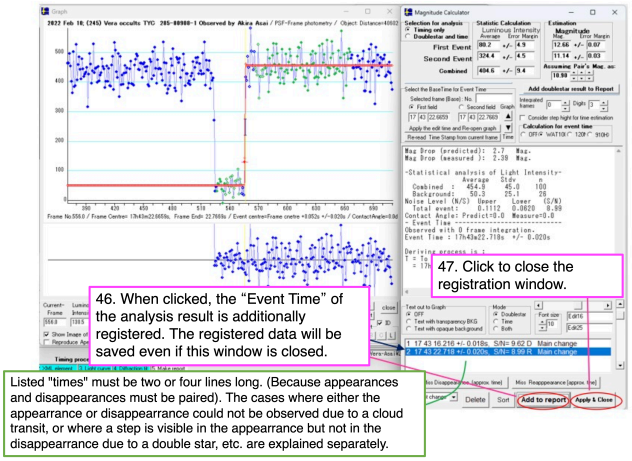

Figure 60: Fitting and registration of the event time data.

4-5. Prepare (display) graphs for text light curve data

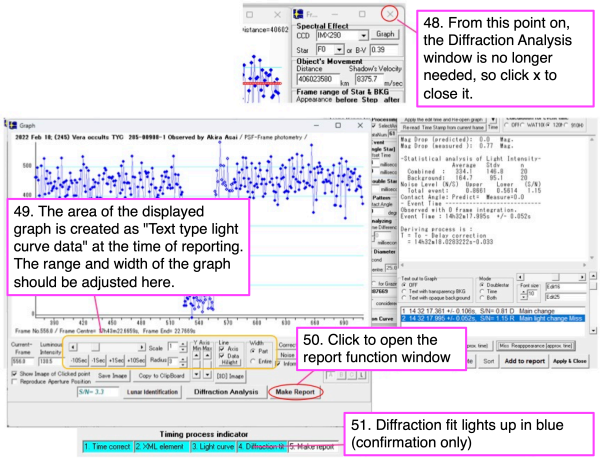

Figure 61: Display graphs for text light curve data

4-6. Special cases ... when either disappearance or appearance could not be observed due to clouds, etc.

Figure 62 shows a case where the disappearance (●) was observed, but the appearance could not be observed due to the immediate cloud cover after the occultaion event. In such a case, a dummy value is given to the appearance side, as shown in Figures 62 and 63, to create a situation where "disappearance and appearance exist as a pair", and then the Make report process is performed.

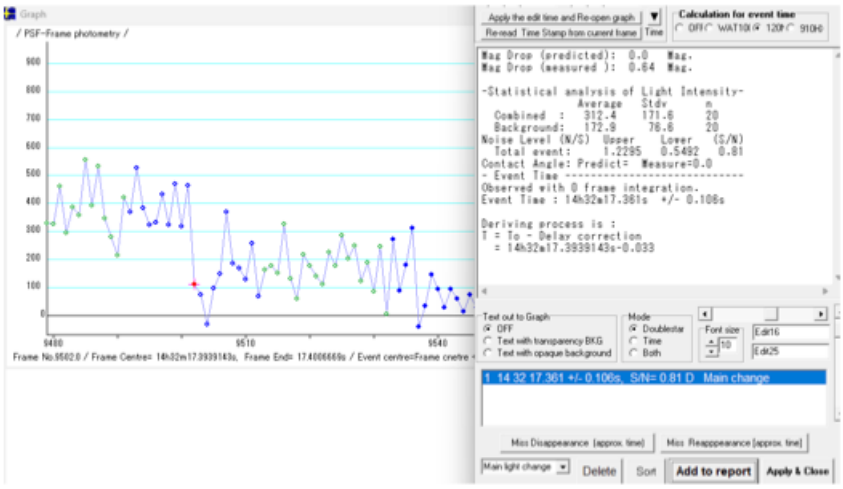

Figure 62: Disappearance could not be observed due to clouds, etc.

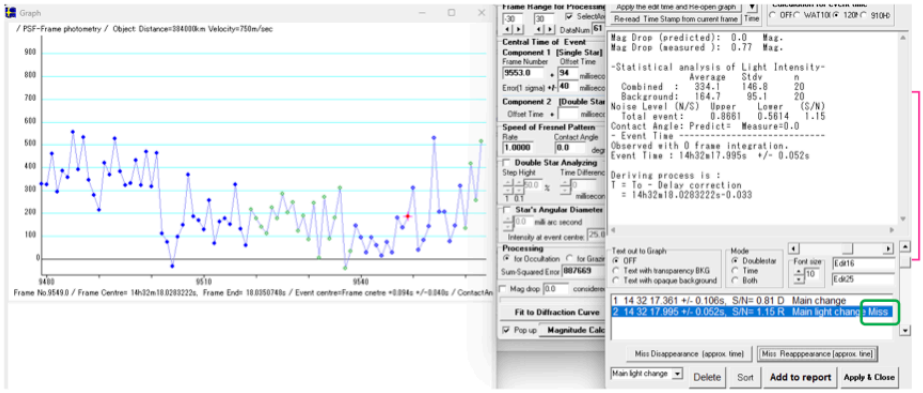

Figure 63: Give a dummy value at the appearance side

4-7. Special case ... when passing through (negative detection)

Click any location near the event time on the lightcurve, register it with "Miss", and then proceed to the report generation.

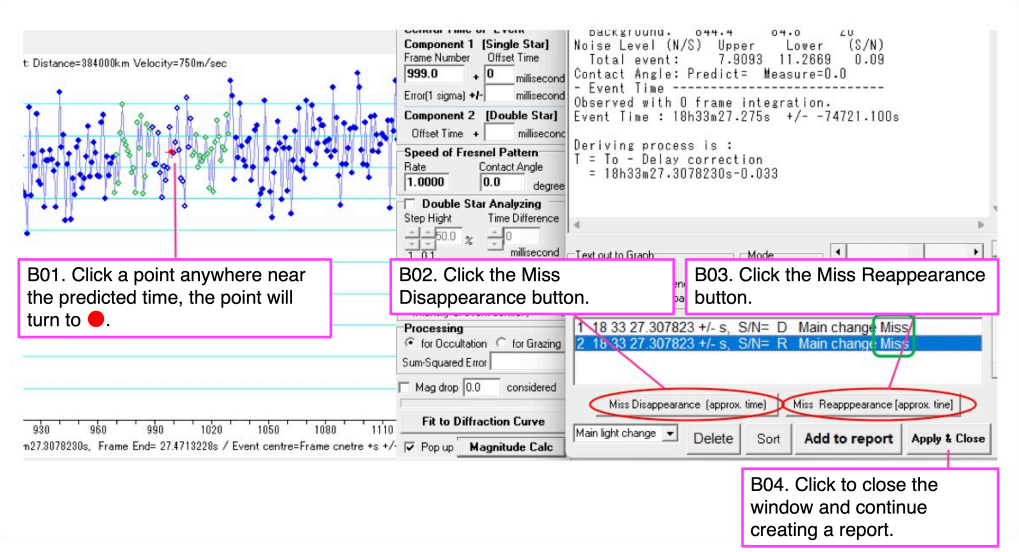

Figure 64: Register with "Miss"

4-8. Special cases ... Double stars

This section describes the case where both the disappearance and the appearance of the light curve have steps. When a step is observed in the middle of the disappearance/appearance process, the one with the larger brightness change can be registered as the "Main light change", and the one with the smaller brightness change can be registered as the "Minor light change" (see Figures 65, 66, 67, 68).

Clicking the "Add to report" button will register the phenomenon caused by the main star (main light change). If you want to register the minor light change, change "Main light change" to "Minor light change" in the combo box. It is important to do this with the appropriate line in the list highlighted in blue. Usually the line is highlighted in blue immediately after "Add to report", but due to some operation it will be black on a white background. In this case, click on the line to make it blue again.

The case described here is the one in which the phenomena occurred in the order "disappearance of bright stars" → "disappearance of faint stars" → "appearance of bright stars" → "appearance of faint stars". If the order

of brightness change of the stars is different, set “Main/Minor” accordingly.

You may face a case of no step on one side of the disappearance/appearance. For example, if no step is seen on the appearance side, you can create two disappearance/appearance combinations by clicking the “Miss Reappearance [approx. time]” button after registering the appearance with operation E04 (see Figure 67), and you are ready to make a “Make Report”.

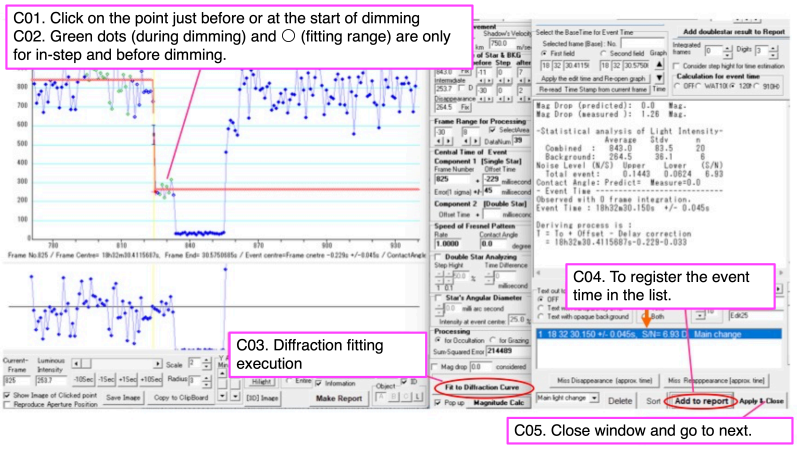

Figure 65: In the case of double stars 1

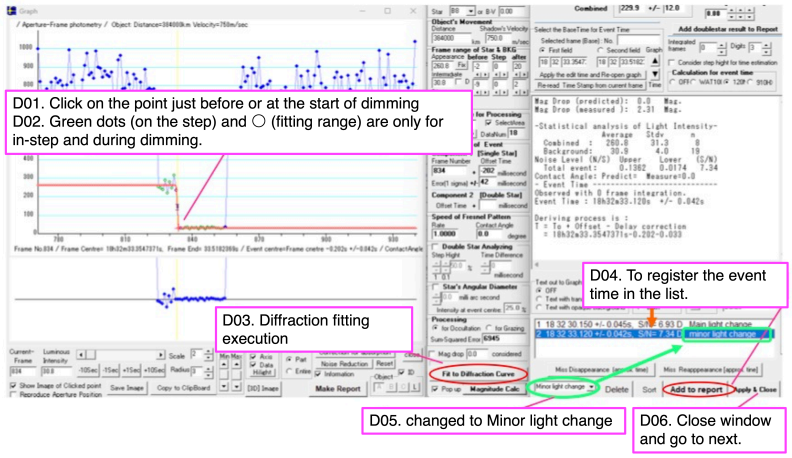

Figure 66: In the case of double stars 2

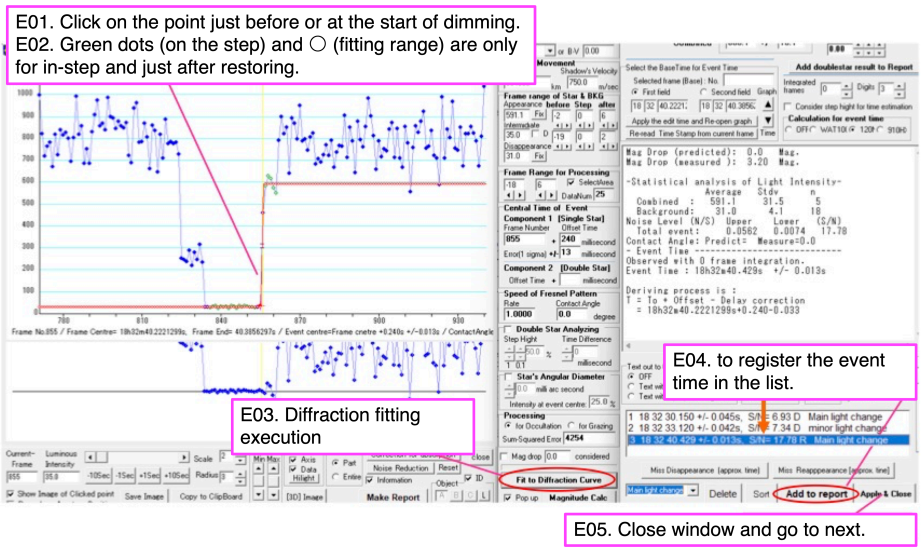

Figure 67: In the case of double stars 3

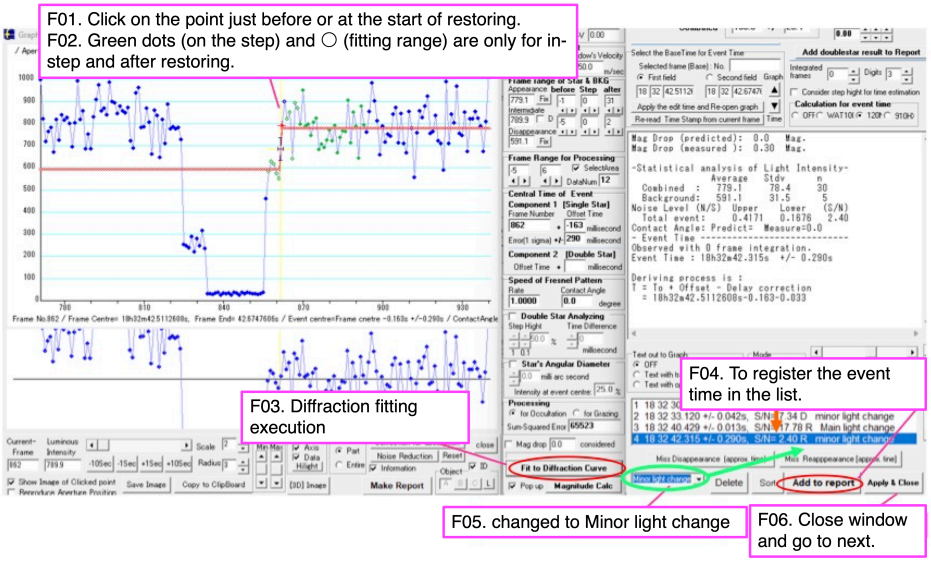

Figure 68: In the case of double stars 4

Step 5. Make report

The previously entered information such as asteroids, stars, and latitude and longitude of the observation site is displayed when the screen is opened. The information about the observation equipment and atmospheric conditions should be entered here. When the camera setup information file is loaded, the necessary information can be entered automatically.

The above information can be copied to the clipboard using the "Copy for Text Report" button and pasted into an e-mail as shown in the lower panel of Figure 69 to be reported as is.

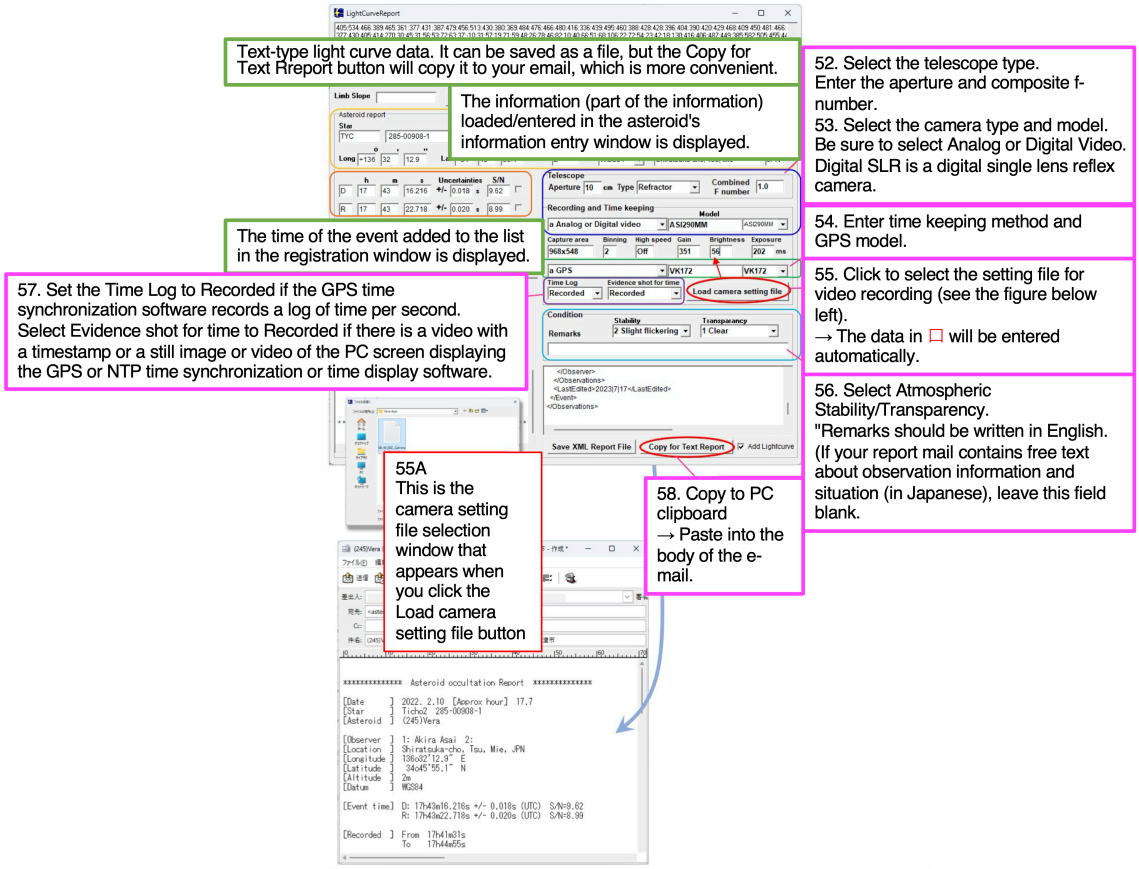

Figure 69: Procedures for making reports

5.2.4 Output Example

```
**************  Asteroid occultation Report  **************

[Date         ]   2022. 2.10   [Approx hour]   17.7
[Star         ]   Ticho2   285-00908-1
[Asteroid    ]   (245)Vera

[Observer    ]   1: Akira Asai    2:
[Location    ]   Shiratsuka-cho, Tsu, Mie, JPN
[Longitude ]   136o32'12.9"    E
[Latitude    ]    34o45'55.1"    N
[Altitude    ]   2m
[Datum        ]   WGS84

[Event time]   D: 17h43m16.216s +/- 0.018s (UTC)    S/N=9.62
                  R: 17h43m22.718s +/- 0.020s (UTC)    S/N=8.99

[Recorded    ]   From    17h41m31s
                  To       17h44m55s

[Mag. drop ]   D: Measured: 2.32 ; Predicted: 2.7
                  R: Measured: 2.39 ; Predicted: 2.7

[Telescope ]   Aperture: 10cm     Type: Refractor     F=1.0
[Camera      ]   Analog or Digital video ,   Model= ASI290MM
[Exposure    ]   Set: 202msec,   Measure: 202msec
[Setting     ]   Area: 968x548   ;   Binning=2
                  Gain: 351   ;   Brightness: 0   ;   High Speed Mode: Off
[Time keep ]   GPS   ;   Model: VK172
[Evidence    ]   GPS Time Log : Recorded   ;   Screen shot: Recorded

[Condition ]   Stability: Slight flickering   Transparency: Clear
[Remarks     ]

[Additional comment]



****************************************************************

<Observations>
  <Event>
    <Date>2022|2|10|17.7</Date>
    <Details>
      <Star>Ticho2|                                                                                                    285-00908-
1|0||0.0000000000|0.000000000|0.00|0.00|0.00|0|0.00000000|0.0000000|25.00|25.00|25.00|0</Star>

<Asteroid>245|Vera|0.00000000|0.00000000|0.0000000|0.0000000|0.0000000|0.0000000|1.00000|0.00000|0.0|1.0|2
0.00</Asteroid>
    </Details>
    <Observations>
      <Observer>
        <ID>1|Akira Asai||0|Shiratsuka-cho, Tsu, Mie|JPN|+136 32 12.9|+34 45 55.1|2| |10|1|a|a</ID>
        <Conditions>2|1|9.30||</Conditions>
        <D>17 43 16.216|D|0.018||| </D>
        <R>17 43 22.718|R|0.020||| </R>
      </Observer>
    </Observations>
    <LastEdited>2023|7|17</LastEdited>
  </Event>
</Observations>

****************************************************************
```

Figure 70: Part of Asteroid occultation Report 1.

Text-based Light curve

Date: 2022-2-10 17:42:45.30: 68.48: 340
Star: 0: 0: 0: 0: 285-00908-1: 0-0
Observer: +136:32:12.9: +34:45:55.1: 2: Akira Asai
Object: Asteroid: 245: Vera
Values:463:464:496:453:403:364:504:384:388:528:407:458:485:443:410:478:444:419:427:433:449:316:426:496:461:39
6:438:528:431:446:448:399:452:404:422:431:479:452:445:381:403:455:403:446:387:387:458:487:374:
534:507:435:416:496:351:486:391:423:393:430:455:432:448:380:395:444:470:393:392:389:457:476:494:488:443:442:4
64:464:415:461:465:452:436:452:391:386:476:468:410:503:422:517:446:396:474:444:446:444:427:
405:534:466:389:465:361:377:431:387:479:456:513:430:380:369:484:476:466:480:416:336:439:495:460:388:428:428:3
96:404:390:420:429:468:409:450:481:466:483:428:462:438:426:498:428:535:389:473:441:440:472:
377:430:405:414:270:30:45:31:56:53:72:63:37:-
10:31:57:19:71:59:48:26:78:46:82:10:40:66:51:68:106:22:72:54:23:42:18:130:416:406:487:449:385:582:505:455:442:50
3:447:436:422:
526:346:419:418:439:418:445:457:448:426:509:366:479:426:436:490:530:460:432:528:496:414:459:396:446:511:413:3
95:435:494:441:430:467:511:488:441:458:399:457:408:442:487:517:516:447:534:458:438:417:386:
414:463:372:439:432:494:459:504:464:414:497:419:392:414:523:433:428:529:465:493:414:458:541:450:421:445:482:5
36:496:450:426:429:445:445:506:436:482:572:431:346:493:454:387:498:479:513:501:480:491:448:
448:411:456:449:488:450:472:445:415:478:504:370:370:400:437:469:511:367:527:449:468:472:326:518:439:491:422:4
63:483:451:478:478:492:419:423:457:435:467:430:397:375

Figure 71: Part of Asteroid occultation Report 2.

6 Observation Reports

The following information is required for the observation report. Here we describe how to obtain the information for 2. The data under 3. will be obtained after the analysis is completed.

1. Name of observer and name in Roman alphabet
2. Name of the observation site, latitude and longitude of the observation site, altitude and geodetic system
3. Time of start and end of observation
4. Did you observe light attenuation? Even if no attenuation was observed, this is still important data.
5. Time when the dimming occurred: the time of the beginning and the time of the end of the dimming.
6. Observation equipments
7. Time keeping method

6.1 Observation site

The information of observation site is an important piece of data, with the same weight as the time of the event. The observation site should be reported in a way that ensures accuracy.

6.1.1 Measure the longitude and latitude of the observation site

The coordinate system for latitude and longitude used to be unique to each country, but nowadays the "World Geodetic System" is commonly used throughout the world, and latitude and longitude should be reported according to the "World Geodetic System" unless there are obstacles. If observations are made in special areas where " World Geodetic System" coordinates are not available, the type of geodetic system should be specified. For example, the United States uses the "WGS84 coordinate system" and Japan uses the "JDS2000 coordinate system", but both coordinate systems can be considered practically the same for general use, including occultation observations. When specifying an observer's latitude and longitude based on these world geodetic systems, the geodetic system should be specified as "WGS84".

Within Japan, the Geospatial Information Authority of Japan's Geospatial Information Authority of Japan (GSI) map site (https://maps.gsi.go.jp) can be used. Longitude and latitude measurements by GPS are accurate enough for occultation observations with a typical GPS receiver and can be used in any region of the world. when surveying with GPS, it is advisable to average several measurements after a period of at least 10 minutes after power-on to achieve receiver stability.

Latitude and longitude should be reported as "DD degrees MM minutes SS.S seconds" or "DD.DDDDD degrees". The former should be reported to an accuracy of 0.1 seconds and the latter to an accuracy of five decimal places. At the equator, 0.1 second corresponds to a distance of about 3 meters on the Earth's surface, and 0.00001 degree corresponds to about 1 meter.

[HY1] Although the required latitude and longitude accuracy varies with each event and time resolution, a positional accuracy of 0.1 second (or 0.00001 degree) is sufficient for occultation observations.

6.1.2 Observer's elevation

The elevation of the observation site is also important, as are the latitude and longitude. The elevation is the so-called "above mean sea level", which

in geodetic terms is the "height above the geoid plane". This is a different standard from the common GPS altitude (altitude above the plane of the Earth's rotating ellipsoid) and requires caution. The GPS altitude is currently inaccurate and inadequate, so it is not recommended. The reason for the low accuracy is that GPS satellite information below the horizon is not available.

As with longitude and latitude, it is desirable to measure altitude using a method that guarantees accuracy. In Japan, the Geospatial Information Authority of Japan (GSI) map website can be used for this purpose. If reliable elevation data is not available, such as in foreign countries, elevations can be obtained from the following site, "mapcoordinates.net" (https://www.mapcoordinates.net/en) .

This type of global elevation service on the Internet often uses the "Google Elevation Service" provided by Google Earth (GE), which does not disclose its accuracy, but a survey in the U.S. reported an error of (1σ) 22 meters. The reported elevation is the height of the observation site plus the height of the building and the telescope position, reported to the order of 1 meter. The required elevation accuracy varies with the altitude of the target star and the time resolution of each event, but an accuracy of 10 meters is usually sufficient for occultation observations (the time error is usually much larger than the elevation error, although it varies with each event).

6.2 Report

IOTA (The International Occultation Timing Association) collects and makes available internationally the results of observations of stellar occultations by asteroids. It is recommended that observations be reported to IOTA regardless of whether positive/negative detentions. IOTA has a coordinator in each region, and the following information should be reported to the coordinator in the region where the observation was made.

1. Name of observer and name in Roman alphabet
2. Name of the observation site, latitude and longitude of the observation site, altitude and geodetic system
3. Time of start and end of observation
4. Did you observe light attenuation? Even if no attenuation was observed, this is still important data.

5. Time when the dimming occurred: the time of the beginning and the time of the end of the dimming.

6. Observation equipments

7. Time keeping method

Observations reported to IOTA are registered as historical observations in the OCCULT4 software and, depending on the results, reported to IAU Asteroid Astrometry and JDSO for development of astronomy. If you are an observer who can use OCCULT4, you are also encouraged to report your observations using the OCCULT4 report form (OBS.xml).

Table 1: Coordinators and contact information for each region as of 2022

North America	Jhon Moore	reports@asteroidoccultation.com
South America	Breno Loureiro Giacchini	bgiacchini@yahoo.com.br
Europe	Eric Frappa	frappa@laposte.net
Asia	Tsutomu Hayamizu	asteroid-report@iota-ea.org
Oceania	Steve Kerr	Steve.Kerr@outlook.com.au
	Dave Gault	davegault@bigpond.com

7 Appendix a

7.1 Observations of stellar occultation by asteroid (3200) Phaethon; DESTINY$^+$ flyby targets

7.1.1 The importance of Phaethon observations

Asteroid (3200) Phaethon is an Apollo-type near-Earth asteroid. The orbital period is 1.43 years, orbital radius: 1.27 au, eccentricity: 0.89, inclination: 22°.3, and it orbits in an elongated orbit inclined from the ecliptic plane. The perihelion distance is 0.14 au, which is inside Mercury's orbit and brings Phaethon's surface temperature to about 1000 K. The aphelion distance is 2.40 au, which is the middle of the main belt (asteroid belt), where Phaethon's surface temperature is estimated to drop to about 200 K. Phaethon's surface temperature there is estimated to drop to about 200 K. In other words, Phaethon experiences a temperature change of about 800 K every 1.43 years [33, 22, 23, 36]. We suspect that such extreme and cyclical temperature changes cause Phaethon's surface to be covered with thermally altered or disintegrated material. Such Phaethon-like objects are rare even among the various forms of near-Earth asteroids.

Phaethon is also considered the parent body of the Geminid meteor shower observed every December [16, 41, 21]. Phaethon is classified as a B- or F-type asteroid [35, 29, 30, 6, 32, 24, 38]. This type of asteroid belongs to a C-complex, like (162173) Ryugu, which is the target of the HAYABUSA mission, which contains organic matter, hydrous minerals, etc. The fact that Phaethon is the parent body of the Geminid meteor shower indicates that Phaethon is one of the sources from which dust containing carbon and organic matter, the precursors of life, reaches the Earth. The study of the asteroid Phaethon will lead to an understanding of the mechanism of dust release from the asteroid and the composition of the organic dust delivered to the Earth.

As seen from the above, Phaethon is an object worthy of detailed study by a spacecraft. Therefore, the Institute of Space and Astronautical Science (ISAS) of the Japan Aerospace Exploration Agency (JAXA), in collaboration with the Planetary Exploration Research Centre of the Chiba Institute of Technology (Chiba Institute of Technology), is planning the "DESTINY$^+$" (Demonstration and Experiment of Space Technology for INterplanetary voYage with Phaethon fLyby and dUst Science) project[3, 4, 5].

The goal of the DESTINY$^+$ mission is to conduct scientific investigations of the asteroid Phaethon and its dust using advanced ion engine navigation and multi-object flyby exploration technologies. The spacecraft is scheduled

for launch in 2025. The DESTINY$^+$ spacecraft will be launched by an Epsilon rocket into a long elliptical orbit around the Earth, gradually increasing its orbital altitude over about two years and leaving the Earth in a 'lunar swing-by'. It will then gradually change orbit over two years to reach the Phaethon flyby point in 2030. During the four years between launch and flyby, the spacecraft will observe interstellar and interplanetary dust with the DESTINY$^+$ Dust Analyser (DDA) [26, 31] on board. During the flyby, the spacecraft will come till 500 km from Phaethon and observe the asteroid with two cameras, the Telescope Camera for Phaethon (TCAP) and the Multiband Camera for Phaethon (MCAP)[20, 19]. In addition, DDA will directly analyze the dust around Phaethon.

The DESTINY$^+$ spacecraft will orbit roughly on the ecliptic plane waiting for Phaethon to approach and will encounter Phaethon at 36 km/s during the flyby. At such a high speed, the spacecraft will only be close to Phaethon for a very short time and will not have enough time to study the asteroid in detail from the spacecraft before the flyby. It is therefore essential for the success of the mission that the characteristics of the object, such as shape, albedo and rotation period, are studied in as much detail as possible before the flyby, and that making an observing strategy for the flyby, such as the exposure time, the angle of view of the two cameras, the timing of the flyby, etc., is devised. Ground-based observations are therefore necessary.

In December 2017, Phaethon approached Earth to about 0.07 au and brightened to about 11th magnitude. Taking advantage of this opportunity, the DESTINY$^+$ Science team called for a global observation campaign. Many researchers observed Phaethon. As a result, together with the results of previous studies, the rotation period of Phaethon and the direction of its rotation axis [37, 27, 2, 17, 18, 25] and the spectral type [**?**, 29, 30, 6, 32, 24, 38] were determined with high accuracy. Radar observations carried out at the Arecibo Observatory revealed that the effective diameter of Phaethon is about 6 km and that Phaethon has a spin-top shape, which is similar to the shape of (162173) Ryugu [39] and (101955) Benne [12], which were explored by Hayabusa2 [40] and OSIRIS-Rex [28], respectively.

Despite these intensive observations, the absolute magnitude, which is essential for estimating Phaethon's size, could not be accurately determined. The absolute magnitude of an asteroid is defined as the V-magnitude (visible light) at a solar phase angle of 0°, but due to Phaethon's peculiar orbit and the orbital configuration between Phaethon, the Sun and the Earth, there is no chance to observe Phaethon at a solar phase angle of 0°. Therefore, there was a large error in the estimation of Phaethon's size and albedo. Since the

albedo, which is determined based on the object size, is an important value in determining the camera exposure, the DESTINY$^+$ Science team had to estimate Phaethon's size using a method other than absolute magnitude to derive a more accurate albedo.

Occultation observation is a method of determining the size of an asteroid by measuring the size of the shadow cast on the ground by the asteroid as it occults background stars. Light coming from a distant star can be regarded as parallel light, so it is "the size of the shadow cast by the asteroid on the Earth" $\approx$ "the size of Phaethon". Before the method of calculating the diameter of an asteroid from the albedo estimated by a combination of the absolute magnitude in visible light and a thermal model obtained from infrared observations became common, the diameter of asteroids was measured by occultation observations. Determining the diameter of an asteroid from visible and infrared observations requires a thermal model, a "rough assumption", which introduces systematic errors. Occultation observations, on the other hand, directly measure the size of the asteroid's shadow. Only the accuracy of the measurement of the occultation timing (dim and recover) only introduces error into the diameter estimate. Therefore, if we can observe the occultation event with high time resolution and precise timing, we can determine the asteroid diameter very accurately. Now we have GPS and a CMOS camera. If you use this instruments correctly, the measurment of the asteroid size by stellar occultation provides us the most accurate size and shape of asteroids than any other method currently available.

The DESTINY$^+$ science team therefore decided to perform occultation observations to obtain a more accurate estimate of Phaethon's diameter. However, occultation observations of small objects like Phaethon were almost unprecedented: the smallest asteroid successfully observed its stellar occultation before 2019 was (11072) Hiraoka with a diameter of 7 km, but only one positive detection was reported (http://spiff.rit.edu/richmond/occult/hiraoka_may2006/Observation_of_a_Very_Small_Asteroid.doc.). In recent years, however, this situation has changed significantly. The Gaia Space Telescope of the European Space Agency (ESA) catalogus the positions, distances and motions of stars with unprecedented accuracy[15, 13, 14], All-Sky Surveys (Pan-STARRS [34] and Catalina Sky Survey [8]) have improved the accuracy of orbit determination for small asteroids.

As the accuracy of star positions improves and the orbital information of many asteroids is listed, more and more occultation events can be accurately predicted. In this context, Isao Sato discovered that stellar occultation event by Phaethon occurs in the western USA on July 29, 2019. Hirotomo Noda

noticed that Phaethon's stellar occultation can be observable in Japan on August 21, 2019 and October 15, 2019. Therefore, the DESTINY$^+$ Science team asked experienced occultation observers to observe these stellar occultations by Phaethon.

7.1.2 Observations of stellar occultation by Phaethon

The first successful observation of Phaethon's stellar occultation was in the western USA on July 29, 2019. The observation was organized on a very large scale, with a large number of volunteers stationed at 66 lines drawn 680 m apart from the center of the predicted occultation zone in the San Joaquin Valley. Simultaneous observations were also made at 19 sites in Las Vegas. As a result of these observations, Phaethon's shadow was found to be slightly larger than a circle 5 km in diameter, as shown in Figure72. Other events were observed in California, USA on September 29, 2019 (see Figure73), in Virginia, USA, on October 12, 2019 (see Figure74), in Algeria on October 15 and 25, 2019 (see Figure76, 77), and in Mississippi, USA, October 5, 2020 (see Fig. **??**). However these observations did not provide enough data to improve on the results obtained on July 29, 2019, due to the small number of chords [9, 10, 11].

In Japan, a team of amateur astronomers and planetary scientists observed Phaethon's stellar occultation on August 21, 2019 (Hokkaido, Japan) and October 15, 2019 (Tohoku region), but the weather was poor and only two positive detections were obtained on October 15, 2019 (Figure 75,[9], https://aas.org/sites/default/files/2020-10/David_Dunham_DPS52.pdf, http://iota.jhuapl.edu/DunhamAstSciConf2019.ppt).

As mentioned above, the DESTINY$^+$ Science team did not achieve its goal of "determining the size of Phaethon with an error of less than 5 %" during the intensive Phaethon occultation observation campaign conducted from 2019 to 2020. Therefore, the DESTINY$^+$ science team conducted another observation campaign in Japan for the occultation event occures on October 3, 2021 (UTC). This was an opportunity to observe the shape of Phaethon from a different angle than the stellar occultation by Phaethon that occurred in the western USA on July 29, 2019. At the observations on October 3, 2021, the team got positive detections at 18 different locations and successfully obtained the shape of Phaethon during the occultation, which can be fitted as an ellipse with a major axis of 6.12±0.07 km and a minor axis of 4.14±0.07km (see Figure 78). Furthermore, the DESTINY$^+$ science team again convened an observation team of amateur astronomers and planetary scientists in Hokkaido on October 21, 2022, and succeeded in

Table 2: Observations of stellar occultation by (3200) Phaethon to date

Date (UTC)	Star	Mag (mag)	Duration (Max) (sec)	Number of observers	Number of positive detection	Country /region
2019.07.29	HIP 24973	7.3	0.47	52	6	USA
2019.09.29	UCAC4 721-029705	12.0	0.27	8	4	USA
2019.10.12	TYC 3293-01959-1	11.3	0.23	2	2	USA
2019.10.15	TYC 3292-00570-1	11.5	0.22	3	2	Tohoku
2019.10.15	UCAC4 707-014626	11.1	0.22	5	3	Europe
2019.10.25	TYC 3268-00276-1	11.3	0.22	4	3	Italy, Algeria
2020.10.05	TYC 1931-01029-1	11.2	0.16	6	1	USA
2021.10.03	UCAC4 646-021974	12.0	0.64	25	18	West Japan
2021.12.07	UCAC4 617-00897	9.9	0.23	2	2	Taiwan
2022.10.21	TYC 2844-0735-1	10.8	0.22	39	9	Hokkaido
2022.10.22	UCAC4 674-012720	12.8	0.30	1	1	Hiroshima

measuring a different cross-sectional shape of Phaethon than that obtained on October 3, 2021 (see Figure82).

We summarized the results of Phaethon's occultation observations to date in Table 2. Figures 72 to 82 are the skyplane maps of the respective observations. As can be seen from these figures, that the observations made by Marc Buie and his colleagues on July 29, 2019, responed to the the DESTINY$^+$ science team's request, involved how large number of observers. This initial success led to improvements in Phaethon's orbit and increased the accuracy of later occultation predictions. Subsequent occultation events for two years could not be observed with greater accuracy than that of July 29, 2019 due to unfavorable weather conditions, but the observations made in Japan on October 3, 2021 and October 21, 2022 were very successful. The results of these two observations were compared with the 3D shape model of Phaethon created by Sean Marshall, a member of the DESTINY$^+$ science team (Figure83, Figure 84) and used as data to improve the model.

figures/2019.10.15b.eps

As described above, the Phaethon's occultation observations were very successful. In particular, the great success of the joint observation of professional/amateur observers on October 3, 2021, is described in detail in [42]. This observation proved that it is possible to accurately observe occultations with durations of less than 1 second by asteroids with diameters of 5 to 6 km, in addition, it also proved, if multiple chord observations are success-

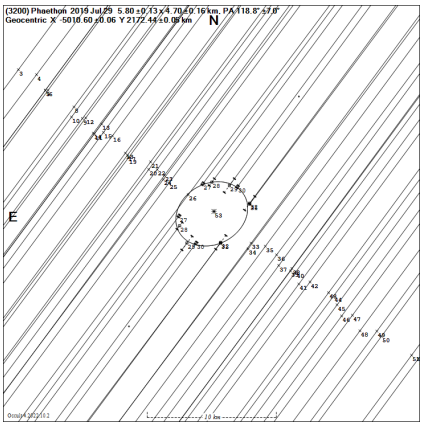

Figure 72: 2019.07.29

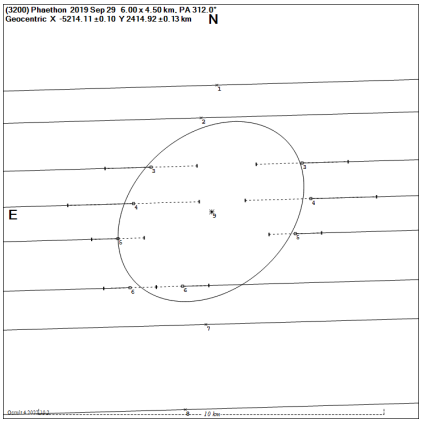

Figure 73: 2019.09.29

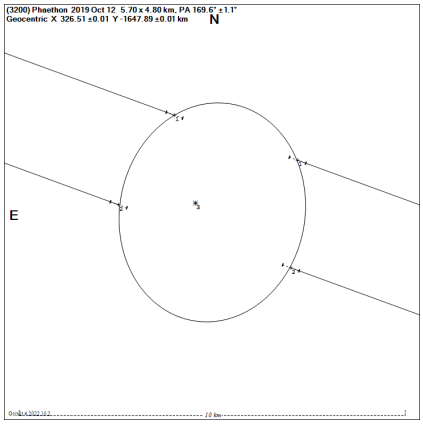

Figure 74: 2019.10.12

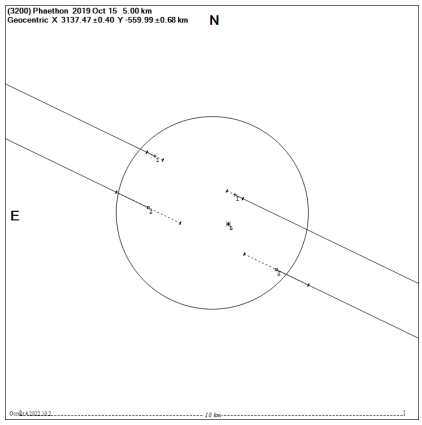

Figure 75: 2019.10.15 in Tohoku, Japan

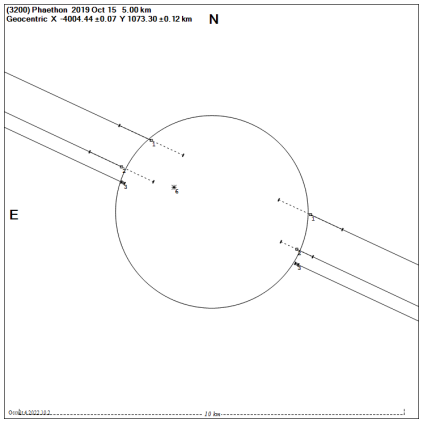

Figure 76: 2019.10.15 in Europe

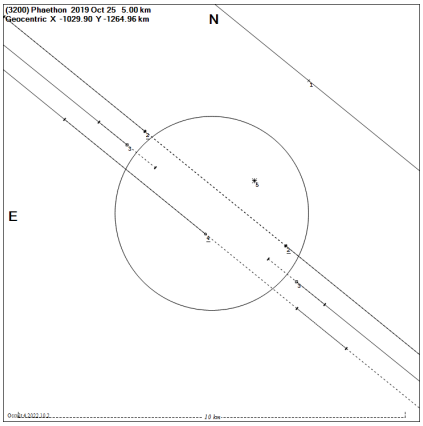

Figure 77: 2019.10.25

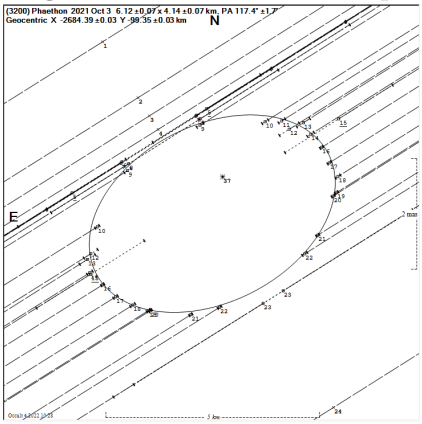

Figure 78: 2021.10.03

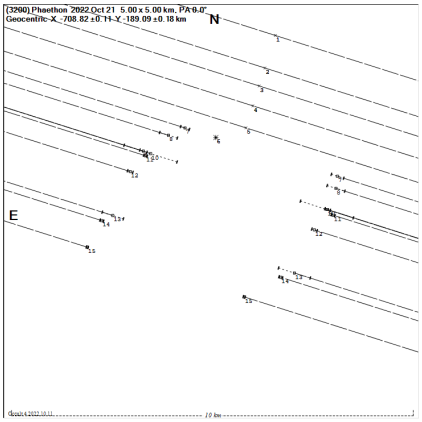

Figure 79: 2022.10.21

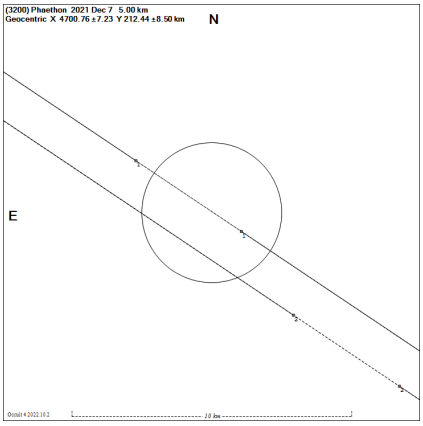

Figure 80: 2021.12.07

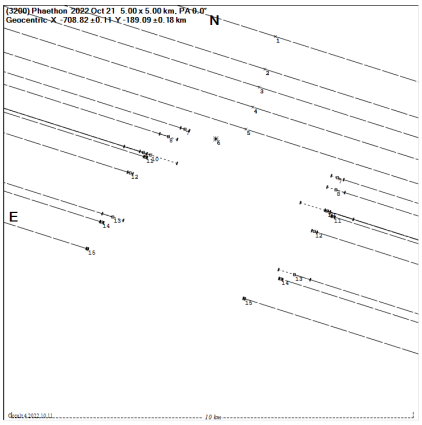

Figure 81: 2022.10.21

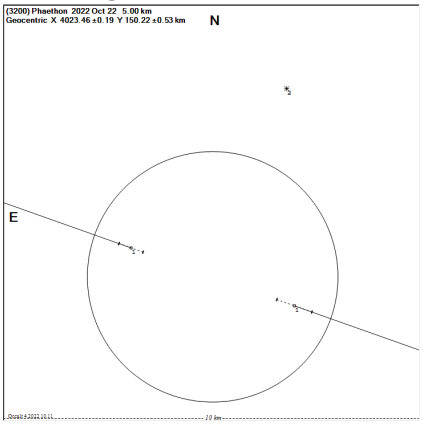

Figure 82: 2022.10.22

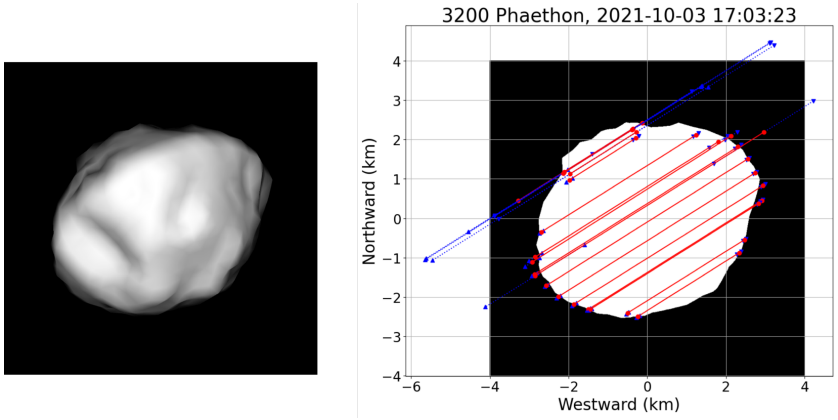

Figure 83: Left: 3D figure of Phaethon generated from the 3D shape model created by Sean Marshall showing the shape and orientation of Phaethon as seen from the Earth at the time of the occultation event on October 3, 2021 (UT). Right: Multiple chords derived from observations of stellar occultation by Pharthon superimposed on the cross section generated by the 3D shape model. The length of each red line corresponds to the size of Phaethon's shadow measured by each occultation observer. The blue line indicates the measurement error.

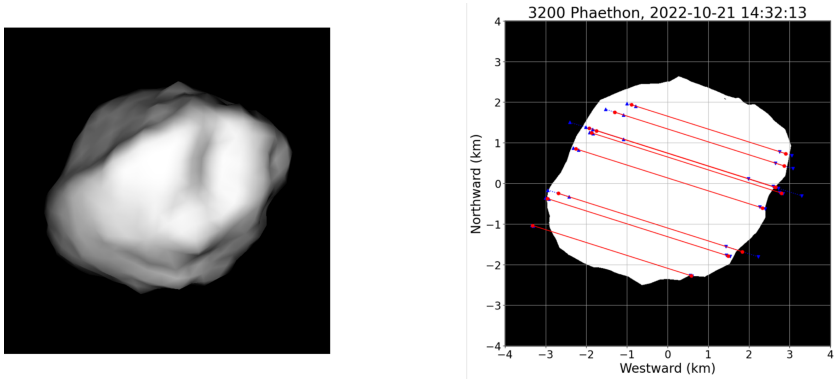

Figure 84: Left: 3D figure of Phaethon generated from the 3D shape model created by Sean Marshall showing the shape and orientation of Phaethon as seen from the Earth at the time of the occultation event on October 21, 2022 (UT). Right: Multiple chords derived from observations of stellar occultation by Pharthon superimposed on the cross section generated by the 3D shape model. The length of each red line corresponds to the size of Phaethon's shadow measured by each occultation observer. The blue line indicates the measurement error.

fully performed, the shape of such small asteroid can be determined. After these successful experiences, Japanese observers came up to the challenge of observing occultation events by smaller asteroids. For example, a team of Japanese amateur observers made successful observation four times on the occultation observations by the primary of a double asteroid: Didymos (780 m in diameter) for NASA's DART mission (URL https://dart.jhuapl.edu).

In Japan, occultation observations played a role in supporting planetary exploration missions for the first time in the DESTINY$^+$ mission. While overseas, occultation observations play a very important role in NASA's New Horizons mission, which made flybys of Pluto system and (486958) Arrokoth [7], and NASA's Lucy mission, which will flyby Jupiter Trojan asteroids (http://lucy.swri.edu/occultations.html).

Occultations by asteroids smaller than a few kilometers in diameter were not even publicly predicted before, but since "Occult", an occultation prediction and observation software, was released and made freely available to everyone, it has become easier for anyone to plan occultation observations. The development of CMOS cameras, GPS modules, and other technologies has made it possible to measure the timing of the occultation more accurately and to obtain precise information about the observer's location. The accuracy of the positions of occulted stars and the orbits of asteroids have also improved dramatically. In the future, people will challenge the occultation observations with smaller asteroids and fainter stars. We are sure that the occultation observation will be more precise and accurate and then become as a very useful partner of planetary exploration missions.

References

[1] Detection and Characterization of Near Earth Asteroids Using Stellar Occultation, volume 150. 2013.

[2] M. Ansdell, K. J. Meech, O. Hainaut, M. W. Buie, H. Kaluna, J. Bauer, and L. Dundon. REFINED ROTATIONAL PERIOD, POLE SOLUTION, AND SHAPE MODEL FOR (3200) PHAETHON. The Astrophysical Journal, 793(1):50, sep 2014.

[3] T. Arai. Overview and Science of DESTINY+. In European Planetary Science Congress, pages EPSC2021–877, Sept. 2021.

[4] T. Arai, T. Yamamoto, N. Ozaki, H. Toyota, K. Nishiyama, and T. Takashima. Current status and science of DESTINY+. In 43rd COSPAR Scientific Assembly. Held 28 January - 4 February, volume 43, page 276, Jan. 2021.

[5] T. Arai, F. Yoshida, M. Kobayashi, K. Ishibashi, H. Kimura, T. Hirai, P. Hong, K. Wada, H. Senshu, M. Yamada, R. Srama, H. Krüger, M. Ishiguro, H. Yabuta, T. Nakamura, S. Kobayashi, J. Watanabe, T. Ito, T. Ootsubo, K. Ohtsuka, S. Tachibana, T. Mikouchi, T. Morota, M. Komatsu, K. Nakamura-Messenger, S. Sasaki, T. Hiroi, S. Abe, S. Urakawa, N. Hirata, H. Demura, G. Komatsu, T. Noguchi, T. Sekiguchi, D. Kinoshita, H. Kaneda, S. Kameda, S. Matsuura, M. Ito, A. Yamaguchi, T. Yanagisawa, H. Kurosaki, T. Okamoto, A. Nakato, H. Yano, M. Yoshikawa, D. W. Dunham, M. W. Buie, P. A. Taylor, S. Marshall, N. Ozaki, T. Yamamoto, H. Imamura, H. Toyota, K. Nishiyama, and T. Takashima. Current Status of DESTINY+ and Updated Understanding of Its Target Asteroid (3200) Phaethon. In 52nd Lunar and Planetary Science Conference, Lunar and Planetary Science Conference, page 1896, Mar. 2021.

[6] G. Borisov, M. Devogèle, A. Cellino, S. Bagnulo, A. Christou, P. Bendjoya, J.-P. Rivet, L. Abe, D. Vernet, Z. Donchev, Y. Krugly, I. Belskaya, T. Bonev, D. Steeghs, D. Galloway, V. Dhillon, P. O'Brien, D. Pollacco, S. Poshyachinda, G. Ramsay, E. Thrane, K. Ackley, E. Rol, K. Ulaczyk, R. Cutter, and M. Dyer. Rotational variation of the linear polarization of the asteroid (3200) Phaethon as evidence for inhomogeneity in its surface properties ★. Monthly Notices of the Royal Astronomical Society: Letters, 480(1):L131–L135, 08 2018.

[7] M. W. Buie, S. B. Porter, A. J. Verbiscer, R. Leiva, B. A. Keeney, C. C. C. Tsang, D. Baratoux, M. F. Skrutskie, F. Colas, J. Desmars, S. A. Stern, and N. H. C. Team. Pre-encounter update on (486958) 2014mu69 and occultation results from 2017 and 2018. 2018.

[8] A. J. Drake, S. G. Djorgovski, A. Mahabal, E. Beshore, S. Larson, M. J. Graham, R. Williams, E. Christensen, M. Catelan, A. Boattini, A. Gibbs, R. Hill, and R. Kowalski. FIRST RESULTS FROM THE CATALINA REAL-TIME TRANSIENT SURVEY. The Astrophysical Journal, 696(1):870–884, apr 2009.

[9] D. Dunham, J. Dunham, M. Buie, S. Preston, D. Herald, D. Farnocchia, J. Giorgini, T. Arai, D. Baba Aissa, and Z. Grigahcene. First Occultation Observations by a Small NEO, (3200) Phaethon. In AAS/Division for Planetary Sciences Meeting Abstracts, volume 52 of AAS/Division for Planetary Sciences Meeting Abstracts, page 412.01, Oct. 2020.

[10] D. Dunham, J. Dunham, M. Buie, S. Preston, D. Herald, D. Farnocchia, J. Giorgini, T. Arai, I. Sato, R. Nolthenius, J. Irwin, S. Degenhardt, S. Marshall, J. Moore, S. Whitehurst, R. Venable, M. Skrutskie, F. Marchis, Q. Ye, P. Tanga, D. B. Aissa, and Z. Grigahcene. Accurate NEO Orbits from Occultation Observations. In 7th IAA Planetary Defense Conference, page 37, Apr. 2021.

[11] D. W. Dunham, J. B. Dunham, M. Buie, S. Preston, D. Herald, and D. Farnocchia. (3200) Phaethon, First Successful Occultation Observations of a Small Near-Earth Object. In Asteroid Science in the Age of Hayabusa2 and OSIRIS-REx, volume 2189 of LPI Contributions, page 2062, Nov. 2019.

[12] H. L. Enos and D. S. Lauretta. A rendezvous with asteroid Bennu. Nature Astronomy, 3:363–363, Apr. 2019.

[13] Gaia Collaboration, A. G. A. Brown, A. Vallenari, T. Prusti, J. H. J. de Bruijne, C. Babusiaux, C. A. L. Bailer-Jones, M. Biermann, D. W. Evans, L. Eyer, F. Jansen, C. Jordi, S. A. Klioner, U. Lammers, L. Lindegren, X. Luri, F. Mignard, C. Panem, D. Pourbaix, S. Randich, P. Sartoretti, H. I. Siddiqui, C. Soubiran, F. van Leeuwen, N. A. Walton, F. Arenou, U. Bastian, M. Cropper, R. Drimmel, D. Katz, M. G. Lattanzi, J. Bakker, C. Cacciari, J. Castañeda, L. Chaoul, N. Cheek, F. De Angeli, C. Fabricius, R. Guerra, B. Holl, E. Masana, R. Messineo, N. Mowlavi, K. Nienartowicz, P. Panuzzo, J. Portell,

M. Riello, G. M. Seabroke, P. Tanga, F. Thévenin, G. Gracia-Abril, G. Comoretto, M. Garcia-Reinaldos, D. Teyssier, M. Altmann, R. Andrae, M. Audard, I. Bellas-Velidis, K. Benson, J. Berthier, R. Blomme, P. Burgess, G. Busso, B. Carry, A. Cellino, G. Clementini, M. Clotet, O. Creevey, M. Davidson, J. De Ridder, L. Delchambre, A. Dell'Oro, C. Ducourant, J. Fernández-Hernández, M. Fouesneau, Y. Frémat, L. Galluccio, M. García-Torres, J. González-Núñez, J. J. González-Vidal, E. Gosset, L. P. Guy, J. L. Halbwachs, N. C. Hambly, D. L. Harrison, J. Hernández, D. Hestroffer, S. T. Hodgkin, A. Hutton, G. Jasniewicz, A. Jean-Antoine-Piccolo, S. Jordan, A. J. Korn, A. Krone-Martins, A. C. Lanzafame, T. Lebzelter, W. Löffler, M. Manteiga, P. M. Marrese, J. M. Martín-Fleitas, A. Moitinho, A. Mora, K. Muinonen, J. Osinde, E. Pancino, T. Pauwels, J. M. Petit, A. Recio-Blanco, P. J. Richards, L. Rimoldini, A. C. Robin, L. M. Sarro, C. Siopis, M. Smith, A. Sozzetti, M. Süveges, J. Torra, W. van Reeven, U. Abbas, A. Abreu Aramburu, S. Accart, C. Aerts, G. Altavilla, M. A. Álvarez, R. Alvarez, J. Alves, R. I. Anderson, A. H. Andrei, E. Anglada Varela, E. Antiche, T. Antoja, B. Arcay, T. L. Astraatmadja, N. Bach, S. G. Baker, L. Balaguer-Núñez, P. Balm, C. Barache, C. Barata, D. Barbato, F. Barblan, P. S. Barklem, D. Barrado, M. Barros, M. A. Barstow, S. Bartholomé Muñoz, J. L. Bassilana, U. Becciani, M. Bellazzini, A. Berihuete, S. Bertone, L. Bianchi, O. Bienaymé, S. Blanco-Cuaresma, T. Boch, C. Boeche, A. Bombrun, R. Borrachero, D. Bossini, S. Bouquillon, G. Bourda, A. Bragaglia, L. Bramante, M. A. Breddels, A. Bressan, N. Brouillet, T. Brüsemeister, E. Brugaletta, B. Bucciarelli, A. Burlacu, D. Busonero, A. G. Butkevich, R. Buzzi, E. Caffau, R. Cancelliere, G. Cannizzaro, T. Cantat-Gaudin, R. Carballo, T. Carlucci, J. M. Carrasco, L. Casamiquela, M. Castellani, A. Castro-Ginard, P. Charlot, L. Chemin, A. Chiavassa, G. Cocozza, G. Costigan, S. Cowell, F. Crifo, M. Crosta, C. Crowley, J. Cuypers, C. Dafonte, Y. Damerdji, A. Dapergolas, P. David, M. David, P. de Laverny, F. De Luise, R. De March, D. de Martino, R. de Souza, A. de Torres, J. Debosscher, E. del Pozo, M. Delbo, A. Delgado, H. E. Delgado, P. Di Matteo, S. Diakite, C. Diener, E. Distefano, C. Dolding, P. Drazinos, J. Durán, B. Edvardsson, H. Enke, K. Eriksson, P. Esquej, G. Eynard Bontemps, C. Fabre, M. Fabrizio, S. Faigler, A. J. Falcão, M. Farràs Casas, L. Federici, G. Fedorets, P. Fernique, F. Figueras, F. Filippi, K. Findeisen, A. Fonti, E. Fraile, M. Fraser, B. Frézouls, M. Gai, S. Galleti, D. Garabato, F. García-Sedano, A. Garofalo, N. Garralda, A. Gavel, P. Gavras, J. Gerssen, R. Geyer, P. Gia-

cobbe, G. Gilmore, S. Girona, G. Giuffrida, F. Glass, M. Gomes, M. Granvik, A. Gueguen, A. Guerrier, J. Guiraud, R. Gutiérrez-Sánchez, R. Haigron, D. Hatzidimitriou, M. Hauser, M. Haywood, U. Heiter, A. Helmi, J. Heu, T. Hilger, D. Hobbs, W. Hofmann, G. Holland, H. E. Huckle, A. Hypki, V. Icardi, K. Janßen, G. Jevardat de Fombelle, P. G. Jonker, Á. L. Juhász, F. Julbe, A. Karampelas, A. Kewley, J. Klar, A. Kochoska, R. Kohley, K. Kolenberg, M. Kontizas, E. Kontizas, S. E. Koposov, G. Kordopatis, Z. Kostrzewa-Rutkowska, P. Koubsky, S. Lambert, A. F. Lanza, Y. Lasne, J. B. Lavigne, Y. Le Fustec, C. Le Poncin-Lafitte, Y. Lebreton, S. Leccia, N. Leclerc, I. Lecoeur-Taibi, H. Lenhardt, F. Leroux, S. Liao, E. Licata, H. E. P. Lindstrøm, T. A. Lister, E. Livanou, A. Lobel, M. López, S. Managau, R. G. Mann, G. Mantelet, O. Marchal, J. M. Marchant, M. Marconi, S. Marinoni, G. Marschalkó, D. J. Marshall, M. Martino, G. Marton, N. Mary, D. Massari, G. Matijevič, T. Mazeh, P. J. McMillan, S. Messina, D. Michalik, N. R. Millar, D. Molina, R. Molinaro, L. Molnár, P. Montegriffo, R. Mor, R. Morbidelli, T. Morel, D. Morris, A. F. Mulone, T. Muraveva, I. Musella, G. Nelemans, L. Nicastro, L. Noval, W. O'Mullane, C. Ordénovic, D. Ordóñez-Blanco, P. Osborne, C. Pagani, I. Pagano, F. Pailler, H. Palacin, L. Palaversa, A. Panahi, M. Pawlak, A. M. Piersimoni, F. X. Pineau, E. Plachy, G. Plum, E. Poggio, E. Poujoulet, A. Prša, L. Pulone, E. Racero, S. Ragaini, N. Rambaux, M. Ramos-Lerate, S. Regibo, C. Reylé, F. Riclet, V. Ripepi, A. Riva, A. Rivard, G. Rixon, T. Roegiers, M. Roelens, M. Romero-Gómez, N. Rowell, F. Royer, L. Ruiz-Dern, G. Sadowski, T. Sagristà Sellés, J. Sahlmann, J. Salgado, E. Salguero, N. Sanna, T. Santana-Ros, M. Sarasso, H. Savietto, M. Schultheis, E. Sciacca, M. Segol, J. C. Segovia, D. Ségransan, I. C. Shih, L. Siltala, A. F. Silva, R. L. Smart, K. W. Smith, E. Solano, F. Solitro, R. Sordo, S. Soria Nieto, J. Souchay, A. Spagna, F. Spoto, U. Stampa, I. A. Steele, H. Steidelmüller, C. A. Stephenson, H. Stoev, F. F. Suess, J. Surdej, L. Szabados, E. Szegedi-Elek, D. Tapiador, F. Taris, G. Tauran, M. B. Taylor, R. Teixeira, D. Terrett, P. Teyssandier, W. Thuillot, A. Titarenko, F. Torra Clotet, C. Turon, A. Ulla, E. Utrilla, S. Uzzi, M. Vaillant, G. Valentini, V. Valette, A. van Elteren, E. Van Hemelryck, M. van Leeuwen, M. Vaschetto, A. Vecchiato, J. Veljanoski, Y. Viala, D. Vicente, S. Vogt, C. von Essen, H. Voss, V. Votruba, S. Voutsinas, G. Walmsley, M. Weiler, O. Wertz, T. Wevers, Ł. Wyrzykowski, A. Yoldas, M. Žerjal, H. Ziaeepour, J. Zorec, S. Zschocke, S. Zucker, C. Zurbach, and T. Zwitter. Gaia Data Release 2. Summary of the

contents and survey properties. A&A, 616:A1, Aug. 2018.

[14] Gaia Collaboration, A. G. A. Brown, A. Vallenari, T. Prusti, J. H. J. de Bruijne, C. Babusiaux, M. Biermann, O. L. Creevey, D. W. Evans, L. Eyer, A. Hutton, F. Jansen, C. Jordi, S. A. Klioner, U. Lammers, L. Lindegren, X. Luri, F. Mignard, C. Panem, D. Pourbaix, S. Randich, P. Sartoretti, C. Soubiran, N. A. Walton, F. Arenou, C. A. L. Bailer-Jones, U. Bastian, M. Cropper, R. Drimmel, D. Katz, M. G. Lattanzi, F. van Leeuwen, J. Bakker, C. Cacciari, J. Castañeda, F. De Angeli, C. Ducourant, C. Fabricius, M. Fouesneau, Y. Frémat, R. Guerra, A. Guerrier, J. Guiraud, A. Jean-Antoine Piccolo, E. Masana, R. Messineo, N. Mowlavi, C. Nicolas, K. Nienartowicz, F. Pailler, P. Panuzzo, F. Riclet, W. Roux, G. M. Seabroke, R. Sordo, P. Tanga, F. Thévenin, G. Gracia-Abril, J. Portell, D. Teyssier, M. Altmann, R. Andrae, I. Bellas-Velidis, K. Benson, J. Berthier, R. Blomme, E. Brugaletta, P. W. Burgess, G. Busso, B. Carry, A. Cellino, N. Cheek, G. Clementini, Y. Damerdji, M. Davidson, L. Delchambre, A. Dell'Oro, J. Fernández-Hernández, L. Galluccio, P. García-Lario, M. Garcia-Reinaldos, J. González-Núñez, E. Gosset, R. Haigron, J. L. Halbwachs, N. C. Hambly, D. L. Harrison, D. Hatzidimitriou, U. Heiter, J. Hernández, D. Hestroffer, S. T. Hodgkin, B. Holl, K. Janßen, G. Jevardat de Fombelle, S. Jordan, A. Krone-Martins, A. C. Lanzafame, W. Löffler, A. Lorca, M. Manteiga, O. Marchal, P. M. Marrese, A. Moitinho, A. Mora, K. Muinonen, P. Osborne, E. Pancino, T. Pauwels, J. M. Petit, A. Recio-Blanco, P. J. Richards, M. Riello, L. Rimoldini, A. C. Robin, T. Roegiers, J. Rybizki, L. M. Sarro, C. Siopis, M. Smith, A. Sozzetti, A. Ulla, E. Utrilla, M. van Leeuwen, W. van Reeven, U. Abbas, A. Abreu Aramburu, S. Accart, C. Aerts, J. J. Aguado, M. Ajaj, G. Altavilla, M. A. Álvarez, J. Álvarez Cid-Fuentes, J. Alves, R. I. Anderson, E. Anglada Varela, T. Antoja, M. Audard, D. Baines, S. G. Baker, L. Balaguer-Núñez, E. Balbinot, Z. Balog, C. Barache, D. Barbato, M. Barros, M. A. Barstow, S. Bartolomé, J. L. Bassilana, N. Bauchet, A. Baudesson-Stella, U. Becciani, M. Bellazzini, M. Bernet, S. Bertone, L. Bianchi, S. Blanco-Cuaresma, T. Boch, A. Bombrun, D. Bossini, S. Bouquillon, A. Bragaglia, L. Bramante, E. Breedt, A. Bressan, N. Brouillet, B. Bucciarelli, A. Burlacu, D. Busonero, A. G. Butkevich, R. Buzzi, E. Caffau, R. Cancelliere, H. Cánovas, T. Cantat-Gaudin, R. Carballo, T. Carlucci, M. I. Carnerero, J. M. Carrasco, L. Casamiquela, M. Castellani, A. Castro-Ginard, P. Castro Sampol, L. Chaoul, P. Charlot, L. Chemin, A. Chiavassa, M. R. L.

Cioni, G. Comoretto, W. J. Cooper, T. Cornez, S. Cowell, F. Crifo, M. Crosta, C. Crowley, C. Dafonte, A. Dapergolas, M. David, P. David, P. de Laverny, F. De Luise, R. De March, J. De Ridder, R. de Souza, P. de Teodoro, A. de Torres, E. F. del Peloso, E. del Pozo, M. Delbo, A. Delgado, H. E. Delgado, J. B. Delisle, P. Di Matteo, S. Diakite, C. Diener, E. Distefano, C. Dolding, D. Eappachen, B. Edvardsson, H. Enke, P. Esquej, C. Fabre, M. Fabrizio, S. Faigler, G. Fedorets, P. Fernique, A. Fienga, F. Figueras, C. Fouron, F. Fragkoudi, E. Fraile, F. Franke, M. Gai, D. Garabato, A. Garcia-Gutierrez, M. García-Torres, A. Garofalo, P. Gavras, E. Gerlach, R. Geyer, P. Giacobbe, G. Gilmore, S. Girona, G. Giuffrida, R. Gomel, A. Gomez, I. Gonzalez-Santamaria, J. J. González-Vidal, M. Granvik, R. Gutiérrez-Sánchez, L. P. Guy, M. Hauser, M. Haywood, A. Helmi, S. L. Hidalgo, T. Hilger, N. Hładczuk, D. Hobbs, G. Holland, H. E. Huckle, G. Jasniewicz, P. G. Jonker, J. Juaristi Campillo, F. Julbe, L. Karbevska, P. Kervella, S. Khanna, A. Kochoska, M. Kontizas, G. Kordopatis, A. J. Korn, Z. Kostrzewa-Rutkowska, K. Kruszyńska, S. Lambert, A. F. Lanza, Y. Lasne, J. F. Le Campion, Y. Le Fustec, Y. Lebreton, T. Lebzelter, S. Leccia, N. Leclerc, I. Lecoeur-Taibi, S. Liao, E. Licata, H. E. P. Lindstrøm, T. A. Lister, E. Livanou, A. Lobel, P. Madrero Pardo, S. Managau, R. G. Mann, J. M. Marchant, M. Marconi, M. M. S. Marcos Santos, S. Marinoni, F. Marocco, D. J. Marshall, L. Martin Polo, J. M. Martín-Fleitas, A. Masip, D. Massari, A. Mastrobuono-Battisti, T. Mazeh, P. J. McMillan, S. Messina, D. Michalik, N. R. Millar, A. Mints, D. Molina, R. Molinaro, L. Molnár, P. Montegriffo, R. Mor, R. Morbidelli, T. Morel, D. Morris, A. F. Mulone, D. Munoz, T. Muraveva, C. P. Murphy, I. Musella, L. Noval, C. Ordénovic, G. Orrù, J. Osinde, C. Pagani, I. Pagano, L. Palaversa, P. A. Palicio, A. Panahi, M. Pawlak, X. Peñalosa Esteller, A. Penttilä, A. M. Piersimoni, F. X. Pineau, E. Plachy, G. Plum, E. Poggio, E. Poretti, E. Poujoulet, A. Prša, L. Pulone, E. Racero, S. Ragaini, M. Rainer, C. M. Raiteri, N. Rambaux, P. Ramos, M. Ramos-Lerate, P. Re Fiorentin, S. Regibo, C. Reylé, V. Ripepi, A. Riva, G. Rixon, N. Robichon, C. Robin, M. Roelens, L. Rohrbasser, M. Romero-Gómez, N. Rowell, F. Royer, K. A. Rybicki, G. Sadowski, A. Sagristà Sellés, J. Sahlmann, J. Salgado, E. Salguero, N. Samaras, V. Sanchez Gimenez, N. Sanna, R. Santoveña, M. Sarasso, M. Schultheis, E. Sciacca, M. Segol, J. C. Segovia, D. Ségransan, D. Semeux, S. Shahaf, H. I. Siddiqui, A. Siebert, L. Siltala, E. Slezak, R. L. Smart, E. Solano, F. Solitro, D. Souami, J. Souchay, A. Spagna, F. Spoto, I. A. Steele, H. Steidelmüller, C. A. Stephenson, M. Süveges,

L. Szabados, E. Szegedi-Elek, F. Taris, G. Tauran, M. B. Taylor, R. Teixeira, W. Thuillot, N. Tonello, F. Torra, J. Torra, C. Turon, N. Unger, M. Vaillant, E. van Dillen, O. Vanel, A. Vecchiato, Y. Viala, D. Vicente, S. Voutsinas, M. Weiler, T. Wevers, Ł. Wyrzykowski, A. Yoldas, P. Yvard, H. Zhao, J. Zorec, S. Zucker, C. Zurbach, and T. Zwitter. Gaia Early Data Release 3. Summary of the contents and survey properties (Corrigendum). A&A, 650:C3, June 2021.

[15] Gaia Collaboration, A. G. A. Brown, A. Vallenari, T. Prusti, J. H. J. de Bruijne, F. Mignard, R. Drimmel, C. Babusiaux, C. A. L. Bailer-Jones, U. Bastian, M. Biermann, D. W. Evans, L. Eyer, F. Jansen, C. Jordi, D. Katz, S. A. Klioner, U. Lammers, L. Lindegren, X. Luri, W. O'Mullane, C. Panem, D. Pourbaix, S. Randich, P. Sartoretti, H. I. Siddiqui, C. Soubiran, V. Valette, F. van Leeuwen, N. A. Walton, C. Aerts, F. Arenou, M. Cropper, E. Høg, M. G. Lattanzi, E. K. Grebel, A. D. Holland, C. Huc, X. Passot, M. Perryman, L. Bramante, C. Cacciari, J. Castañeda, L. Chaoul, N. Cheek, F. De Angeli, C. Fabricius, R. Guerra, J. Hernández, A. Jean-Antoine-Piccolo, E. Masana, R. Messineo, N. Mowlavi, K. Nienartowicz, D. Ordóñez-Blanco, P. Panuzzo, J. Portell, P. J. Richards, M. Riello, G. M. Seabroke, P. Tanga, F. Thévenin, J. Torra, S. G. Els, G. Gracia-Abril, G. Comoretto, M. Garcia-Reinaldos, T. Lock, E. Mercier, M. Altmann, R. Andrae, T. L. Astraatmadja, I. Bellas-Velidis, K. Benson, J. Berthier, R. Blomme, G. Busso, B. Carry, A. Cellino, G. Clementini, S. Cowell, O. Creevey, J. Cuypers, M. Davidson, J. De Ridder, A. de Torres, L. Delchambre, A. Dell'Oro, C. Ducourant, Y. Frémat, M. García-Torres, E. Gosset, J. L. Halbwachs, N. C. Hambly, D. L. Harrison, M. Hauser, D. Hestroffer, S. T. Hodgkin, H. E. Huckle, A. Hutton, G. Jasniewicz, S. Jordan, M. Kontizas, A. J. Korn, A. C. Lanzafame, M. Manteiga, A. Moitinho, K. Muinonen, J. Osinde, E. Pancino, T. Pauwels, J. M. Petit, A. Recio-Blanco, A. C. Robin, L. M. Sarro, C. Siopis, M. Smith, K. W. Smith, A. Sozzetti, W. Thuillot, W. van Reeven, Y. Viala, U. Abbas, A. Abreu Aramburu, S. Accart, J. J. Aguado, P. M. Allan, W. Allasia, G. Altavilla, M. A. Álvarez, J. Alves, R. I. Anderson, A. H. Andrei, E. Anglada Varela, E. Antiche, T. Antoja, S. Antón, B. Arcay, N. Bach, S. G. Baker, L. Balaguer-Núñez, C. Barache, C. Barata, A. Barbier, F. Barblan, D. Barrado y Navascués, M. Barros, M. A. Barstow, U. Becciani, M. Bellazzini, A. Bello García, V. Belokurov, P. Bendjoya, A. Berihuete, L. Bianchi, O. Bienaymé, F. Billebaud, N. Blagorodnova, S. Blanco-Cuaresma, T. Boch, A. Bom-

brun, R. Borrachero, S. Bouquillon, G. Bourda, H. Bouy, A. Bragaglia, M. A. Breddels, N. Brouillet, T. Brüsemeister, B. Bucciarelli, P. Burgess, R. Burgon, A. Burlacu, D. Busonero, R. Buzzi, E. Caffau, J. Cambras, H. Campbell, R. Cancelliere, T. Cantat-Gaudin, T. Carlucci, J. M. Carrasco, M. Castellani, P. Charlot, J. Charnas, A. Chiavassa, M. Clotet, G. Cocozza, R. S. Collins, G. Costigan, F. Crifo, N. J. G. Cross, M. Crosta, C. Crowley, C. Dafonte, Y. Damerdji, A. Dapergolas, P. David, M. David, P. De Cat, F. de Felice, P. de Laverny, F. De Luise, R. De March, D. de Martino, R. de Souza, J. Debosscher, E. del Pozo, M. Delbo, A. Delgado, H. E. Delgado, P. Di Matteo, S. Diakite, E. Distefano, C. Dolding, S. Dos Anjos, P. Drazinos, J. Duran, Y. Dzigan, B. Edvardsson, H. Enke, N. W. Evans, G. Eynard Bontemps, C. Fabre, M. Fabrizio, S. Faigler, A. J. Falcão, M. Farràs Casas, L. Federici, G. Fedorets, J. Fernández-Hernández, P. Fernique, A. Fienga, F. Figueras, F. Filippi, K. Findeisen, A. Fonti, M. Fouesneau, E. Fraile, M. Fraser, J. Fuchs, M. Gai, S. Galleti, L. Galluccio, D. Garabato, F. García-Sedano, A. Garofalo, N. Garralda, P. Gavras, J. Gerssen, R. Geyer, G. Gilmore, S. Girona, G. Giuffrida, M. Gomes, A. González-Marcos, J. González-Núñez, J. J. González-Vidal, M. Granvik, A. Guerrier, P. Guillout, J. Guiraud, A. Gúrpide, R. Gutiérrez-Sánchez, L. P. Guy, R. Haigron, D. Hatzidimitriou, M. Haywood, U. Heiter, A. Helmi, D. Hobbs, W. Hofmann, B. Holl, G. Holland, J. A. S. Hunt, A. Hypki, V. Icardi, M. Irwin, G. Jevardat de Fombelle, P. Jofré, P. G. Jonker, A. Jorissen, F. Julbe, A. Karampelas, A. Kochoska, R. Kohley, K. Kolenberg, E. Kontizas, S. E. Koposov, G. Kordopatis, P. Koubsky, A. Krone-Martins, M. Kudryashova, I. Kull, R. K. Bachchan, F. Lacoste-Seris, A. F. Lanza, J. B. Lavigne, C. Le Poncin-Lafitte, Y. Lebreton, T. Lebzelter, S. Leccia, N. Leclerc, I. Lecoeur-Taibi, V. Lemaitre, H. Lenhardt, F. Leroux, S. Liao, E. Licata, H. E. P. Lindstrøm, T. A. Lister, E. Livanou, A. Lobel, W. Löffler, M. López, D. Lorenz, I. MacDonald, T. Magalhães Fernandes, S. Managau, R. G. Mann, G. Mantelet, O. Marchal, J. M. Marchant, M. Marconi, S. Marinoni, P. M. Marrese, G. Marschalkó, D. J. Marshall, J. M. Martín-Fleitas, M. Martino, N. Mary, G. Matijevič, T. Mazeh, P. J. McMillan, S. Messina, D. Michalik, N. R. Millar, B. M. H. Miranda, D. Molina, R. Molinaro, M. Molinaro, L. Molnár, M. Moniez, P. Montegriffo, R. Mor, A. Mora, R. Morbidelli, T. Morel, S. Morgenthaler, D. Morris, A. F. Mulone, T. Muraveva, I. Musella, J. Narbonne, G. Nelemans, L. Nicastro, L. Noval, C. Ordénovic, J. Ordieres-Meré, P. Osborne, C. Pagani, I. Pagano, F. Pailler, H. Palacin, L. Palaversa,

P. Parsons, M. Pecoraro, R. Pedrosa, H. Pentikäinen, B. Pichon, A. M. Piersimoni, F. X. Pineau, E. Plachy, G. Plum, E. Poujoulet, A. Prša, L. Pulone, S. Ragaini, S. Rago, N. Rambaux, M. Ramos-Lerate, P. Ranalli, G. Rauw, A. Read, S. Regibo, C. Reylé, R. A. Ribeiro, L. Rimoldini, V. Ripepi, A. Riva, G. Rixon, M. Roelens, M. Romero-Gómez, N. Rowell, F. Royer, L. Ruiz-Dern, G. Sadowski, T. Sagristà Sellés, J. Sahlmann, J. Salgado, E. Salguero, M. Sarasso, H. Savietto, M. Schultheis, E. Sciacca, M. Segol, J. C. Segovia, D. Segransan, I. C. Shih, R. Smareglia, R. L. Smart, E. Solano, F. Solitro, R. Sordo, S. Soria Nieto, J. Souchay, A. Spagna, F. Spoto, U. Stampa, I. A. Steele, H. Steidelmüller, C. A. Stephenson, H. Stoev, F. F. Suess, M. Süveges, J. Surdej, L. Szabados, E. Szegedi-Elek, D. Tapiador, F. Taris, G. Tauran, M. B. Taylor, R. Teixeira, D. Terrett, B. Tingley, S. C. Trager, C. Turon, A. Ulla, E. Utrilla, G. Valentini, A. van Elteren, E. Van Hemelryck, M. van Leeuwen, M. Varadi, A. Vecchiato, J. Veljanoski, T. Via, D. Vicente, S. Vogt, H. Voss, V. Votruba, S. Voutsinas, G. Walmsley, M. Weiler, K. Weingrill, T. Wevers, Ł. Wyrzykowski, A. Yoldas, M. Žerjal, S. Zucker, C. Zurbach, T. Zwitter, A. Alecu, M. Allen, C. Allende Prieto, A. Amorim, G. Anglada-Escudé, V. Arsenijevic, S. Azaz, P. Balm, M. Beck, H. H. Bernstein, L. Bigot, A. Bijaoui, C. Blasco, M. Bonfigli, G. Bono, S. Boudreault, A. Bressan, S. Brown, P. M. Brunet, P. Bunclark, R. Buonanno, A. G. Butkevich, C. Carret, C. Carrion, L. Chemin, F. Chéreau, L. Corcione, E. Darmigny, K. S. de Boer, P. de Teodoro, P. T. de Zeeuw, C. Delle Luche, C. D. Domingues, P. Dubath, F. Fodor, B. Frézouls, A. Fries, D. Fustes, D. Fyfe, E. Gallardo, J. Gallegos, D. Gardiol, M. Gebran, A. Gomboc, A. Gómez, E. Grux, A. Gueguen, A. Heyrovsky, J. Hoar, G. Iannicola, Y. Isasi Parache, A. M. Janotto, E. Joliet, A. Jonckheere, R. Keil, D. W. Kim, P. Klagyivik, J. Klar, J. Knude, O. Kochukhov, I. Kolka, J. Kos, A. Kutka, V. Lainey, D. LeBouquin, C. Liu, D. Loreggia, V. V. Makarov, M. G. Marseille, C. Martayan, O. Martinez-Rubi, B. Massart, F. Meynadier, S. Mignot, U. Munari, A. T. Nguyen, T. Nordlander, P. Ocvirk, K. S. O'Flaherty, A. Olias Sanz, P. Ortiz, J. Osorio, D. Oszkiewicz, A. Ouzounis, M. Palmer, P. Park, E. Pasquato, C. Peltzer, J. Peralta, F. Péturaud, T. Pieniluoma, E. Pigozzi, J. Poels, G. Prat, T. Prod'homme, F. Raison, J. M. Rebordao, D. Risquez, B. Rocca-Volmerange, S. Rosen, M. I. Ruiz-Fuertes, F. Russo, S. Sembay, I. Serraller Vizcaino, A. Short, A. Siebert, H. Silva, D. Sinachopoulos, E. Slezak, M. Soffel, D. Sosnowska, V. Straižys, M. ter Linden, D. Terrell, S. Theil, C. Tiede, L. Troisi, P. Tsalmantza, D. Tur, M. Vac-

cari, F. Vachier, P. Valles, W. Van Hamme, L. Veltz, J. Virtanen, J. M. Wallut, R. Wichmann, M. I. Wilkinson, H. Ziaeepour, and S. Zschocke. Gaia Data Release 1. Summary of the astrometric, photometric, and survey properties. A&A, 595:A2, Nov. 2016.

[16] B. A. S. Gustafson. Geminid meteoroids traced to cometary activity on Phaethon. A&A, 225(2):533–540, Nov. 1989.

[17] Hanus, J., Durech, J., Oszkiewicz, D. A., Behrend, R., Carry, B., Delbo, M., Adam, O., Afonina, V., Anquetin, R., Antonini, P., Arnold, L., Audejean, M., Aurard, P., Bachschmidt, M., Baduel, B., Barbotin, E., Barroy, P., Baudouin, P., Berard, L., Berger, N., Bernasconi, L., Bosch, J-G., Bouley, S., Bozhinova, I., Brinsfield, J., Brunetto, L., Canaud, G., Caron, J., Carrier, F., Casalnuovo, G., Casulli, S., Cerda, M., Chalamet, L., Charbonnel, S., Chinaglia, B., Cikota, A., Colas, F., Coliac, J.-F., Collet, A., Coloma, J., Conjat, M., Conseil, E., Costa, R., Crippa, R., Cristofanelli, M., Damerdji, Y., Debackère, A., Decock, A., Déhais, Q., Déléage, T., Delmelle, S., Demeautis, C., Drózdz, M., Dubos, G., Dulcamara, T., Dumont, M., Durkee, R., Dymock, R., Escalante del Valle, A., Esseiva, N., Esseiva, R., Esteban, M., Fauchez, T., Fauerbach, M., Fauvaud, M., Fauvaud, S., Forné, E., Fournel, C., Fradet, D., Garlitz, J., Gerteis, O., Gillier, C., Gillon, M., Giraud, R., Godard, J.-P., Goncalves, R., Hamanowa, Hiroko, Hamanowa, Hiromi, Hay, K., Hellmich, S., Heterier, S., Higgins, D., Hirsch, R., Hodosan, G., Hren, M., Hygate, A., Innocent, N., Jacquinot, H., Jawahar, S., Jehin, E., Jerosimic, L., Klotz, A., Koff, W., Korlevic, P., Kosturkiewicz, E., Krafft, P., Krugly, Y., Kugel, F., Labrevoir, O., Lecacheux, J., Lehký, M., Leroy, A., Lesquerbault, B., Lopez-Gonzales, M. J., Lutz, M., Mallecot, B., Manfroid, J., Manzini, F., Marciniak, A., Martin, A., Modave, B., Montaigut, R., Montier, J., Morelle, E., Morton, B., Mottola, S., Naves, R., Nomen, J., Oey, J., Ogloza, W., Paiella, M., Pallares, H., Peyrot, A., Pilcher, F., Pirenne, J.-F., Piron, P., Poli´nska, M., Polotto, M., Poncy, R., Previt, J. P., Reignier, F., Renauld, D., Ricci, D., Richard, F., Rinner, C., Risoldi, V., Robilliard, D., Romeuf, D., Rousseau, G., Roy, R., Ruthroff, J., Salom, P. A., Salvador, L., Sanchez, S., Santana-Ros, T., Scholz, A., Séné, G., Skiff, B., Sobkowiak, K., Sogorb, P., Soldán, F., Spiridakis, A., Splanska, E., Sposetti, S., Starkey, D., Stephens, R., Stiepen, A., Stoss, R., Strajnic, J., Teng, J.-P., Tumolo, G., Vagnozzi, A., Vanoutryve, B., Vugnon, J. M., Warner, B. D., Waucomont, M., Wertz, O., Winiarski, M., and Wolf, M. New and

updated convex shape models of asteroids based on optical data from a large collaboration network. A&A, 586:A108, 2016.

[18] J. Hanuš, D. Vokrouhlický, M. Delbo', D. Farnocchia, D. Polishook, P. Pravec, K. Hornoch, H. Kučáková, P. Kušnirák, R. Stephens, and B. Warner. (3200) Phaethon: Bulk density from Yarkovsky drift detection. A&A, 620:L8, Dec. 2018.

[19] P. Hong, K. Ishibashi, S. Sato, O. Okudaira, M. Otsuki, T. Hosonuma, H. Toyota, K. Nishiyama, and T. Takashima. Initial Test for the Breadboard Model of TCAP Tracking Mirror of DESTINY+ Mission. In 52nd Lunar and Planetary Science Conference, Lunar and Planetary Science Conference, page 1741, Mar. 2021.

[20] K. Ishibashi, P. Hong, T. Okamoto, T. Ishimaru, N. Okazaki, T. Hosonuma, S. Sato, T. Arai, F. Yoshida, O. Okudaira, M. Kagitani, T. Miyabara, M. Ohta, and T. Takashima. Development of Cameras Onboard DESTINY+ Spacecraft for Flyby Observation of (3200) Phaethon. In 52nd Lunar and Planetary Science Conference, Lunar and Planetary Science Conference, page 1405, Mar. 2021.

[21] P. Jenniskens. Meteor Showers and their Parent Comets. Cambridge University Press, 2006.

[22] D. Jewitt, D. Asmus, B. Yang, and J. Li. High-resolution thermal infrared imaging of 3200 phaethon. The Astronomical Journal, 157(5):193, apr 2019.

[23] D. Jewitt and J. Li. ACTIVITY IN GEMINID PARENT (3200) PHAETHON. The Astronomical Journal, 140(5):1519–1527, oct 2010.

[24] T. Kareta, V. Reddy, C. Hergenrother, D. S. Lauretta, T. Arai, D. Takir, J. Sanchez, and J. Hanuš. Rotationally resolved spectroscopic characterization of near-earth object (3200) phaethon. The Astronomical Journal, 156(6):287, nov 2018.

[25] Kim, M.-J., Lee, H.-J., Lee, S.-M., Kim, D.-H., Yoshida, F., Bartczak, P., Dudzi´nski, G., Park, J., Choi, Y.-J., Moon, H.-K., Yim, H.-S., Choi, J., Choi, E.-J., Yoon, J.-N., Serebryanskiy, A., Krugov, M., Reva, I., Ergashev, K. E., Burkhonov, O., Ehgamberdiev, S. A., Turayev, Y., Lin, Z.-Y., Arai, T., Ohtsuka, K., Ito, T., Urakawa, S., and Ishiguro, M. Optical observations of nea 3200 phaethon (1983 tb) during the 2017 apparition. A&A, 619:A123, 2018.

[26] H. Krüger. Dust Science with the DESTINY+ Dust Analyzer. In European Planetary Science Congress, pages EPSC2021–871, Sept. 2021.

[27] Y. Krugly, I. Belskaya, V. Shevchenko, V. Chiorny, F. Velichko, S. Mottola, A. Erikson, G. Hahn, A. Nathues, G. Neukum, N. Gaftonyuk, and E. Dotto. The near-earth objects follow-up program: Iv. ccd photometry in 1996–1999. Icarus, 158(2):294–304, 2002.

[28] D. S. Lauretta, D. N. Dellagiustina, C. A. Bennett, D. R. Golish, K. J. Becker, S. S. Balram-Knutson, O. S. Barnouin, T. L. Becker, W. F. Bottke, W. V. Boynton, H. Campins, B. E. Clark, H. C. Connolly, C. Y. Drouet D'Aubigny, J. P. Dworkin, J. P. Emery, H. L. Enos, V. E. Hamilton, C. W. Hergenrother, E. S. Howell, M. R. M. Izawa, H. H. Kaplan, M. C. Nolan, B. Rizk, H. L. Roper, D. J. Scheeres, P. H. Smith, K. J. Walsh, C. W. V. Wolner, and Osiris-Rex Team. The unexpected surface of asteroid (101955) Bennu. Nature, 568(7750):55–60, Mar. 2019.

[29] M. Lazzarin, V. Petropoulou, I. Bertini, F. La Forgia, P. Ochner, A. Migliorini, and A. Siviero. Phaethon variability during december 2017 closest approach to earth. Planetary and Space Science, 165:115–123, 2019.

[30] H.-J. Lee, M.-J. Kim, D.-H. Kim, H.-K. Moon, Y.-J. Choi, C.-H. Kim, B.-C. Lee, F. Yoshida, D.-G. Roh, and H. Seo. Investigation of surface homogeneity of (3200) phaethon. Planetary and Space Science, 165:296–302, 2019.

[31] Y. Li, Z. Sternovsky, H. Krueger, R. Srama, M. Kobayashi, N. Altobelli, T. Arai, A. Mocker, H. Kimura, J. Simolka, M. Trieloff, F. Posterberg, N. Khawaja, J. Hillier, M. Sommer, H. Strack, and S. Kempf. Interplanetary and interstellar dust measurement with DESTINY+. In 43rd COSPAR Scientific Assembly. Held 28 January - 4 February, volume 43, page 307, Jan. 2021.

[32] Z.-Y. Lin, F. Yoshida, Y.-C. Lin, C.-C. Cheng, W.-H. Ip, Y.-C. Cheng, K.-S. Pan, K. Daisuke, and H.-C. Chi. A study of photometric observations of (3200) phaethon from lulin observatory. Planetary and Space Science, 194:105114, 2020.

[33] E. MacLennan, A. Toliou, and M. Granvik. Dynamical evolution and thermal history of asteroids (3200) phaethon and (155140) 2005 ud. Icarus, 366:114535, 2021.

[34] E. A. Magnier, K. C. Chambers, H. A. Flewelling, J. C. Hoblitt, M. E. Huber, P. A. Price, W. E. Sweeney, C. Z. Waters, L. Denneau, P. W. Draper, K. W. Hodapp, R. Jedicke, N. Kaiser, R. P. Kudritzki, N. Metcalfe, C. W. Stubbs, and R. J. Wainscoat. The Pan-STARRS Data-processing System. ApJS, 251(1):3, Nov. 2020.

[35] K. Ohtsuka, T. Ito, D. Kinoshita, S. Abe, K. Sawai, K. Funabashi, R. Kato, S. Miyasaka, S. Hasegawa, T. Nakamura, and W.-P. Chen. Full rotationally phase-resolved visible reflectance spectroscopy of 3200 phaethon. Planetary and Space Science, 191:104940, 2020.

[36] K. Ohtsuka, A. Nakato, T. Nakamura, D. Kinoshita, T. Ito, M. Yoshikawa, and S. Hasegawa. Solar-Radiation Heating Effects on 3200 Phaethon. Publications of the Astronomical Society of Japan, 61(6):1375–1387, 12 2009.

[37] P. Pravec, M. Wolf, and L. Šarounová. Lightcurves of 26 near-earth asteroids. Icarus, 136(1):124–153, 1998.

[38] M. Tabeshian, P. Wiegert, Q. Ye, M.-T. Hui, X. Gao, and H. Tan. Asteroid (3200) phaethon: Colors, phase curve, limits on cometary activity, and fragmentation. The Astronomical Journal, 158(1):30, jun 2019.

[39] S. Watanabe, M. Hirabayashi, N. Hirata, N. Hirata, R. Noguchi, Y. Shimaki, H. Ikeda, E. Tatsumi, M. Yoshikawa, S. Kikuchi, H. Yabuta, T. Nakamura, S. Tachibana, Y. Ishihara, T. Morota, K. Kitazato, N. Sakatani, K. Matsumoto, K. Wada, H. Senshu, C. Honda, T. Michikami, H. Takeuchi, T. Kouyama, R. Honda, S. Kameda, T. Fuse, H. Miyamoto, G. Komatsu, S. Sugita, T. Okada, N. Namiki, M. Arakawa, M. Ishiguro, M. Abe, R. Gaskell, E. Palmer, O. S. Barnouin, P. Michel, A. S. French, J. W. McMahon, D. J. Scheeres, P. A. Abell, Y. Yamamoto, S. Tanaka, K. Shirai, M. Matsuoka, M. Yamada, Y. Yokota, H. Suzuki, K. Yoshioka, Y. Cho, S. Tanaka, N. Nishikawa, T. Sugiyama, H. Kikuchi, R. Hemmi, T. Yamaguchi, N. Ogawa, G. Ono, Y. Mimasu, K. Yoshikawa, T. Takahashi, Y. Takei, A. Fujii, C. Hirose, T. Iwata, M. Hayakawa, S. Hosoda, O. Mori, H. Sawada, T. Shimada, S. Soldini, H. Yano, R. Tsukizaki, M. Ozaki,

Y. Iijima, K. Ogawa, M. Fujimoto, T. M. Ho, A. Moussi, R. Jaumann, J. P. Bibring, C. Krause, F. Terui, T. Saiki, S. Nakazawa, and Y. Tsuda. Hayabusa2 arrives at the carbonaceous asteroid 162173 Ryugu—A spinning top-shaped rubble pile. Science, 364(6437):268–272, Apr. 2019.

[40] S.-i. Watanabe, Y. Tsuda, M. Yoshikawa, S. Tanaka, T. Saiki, and S. Nakazawa. Hayabusa2 Mission Overview. SSRv, 208(1-4):3–16, July 2017.

[41] I. P. Williams and Z. Wu. The Geminid meteor stream and asteroid 3200 Phaethon. MNRAS, 262(1):231–248, May 1993.

[42] F. Yoshida, T. Hayamizu, K. Miyashita, H. Watanabe, H. Yamamura, H. Akitaya, A. Asai, Y. Fujiwara, T. Goto, G. L. Hashimoto, A. Hatanaka, T. Horaguchi, M. Ida, K. Imamura, K. Isobe, M. Ishiguro, N. Kaizuka, H. Kasebe, Y. Kawasaki, T. Kim, K. Kitazaki, N. Manago, M. Matsumura, H. Matsushita, S. Matsuura, T. Nakamura, T. Nagata, H. Noda, M. Ogawa, O. Ohshima, M. Owada, K. Saitou, M. Tsumura, Y. Ueyama, H. Watanabe, M.-y. Yamamoto, H. Yoshihara, T. Fujiwara, M. Haraguchi, H. Hayashi, T. Hitotsuda, T. Horikawa, K. Ishida, T. Ito, S. Jin, W. Kang, T. Katayama, K. S. Kawabata, R. Kawasaki, K. Kim, M. Kita, N. Kitazaki, H. Kurisu, M. Matsushima, C. Matsumi, A. Mihari, M. Naka, T. Nakaoka, R. Nishihama, Y. Nishiyama, S. Nukui, M. Oba, T. Okamoto, Y. Omori, J. Seo, H. Shirakawa, T. Sugino, Y. Tani, K. Takagaki, Y. Ueda, S. Urakawa, M. Watanabe, K. Yamashita, M. Yamashita, I. Sato, S. Murayama, T. Arai, D. Herald, and A. Higuchi. Multi-chord observation of stellar occultation by the near-Earth asteroid (3200) Phaethon on 2021 October 3 (UTC) with very high accuracy. Publications of the Astronomical Society of Japan, 12 2022. psac096.